University of Massachusetts Amherst

ScholarWorks@UMass Amherst

October 2019

Providing Molecular Insight for Understanding Anion Exchange Membrane Conductivity

Michael Kwasny

Follow this and additional works at: https://scholarworks.umass.edu/dissertations_2

Part of the Inorganic Chemistry Commons, Organic Chemistry Commons, Physical Chemistry Commons, and the Polymer Chemistry Commons

Recommended Citation

Kwasny, Michael, "Providing Molecular Insight for Understanding Anion Exchange Membrane Conductivity" (2019). *Doctoral Dissertations*. 1743.
https://scholarworks.umass.edu/dissertations_2/1743

PROVIDING MOLECULAR INSIGHT FOR UNDERSTANDING ANION EXCHANGE MEMBRANE CONDUCTIVITY

A Dissertation Presented

By

MICHAEL THOMAS KWASNY

Submitted to the Graduate School of the
University of Massachusetts Amherst in partial fulfillment
of the requirements for the degree of

DOCTOR OF PHILOSOPHY

September 2019

Polymer Science and Engineering

PROVIDING MOLECULAR INSIGHT FOR UNDERSTANDING ANION EXCHANGE MEMBRANE CONDUCTIVITY

A Dissertation Presented

By

MICHAEL THOMAS KWASNY

Approved as to Style and Content By:

_____

Gregory N. Tew, Chair

_____

Bryan Coughlin, Member

_____

Sarah Perry, Member

_____

Bryan Coughlin, Department Head
Polymer Science and Engineering

DEDICATION

To my wife, Diya Kwasny

ACKNOWLEDGEMENTS

I need to first and foremost acknowledge Jesus, my Lord and Savior for everything I have accomplished throughout my Ph.D. Everything I have achieved has come from Him and has been accomplished for Him. My gratitude for how He has blessed me cannot be fully expressed with words, I just tried to bring Him glory every moment of every day. Thank You for everything.

A majority of the text and figures in the following dissertation come directly from previously published work or articles that are currently in press or in review. The source of the text and figures is identified and credited before it is used immediately preceding the chapter in which it was used. Full copyright credit to respective parties has been given to best of my ability when and where possible.

I need to sincerely thank my advisor throughout my Ph.D. experience, Professor Greg Tew. Once joining PSE, it was obvious that Greg was my top choice for an advisor as it was clear to me from our first meeting that this was someone I could thoroughly enjoy working for and could be successful under. I truly appreciate his straightforward and honest approach as well as his willingness to challenge each of his students to be better, in the

specific and unique ways each student needed to be challenged. He provided me the freedom to work independently and explore science without micromanagement, but also questioned everything I did and guided me when I needed it, even when I didn't realize I needed guidance. His attention to detail and ability to understand his students is something I truly respect and hope I can learn to do when I begin to manage other people. He not only notices the areas of growth, but he also is great at acknowledging the areas of excellence for his students. Throughout the years working with Greg, he has made me a better scientist, teaching me how to fully examine a problem before moving on as opposed to dropping the project when it doesn't work instantly. Thank you Greg, for all of your help getting me through my Ph.D, I have thoroughly enjoyed the time I was able to work for you.

I also need to thank my committee members: Professor Bryan Coughlin and Professor Sarah Perry. I thank both of you for their willingness to meet and have conversations at any point. I appreciate the numerous conversations I had with Bryan about my career and next steps. His wisdom and challenges about what I wanted from a career helped shape the direction I took in my life and helped me to better understand why I am pursuing the path I chose. They may have seemed like simple conversations walking into Conte or standing in the halls, but I always took something important from them and I am thankful for that. I also enjoyed the opportunity to talk about baseball with Bryan on many occasions. Not only do I is it one of my favorite sports, but it also helped me to remember that there is more to life than science, and that it is important to enjoy those things. Plus, I relish the opportunity to talk baseball with anyone who is willing. Beyond that, I appreciate how Bryan and Sarah constantly challenged me scientifically, and caught all of my mistakes, no matter how small, helping me to notice the small details better while still seeing the big

picture of the research. I also need to thank Sarah for all of her help in my research. I had the opportunity to meet with her on a few different occasions, and every time I left with a wealth of knowledge I did not have when I entered her office and an entirely different perspective on my research. She helped me to see different angles for my scientific problems that I could never have seen on my own. I wish now that I had taken the opportunity to meet with her more often, however I appreciate the times I did. Those experiences have helped me to better see different aspects of research to be a more complete and flexible scientist. Thank you, Bryan and Sarah.

I also want to acknowledge our collaborator Professor Mike Hickner at the Pennsylvania State University. His expertise and capabilities to run ion impedance spectroscopy where instrumental to my research. He taught me how to analyze impedance data and what we can all learn from it, and his students (Dr. Liang Zhu, Dr. Jing Pan, and Mr. Nayan Saikia) performed the experiments and provided the data for me. I am grateful for the hours and phone calls they spent working with me, despite the fact that my work was not their primary focus.

I could not have accomplished my Ph.D. without the help of countless members of the PSE and larger UMass community. I would like to thank Dr. Weiguo Hu for maintaining our various top-notch NMR instrumentations and for the numerous hours he spent teaching me different NMR spectroscopy techniques and analyses. I would like to thank Dr. Lizz Bartlett for her maintenance and assistance with the ITC experiments that made this Ph.D. so successful. Her teachings on how to run and analyze ITC data were instrumental for my research. The PSE administrative staff has gone above and beyond to welcome me into the department and guide and assist me throughout my Ph.D. experience. I need to sincerely

friend from the beginning. Thank you to Matt and Cara, Nick and Briana, Josh, Vijesh, Ryan and Cristiam for making living in Amherst and going to PSE so much fun. It has been such a blessing knowing everyone here at PSE. Special thanks to Hazel, Huyen, David, Liz, James, and Minjung for agreeing to join a Bible study this last semester in PSE. It has been amazing seeing God work in and through each of you and you have helped keep me focused on the most important things as I wrap up my Ph.D.

I also need to thank everyone at New Day Church that has supported me during my time here. Thanks to the Pastors Mike, Andrew, Peter and Tracey for all of their guidance and wise teachings. Thank you to all of the young adults who have helped take my walk with Jesus to new and deeper levels, making me a changed man for life. Special thanks to Holden, Caleb, Katie, and Anna. God has used you in such special and amazing ways, words cannot express my gratitude.

Finally, I have to thank my amazing family. First, thank you to my Dad, Mom, Katie and my extended family. You have been there supporting my interests in chemistry since I was a little kid. You allowed me to pursue my passions and follow my own path, despite how far from home it took me at times. Thank you. Your understanding and willingness to travel to visit me when I could not come home means more to me than you could ever know. I appreciate the interest you have shown in my research, despite barely understanding the any of it, has kept me excited by the work I have done here and motivated to do the best I can, to make each of you proud. During my Ph.D. I also had the privilege to add to my family Sanjay, Rae, Nisha, and Anjali Kapur. The way each and every one of you has welcomed me into the family has been so special to me. Your endless support and belief in me as I pursued my Ph.D. has inspired me. Watching how God has move in each

of you and how you have responded over the past 5 years is something that continuously renews my spirit and provides me hope in all situation.

Finally, and most importantly on Earth, I need to thank my wife Diya. How can I ever possibly thank you for everything you have done for me? You stayed at a job you hated to support me as I pursue my dreams and passions in life. You traveled almost every week, were exhausted, had to deal with terrible work-life balance, and the list just goes on, all so I could get my Ph.D. Essentially, you put your life on hold for me. Thank you is not enough. I am so excited that it is now your turn to pursue your path in life and to move on from Deloitte in Columbus. You challenge me to be a better person every day, and always remind me that my Ph.D. is important, but there are so many other things that are more important. You never let me get away with anything, always making me a better person and follower of Christ. I honestly could never have done this without you. I am so thankful to God for bringing us together and that you agreed to marry me.

ABSTRACT

**PROVIDING MOLECULAR INSIGHT FOR UNDERSTANDING ANION
EXCHNAGE MEMBRANE CONDUCTIVITY**

SEPTEMBER 2019

MICHAEL THOMAS KWASNY, B.S. CASE WESTERN RESERVE UNIVERSITY
(OH)

M.S. UNIVERSITY OF MASSACHUSETTS AMHERST

Ph.D., UNIVERSITY OF MASSACHUSETTS AMHERST

Directed by: Professor Gregory N. Tew

Anion exchange membranes (AEMs) are notorious for having both low alkaline
stability and poor ion conductivity in fuel cell operation conditions, with solutions to these
two challenges often being developed independent of each other. The chemical instability
of an AEM is viewed through degradation of the polymer backbone and the cationic species
and improving a material's stability is approached by altering the polymer backbone, the
cation, or both. On the other hand, poor ion conductivity is typically addressed by
modifying bulk membrane properties such as increasing the ion exchange capacity (IEC),
changing the morphology, or increasing the water uptake. These modifications are most
often accomplished by altering the polymers incorporated, the architecture of the polymers,
and increasing the number of cations in the network. However, as a deeper understanding
of these challenges is gained, the connection between the solutions to alkaline stability and
ion conductivity has become clearer. Both the cation's identity and the polymer backbone
incorporated into the membrane influence properties of the AEM, such as chemical
stability, morphology, and water uptake, which results in differences in ion conduction.
Therefore, developing parameters that can decouple the cation's and polymer's impact on

AEM properties from their impact on AEM ion conduction is critical to understanding and developing highly conductive AEMs.

Here, the impact of cation identity on AEM conductivity was explored using metal cation-based AEMs. Ring-opening metathesis polymerization (ROMP) was performed on di-norbornene functionalized, bis(terpyridine) metal complexes in the presence of norbornene, dicyclopentadiene (DCPD) and a di-norbornene functionalized poly(ethylene oxide) (PEO) crosslinker to control the crosslink density and IEC of these materials. Six different metal cations were studied (ruthenium, nickel, cobalt, iron, manganese, and zinc) along with four different counterions (chloride, bicarbonate, hydroxide, and acetate). Bicarbonate and hydroxide counterions were only utilized to explore the impact of the counterion on the water uptake of these metal cation-based AEMs, while chloride and acetate ions were used to explore the impact of counterion identity on ion conduction.

Interestingly, changing the identity of the metal center resulted in minimal changes to AEM properties such as mechanical stability and water uptake, while significant differences in chemical stability and ion conduction were observed. Commonly used bulk-level parameters, such as the hydration number, ion concentration, activation energy, and ion diffusion, offered important insights into AEM ion conduction, but they ultimately failed to fully capture the ion conduction phenomenon. Therefore, isothermal titration calorimetry (ITC) was used to quantify the dissociation thermodynamics for analogous small molecule metal cations through a counterion exchange reaction from either chloride or acetate to bicarbonate ions. This characterization technique showed that the enthalpic response to counterion exchange (ΔH_{tot}) corresponded to a molecular-level parameter termed the cation-counterion association strength (CCAS), where a smaller endothermic

ΔH_{tot} corresponds to a weaker CCAS. That ΔH_{tot} value can then be used to understand and predict AEM ion conduction since a weaker CCAS results in better ion conduction through a larger dissociation of counterions. The CCAS for different cation-counterion pairs is controlled by the degree of ion hydration, where the electrostatic interaction between the cation and water molecule stabilizes the charge, allowing for more facile dissociation of the counterion as the ion hydration increases.

This ITC approach was then expanded to characterize organic, nitrogen-based cations. A series of quaternary ammonium-based cations demonstrated that having a long alkyl chain spacer (10 atoms or more) between an aromatic group and the cation can weaken the CCAS. These parameters shed light on the importance of understanding the various facets of ion conduction and represent a significant step towards elucidating ion conduction trends for different cations through molecular-level interactions.

LIST OF TABLES

LIST OF FIGURES

CHAPTER 1

INTRODUCTION

1.1 Background

Ion exchange membranes (IEMs) are an important class of materials that utilize ionic moieties attached to polymer matrices to perform a variety of functions.[14] Typically, IEMs are classified into two types of membranes: 1) cation exchange membranes (CEMs) and 2) anion exchange membranes (AEMs).[1,14] CEMs utilize anionic head groups attached to the polymer matrix allowing for the transport of cationic species through the membrane and the exclusion of anionic species. Conversely, AEMs utilize cationic species attached to the polymer matrix allowing for the transport of anionic species and the exclusion of cations. Due to the selectivity imparted from the ionic groups, IEMs are a highly selective class of materials and are used in a variety of applications including water treatment, pharmaceutical, semiconductor, power generation, and energy conversion devices.[14–16]

Fuel cells are one class of energy conversion devices that have received growing interest over the past few decades due to their potential as an energy source that utilizes non-fossil fuels.[1,17,18] While there are multiple types of fuel cells, two have received the most attention: proton exchange membrane fuel cells (PEMFCs) and anion exchange membrane fuel cells (AEMFCs) (Figure 1). PEMFCs have garnered the most commercial success due to the development of the CEM Nafion, which has excellent chemical, mechanical, and conductive properties.[19–21] However, the high cost associated with PEMFCs has resulted in the need to develop lower cost devices, such as the AEMFC.[4,22–24] The alkaline conditions in AEMFCs allow for increased oxygen reduction kinetics.

These increased kinetics allows for more efficient energy conversion, the use of more cost-effective catalysts by utilizing non-platinum and non-precious metals, and a wider range of fuels that can be oxidized in AEMFCs over PEMFCs.[24,25] These realizations make AEMFCs an exciting opportunity for developing the next generation of energy conversion devices, with most research focusing on the ion conducting AEM.[18]
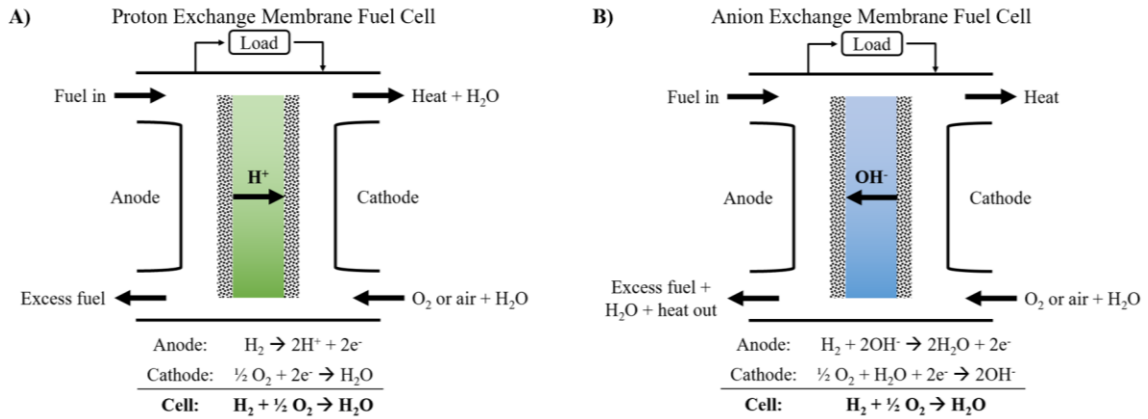
Figure 1. Schematic of A) proton exchange membrane fuel cell and B) anion exchange membrane fuel cell. Schematics adapted from literature. [1]

Despite this potential, advancements in AEM development are hampered by both low ion conduction and poor chemical stability as compared to their PEM counterparts.[1,5,17,26–30] The low ion conduction is due in large part to the intrinsically slower mobility of OH^- ions in AEMFCs as compared to H^+ ions in PEMFCs.[25] This hindered ion conductivity required the development of materials with specific design features, such as increasing the charge density in the material, or the ion exchange capacity (IEC), and introducing microphase separation to yield hydrophilic ion-conducting channels.[31–35] While these approaches have successfully improved the ion conduction in AEMs, they neither provide a better understanding of the ion transport mechanism nor correlate the impact of the polymer backbone and cation structure to the ion transport. Understanding

these two aspects of ion conduction is still needed before ion conduction can be fully optimized in AEMs.[1,25,27,36–38]

In addition to gaining a better understanding of ion conduction in AEMs, improving the poor alkaline chemical stability of the materials used in AEMs must also be accomplished. Improving the chemical stability has garnered more interest as membranes demonstrating high ion conduction have been reported, but the materials have been shown to degrade rapidly in high pH conditions. Materials have demonstrated up to 60% degradation within 30 days as measured by ion conduction and their IEC values.[39] This degradation is observed for the polymer backbones currently utilized, the cationic head groups attached to the polymer matrix, and a combination of the two (Figure 2).[2,3,14,17,40,41] Since the degradation pathways for polymer backbones and cation functional groups are two separate entities, they provide two separate and unique challenges towards improving AEM chemical stability. Here, recent advancements in cation development for use in AEMs are summarized and their impact on AEM conductivity is shown. This impact on ion conduction is used to demonstrate the need for identifying parameters that lead to a better understanding and prediction of ion conduction in AEMs.
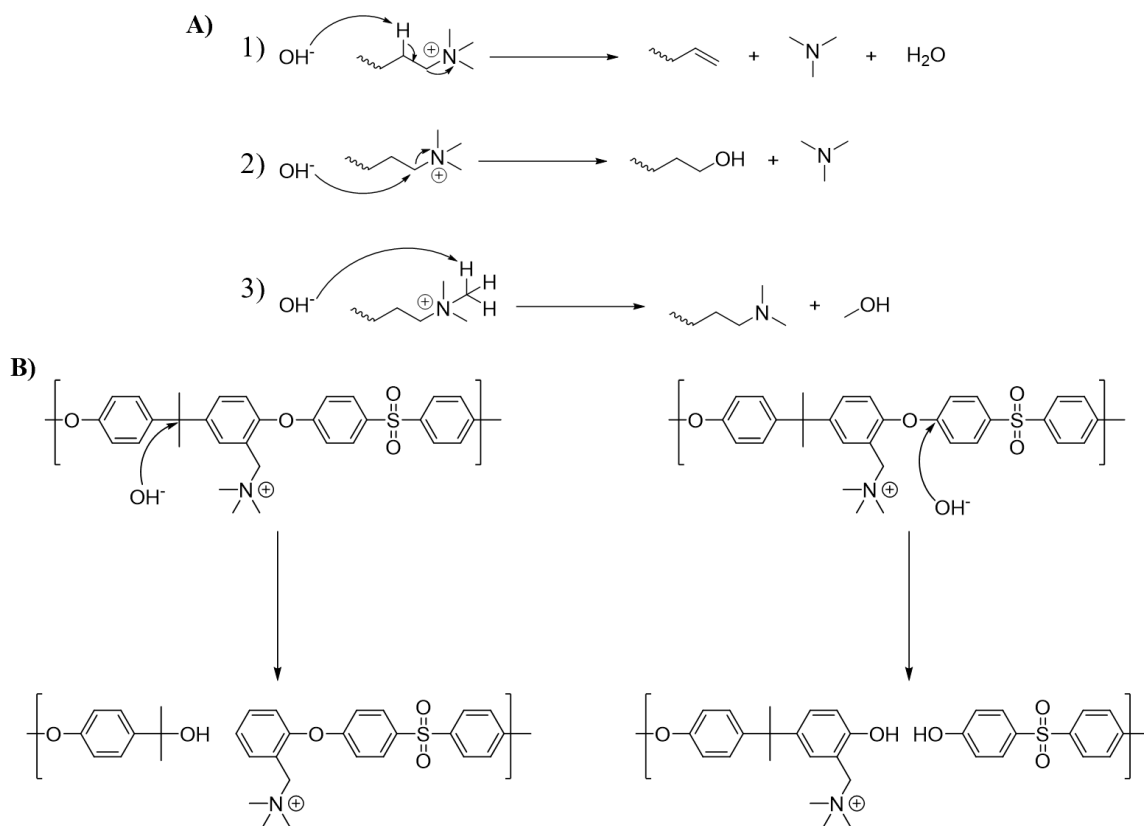
Figure 2. Common AEM degradation pathways for A) cationic species: 1) Hoffmann elimination, 2) nucleophilic substitution, 3) ylide formation, and B) polymer backbone from hydrolysis of: quaternary carbon (left) and ether bonds (right).[2,3]

1.2 Importance of the Membrane Chemistry on AEM Performance

1.2.1 Polymer Backbone Chemistry

Only recently has the impact of the polymer backbone on AEM chemical stability been proposed, although its impact on AEM degradation has quickly become apparent.[2] Aryl ether-based polymer backbones are most often designed due to their facile synthesis. However, it has become evident that the aryl ether functional group is susceptible to nucleophilic attack by the hydroxide ions present in fuel cell systems.[2,42–44] This realization has led to the evolution of AEM polymer chemistries well beyond the traditionally utilized poly(aryl ether) based materials (Figure 3).[4–8,45–50] Furthermore, it has been shown that

polymer backbone chemistry also influences cation chemical stability as well as AEM ion conduction.[28,40,42,51] Therefore, the polymer backbone must be considered as an important design feature to understand AEM ion conduction.
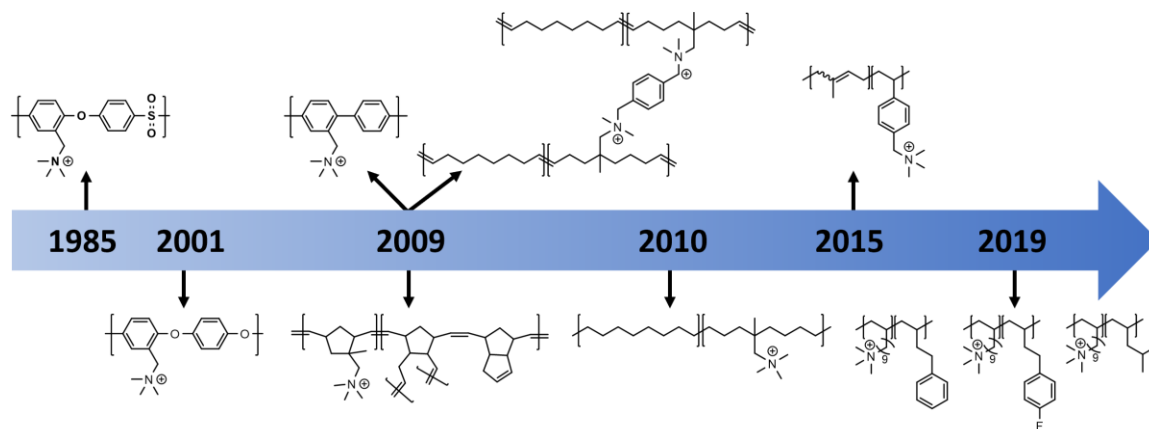
Figure 3. Evolution of polymer backbone chemistries throughout the history of AEM development starting from poly(aryl ether sulfone)s, transitioning to the removal of aryl ether moieties and most recently to olefin- and norbornene-based polymers.[4–8,45,49,50]

1.2.2 Cation Head Group Chemistry

While the impact of polymer backbone chemistry has only recently been considered, the impact of cation chemistry on AEM chemical stability is both well-known and extensively studied. Researchers have employed a variety of approaches to improve cation chemical stability ranging from adding steric hindrance around the cation to increasing the hydrophobicity of the cation, and ultimately to incorporating various types of cations (Figure 4).[11,37,47,52–69]
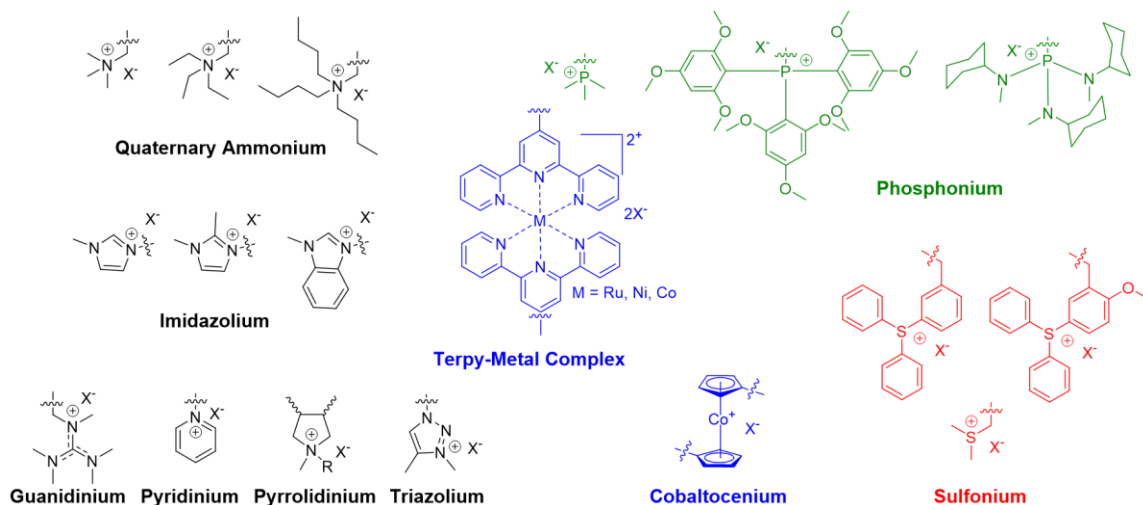
Figure 4. Chemical structures of various cations studied for use in AEM applications, where structures in black are amine-based cations, red are sulfur-based cations, green are phosphorus-based cations, and blue are metal-complex cations.

The most commonly used cation in AEMs is the quaternary ammonium (QA), due in large part to its synthetic ease as well as the potential for high ion conductivity.[3,70] However, QAs quickly degrade in alkaline conditions at high temperatures through one of three processes: 1) Hoffman elimination, 2) nucleophilic substitution, and 3) ylide formation.[3,28] While all three processes must be considered, Hoffman elimination through hydroxide reaction with β-hydrogens represents the most prevalent pathway through which QA groups degrade. Therefore, a popular early approach towards improving QA chemical stability was to design polymer architectures specifically without hydrogens in the β position.[4,7,8] While initial reports using this approach demonstrated improved alkaline stability, more recent reports have indicated this may not be the case due to the presence of the other two degradation pathways.[3]

Therefore, the impact of the alkyl chain length attached to the QA as well as the distance between the QA and the polymer backbone have also been explored.[71–73] Functionalizing the QA with longer alkyl chains, such as ethyl, butyl and hexyl, yielded an

improved chemical stability due to the increased hydrophobicity and steric hinderance around the cation, making it more difficult for the hydroxide ions to react with the cation. However, that increased hydrophobicity also proved to hinder the number of QA groups that could be incorporated into the network, limiting the membrane's IEC.[73] Recently, increasing the alkyl chain spacer between the QA group and the polymer backbone has appeared to be a promising approach to produce membranes with improved alkaline stability.[10,74–76]

Due to the continued chemical instability of the QA, imidazolium cation-based AEMs have also been developed and are the most promising and widespread cation used in AEMs, aside from the QA.[53–55,65,68] Early reports of imidazolium-based AEMs demonstrated potential as they had both good ion conductivity and decent chemical stability.[77] In an effort to further improve the chemical stability, the imidazolium cation was functionalized with a variety of substituents, showing that cations with more steric hindrance had better chemical stability.[68] The result of these functionalization attempts has been the development of many different AEMs that show varied levels of chemical stability and ion conduction.[3,14,53–55,65,68,78–80] While synthesizing imidazoliums containing these various functionalities and incorporating them into AEMs with high IEC values can be synthetically challenging, developing imidazolium-based AEMs remains a very active area of research, with imidazolium-based cations being widely considered as the best potential replacement for QA.

Despite progress on the chemical stability of both QA and imidazolium cations, alkaline stability remains a serious challenge facing AEMs, which has led to the development of many different types of organic cations. The most common types of

organic cations, other than QA and imidazolium, include guanidinium, pyridinium, pyrrolidinium, triazolium, phosphonium, and sulfonium.[17,37,47,52,56,57,64,66,69] However, despite the vast number of organic cations synthesized, AEMs utilizing these different cations have demonstrated varying degrees of chemical stability, with no specific cation distinguishing itself as the best option.

The lack of concrete success for organic cations has led to the development of a new class of materials containing metal-based cations. This new class of materials includes various bis(terpyridine)-based metal cations (containing ruthenium, nickel, cobalt, iron, manganese, and zinc) and cobaltocenium cations.[11,58–61,63,81] These metal-based cations have shown high potential since both types of cations have provided excellent chemical stability with minimal degradation in fuel cell operation conditions.

While an increasingly large number of cations have been incorporated into AEMs, their impact on AEM ion conductivity remains understudied. For example, a recent review about the impact of cations on AEM properties focused solely on their impact on AEM chemical stability, without any discussion on how changing the cation would influence ion conductivity.[3] However, comparing AEMs containing different cations shows that the identity of the cation influences the water uptake and ion conductivity as well as the chemical stability (Table 1).[37,38,47,52,66,68] While these properties are summarized from various reports in literature demonstrating different properties and using various experimental conditions, the nature of the cation clearly impacts the water uptake and ion conductivity. For example, when an AEM was designed to compare a QA and an imidazolium cation, the QA-based membrane showed enhanced ion conduction over the imidazolium-based AEM, as well as enhanced water uptake.[82]

8

Furthermore, while changing the cation can improve the chemical stability of AEMs, it also complicates the challenge of understanding ion conduction in membranes since the cation's identity also influences other properties impacting ion conduction. The relationship between the materials used and the ion conductivity needs to be further explored and understood so that the field can focus on developing the polymers and cations with the highest potentials.

Table 1. Summary of properties for AEMs in the hydroxide form containing different cations. AEMs were synthesized from a variety of polymer chemistries and AEM architectures.

Cation	IEC (mmol/g)	Water Uptake (%)	Condition	Conductivity (mS/cm)[a]
QA[12]	2.2	122	60 ˚C, liquid water	156
Imidazolium[12]	2.2	74	60 ˚C, liquid water	105
Phosphonium[47]	0.67	52	22 ˚C, liquid water	22
Sulfonium[57]	1.37	15.9	80 ˚C, 100% RH	15.6
Bis(terpyridine) Ruthenium Cation[59]	1.4	126	30 ˚C, liquid water	28.6
Cobaltocenium[61]	1.92	40.2	60 ˚C, liquid water	25.1

1.3 Complexity with Elucidating the Impact of Membrane Chemistry on AEM Conductivity

Despite the impact the polymer backbone and cation identity can have on AEM properties, especially conductivity, these relationships are still poorly understood. This deficit is largely due to a lack of direct attention given to these relationships in the literature.[56,71] Only a few reports compare different types of cations, and many of these focus their efforts on understanding chemical stability, rather than ion conduction.[3,79,82–86] In order to fully explore these relationships, a comparison between different reports must be performed, however, this proves complicated for two main reasons: 1) differences in experimental conditions and 2) differences in AEM properties.

1.3.1 Differences in Experimental Conditions

A major factor that complicates uncovering the relationship between AEM structure and ion conduction is the lack of a clear consensus in the field about how to measure ion conduction.[40,68,72,73,82,84] This uncertainty leads to large differences between reports characterizing AEMs, even when similar materials are studied (Table 1). The need for a standardized approach can be best demonstrated by examining three critical experimental conditions: 1) AEM hydration, 2) system temperature, and 3) anions studied for conduction.

1.3.1.1 AEM Hydration

The hydration of an AEM is a critical factor influencing ion conduction and refers primarily to the amount of water in the network. Water molecules facilitate ion mobility by hydrating the conducting anions, allowing them to better flow through the network along with the unbound, free flowing water. Consequently, there must be enough water in the membrane to facilitate ion mobility.[87] On the other hand, too much water dilutes the ions, negating the enhancement from the increased ion mobility. These opposing effects demonstrate the complexity surrounding this critical experimental parameter.[88,89] Furthermore, the amount of water in the network impacts the degree of counterion condensation observed since an increased amount of water helps to the stabilize the charge on the polyelectrolyte allowing for an increased release of counterions.[90,91] Since counterion condensation strongly influences the percentage of free ions available for conduction, membrane hydration impacts ion conduction both through the mobility of the anions and through the percentage of free ions available for conduction.[92]

AEM hydration is typically controlled in one of two ways. The membrane is either immersed in liquid water with the conductivity experiment being conducted once the membrane has reached equilibrium swelling or it is immersed in a chamber set to a specific relative humidity (RH), most commonly 95% RH. Liquid water appears to be the more popular choice and is used because that tends to produce the best ion conduction results,[87] while 95% RH is closer to a fuel cell's operating conditions.[93] While the importance of each option is apparent, reports utilizing different levels of hydration for their conductivity experiments leads to serious difficulty in comparing their results. A report that studies an AEM at 95% RH will have significantly lower hydration than one using liquid water, and thus will demonstrate significantly lower ion conduction.

Furthermore, there is no simple normalization that can be performed to account for changes in AEM hydration, making it difficult to quantify how studying a membrane in 95% RH would compare to studying it in liquid water. The identity of the cation and the polymer backbone will control the ability of the membrane to absorb water, which will dictate how much the membrane swells when transitioned from 95% RH to liquid water. If a normalization was determined for one membrane, that normalization would be dependent on the polymer and cation studied, and thus this correction could not be applied universally to all materials. For example, one report took the same polystyrene-based material and aminated it using two different methods, one prior to crosslinking (homogeneous) and the other after crosslinking (heterogeneous) (Figure 5A).[9] When water uptake and chloride conductivity of these two materials were determined as a function of relative humidity, the homogenous sample showed a larger increase in conductivity than its heterogenous counterpart, despite the only difference being the sequence of fabrication

(Figure 5B and C). Furthermore, both water uptake and conductivity demonstrate a non-linear increase with increased membrane hydration, further demonstrating the difficulty in understanding the impact of different membrane hydration on ion conductivity.[94,95]
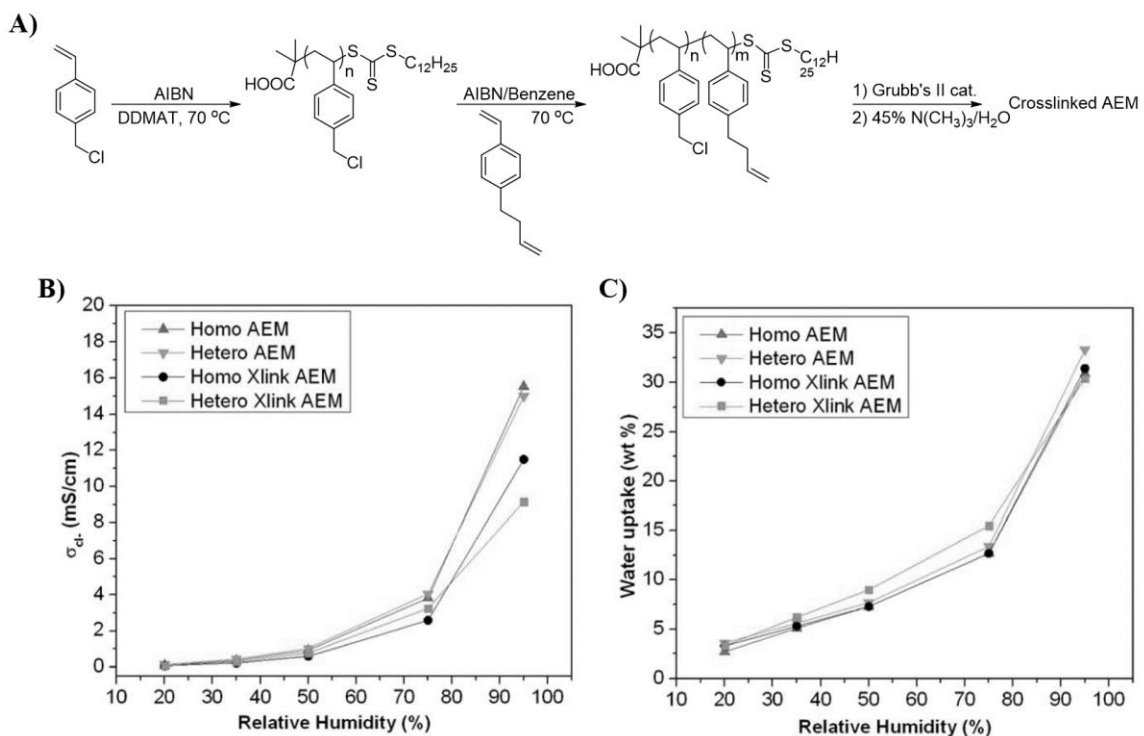
Figure 5. A) Synthetic scheme for polystyrene-based AEMs. B) Plot of chloride conductivity against relative humidity. C) Plot of the water uptake against relative humidity. Figure adapted from literature.[9]

1.3.1.2 System Temperature

Another condition that is often modulated between reports is the temperature at which conductivity experiments are performed. Increased temperature results in an increased ion conductivity due to the enhanced mobility of the conducting ions.[96,97] Three temperature conditions are typically employed: 1) 80 ˚C, 2) room temperature, and 3) a temperature range.[7,47,57,97–99] 80 ˚C is used as that temperature produces the best conductivity results and is the temperature typically observed in fuel cells during operation.[97] Running

12

experiments at room temperature is chosen because membranes generally show better stability at lower temperatures and side reactions are less likely to occur, such as the reaction between hydroxides and carbon dioxide in the air.[100–102] However, the most popular approach is to collect data as a function of temperature to encompass the entire range of temperatures typically observed in a fuel cell between warming up and cooling down the device.

The presence of multiple commonly-employed temperature conditions further demonstrates the complexity in elucidating conductivity trends based on different reports from literature. The extent to which conductivity increases is highly dependent on the materials used in the membrane and is captured by the activation energy (E_a) barrier to ion conduction, as discussed in more detail later. Since different materials demonstrate different rates of increase for ion conduction, the result for one membrane at 80 ˚C cannot accurately be corrected to compare to the result for another membrane at 30 ˚C.[103]

1.3.1.3 Anions Studied for Conduction

Beyond changes in the experimental conditions, there are also multiple anions used to measure conductivity. Hydroxide ions are known to react with CO_2 in the air to produce carbonates and bicarbonates, which have different mobilities than hydroxide ions, making it difficult to perform and analyze hydroxide ion conductivity experiments.[100–102] For this reason, other anionic species are typically studied in place of hydroxide ions, most commonly chloride, bromide, and bicarbonate ions.[27,101] Chloride and bromide ions combine synthetic ease with an inert ion, as most cations are initially synthesized from an alkyl chloride or bromide. Likewise, the bicarbonate ion demonstrates the same inert

nature, but has the benefit of being the ion observed in a fuel cell as the product from the reaction of hydroxide ions with carbon dioxide.

While utilizing alternate counterions allows for facile synthesis and experimental characterization, conductivity trends with one anion cannot be accurately correlated to conductivity trends for another anion. For example, one report showed that a series of five different nitrogen-based cations had different trends in chloride conduction when compared to hydroxide conductivity.[10] That report showed that for chloride ion conductivity a piperazine-based cation (DMP) facilitates similar conduction to a trimethylammonium-based cation (TMHA), but significantly worse hydroxide conductivity (Figure 6). Furthermore, larger anions are known to have slower diffusions, hindering their ability to be conducted in an AEM and causing complications in comparing conductivity for one anion to another.[104] Therefore, as elucidating the relationship between cation identity and ion conduction becomes more important, reports using different anions for conduction will seriously hamper our ability to understand that relationship.
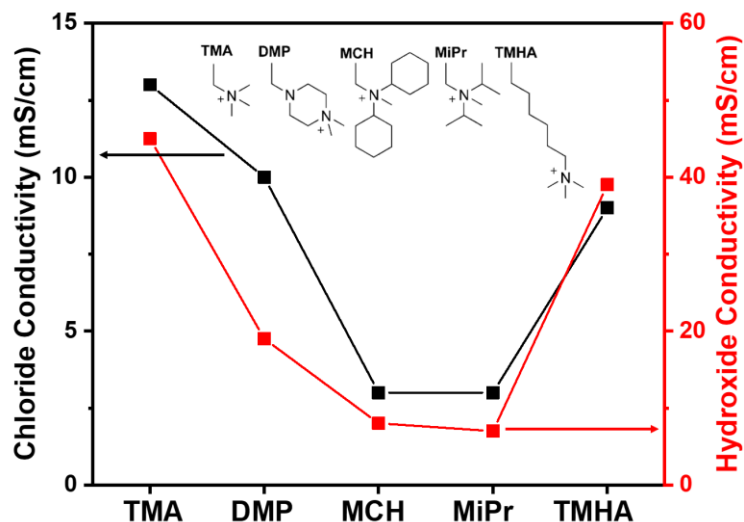
Figure 6. Plot showing the chloride conductivity (black, left-axis) and hydroxide conductivity (red, right-axis¬), for five nitrogen-based AEMs where the structures for TMA, DMP, MCH, MiPr, and TMHA are shown as an inset.[10]

1.3.2 Differences in AEM Properties

Understanding the relationship between the materials used in AEMs (cationic head group and polymer backbone) and ion conduction is also complicated by the impact of the materials on various AEM properties. While developing a standardized approach to characterizing AEMs would be possible, understanding the effects of different materials on AEM properties is significantly more challenging. AEM properties are difficult to handle since they are due to the nature of the materials, as opposed to choices made by researchers. The AEM properties typically impacted by changing cation identity or polymer chemistry include: 1) water uptake, 2) morphology, and 3) IEC.

1.3.2.1 Water Uptake

Earlier, the hydration of the membrane was discussed in terms of the influence from external factors, such as the degree of humidity in the experimental system. However, AEM hydration is also influenced by the inherent nature of the cation and type of polymer

15

incorporated. It is well known that increasing the hydrophilicity of the polymer increases the water uptake within the network.[63,105] However, the impact of the cation's identity on the water uptake in an AEM is just as important. When reports comparing trimethylammonium- and imidazolium-based cations are studied, it becomes clear that the trimethylammonium facilitates more water uptake than its imidazolium counterpart (Table 1).[12,79,82,83] For example, when quaternary ammonium-, imidazolium-, and methylimidazolium-based AEMs were synthesized at similar IEC values, the QA-based AEM had the highest water uptake at 25 ˚C (38.9 wt%), followed by the methylimidazolium-based AEM (24.3 wt%), and the imidazolium-based AEM had the lowest water uptake (10.1 wt%).[82] Accordingly, it quickly becomes difficult to attribute differences in conductivity to either cation identity or water uptake, since the two cannot be easily decoupled.

1.3.2.2 Morphology

One key design feature utilized extensively in AEMs to improve ion conduction is microphase separation. It has been shown that introducing phase separation to an AEM can drastically increase ion conductivity, as well as improve mechanical and thermal stabilities, through the formation of interconnected hydrophilic, ion containing channels.[29,30,32–35,81,106–109] These hydrophilic channels allow for more efficient flow of water molecules and hydrated ions throughout the network. In order for phase separation to occur, the chemical mismatch between the hydrophobic matrix and the hydrophilic, ion-containing phase must be large enough that they overcome the entropic penalty for phase separation and form segregated phases as opposed to remaining mixed, indicated through the Flory-Huggins interaction parameter, χ.[33]

16

Therefore, it is important to understand the impact that the nature of the cation and the polymer chemistry used have on the capability of a network to phase separate, as AEMs are typically formed from a hydrophobic polymer matrix and a hydrophilic, ionic pendant group.[29,30,106–109] The mismatch between the two materials is strongly influenced by the polarity of the two species, and the polarity difference is known to strongly influence the morphology obtained through phase separation.[30] A more disordered morphology is obtained as the polarity difference between the immiscible phases decreases, enhancing the mechanical and conductive properties of AEMs.[30,33,110] Therefore, changing the polymer backbone or the nature of the cation will alter the difference in polarity between the two components, changing the microphase separation of the network.

The channel size has also been well established to impact the ion transport properties. Channels smaller than 5 nm have been shown to facilitate better water and ion mobility, although larger channels have better channel continuity, leading to enhanced ion conductivity.[30,111–115] Since the cationic head groups are positioned in the hydrophilic channel, and different cations interact with the water molecules differently, the size and identity of the cation can significantly influence the size of the channels through their bulkiness and ability to structure water molecules. Therefore, as the sizes of those channels change, the ease with which water and ions flow through the network will be impacted, leading to changes in the ultimate ion conduction.

1.3.2.3 IEC

Another key property of the AEM that influences its ion conductivity is its IEC. Since this value indicates the number of cations incorporated into the network, increasing the IEC leads to better ion conduction.[5,31] As such, reports will often strive for the highest IEC

possible in the specific chemical platform to achieve the best ion conduction possible. The drive for the highest possible IEC results in a wide range of IEC values seen throughout literature, especially as different types of cations and polymer matrices are incorporated into the network. The range in IEC values observed becomes more apparent as different cations are used because changing the identity of the cation can have an impact on the efficiency with which cations can be incorporated into the network. For example, as cations become more hydrophobic and increase in size, it can be difficult to achieve high IEC values.[71–73] It is difficult to compare AEMs at one IEC value to membranes with higher IEC values, as there is no simple correction that can be applied to membranes with different IEC values. This inability to easily correct for the IEC value is due in large part to its influence on other properties, such as water uptake.

1.4 Currently Identified Bulk Parameters Used to Understand Conductivity

Up to this point, the polymer backbone's and cationic head group's impact on AEM properties have been discussed, especially in regard to ion conductivity. Due to the complexity with understanding the relationship between the materials used and AEM ion conductivity, parameters that can decouple or operate independently of AEM water uptake and ion conduction must be developed.[1,5,24,25,27,36,37,105] Despite very little direct attention being addressed to understanding this relationship and developing these parameters, over time four parameters have been identified and used to better understand ion conduction: 1) hydration number, 2) ion concentration, 3) the ratio of the effective diffusion coefficient for the conducting ion, D, to the dilute solution diffusivity for the ion, D_o (D/D_o), and 4) the activation energy (E_a) of ion conduction.[11,32,35,54,81,103] All of these parameters represent

attempts to account for differences in water uptake, IEC values, and bulk ion mobility and their influence on ion conduction within the network.

1.4.1 Hydration Number and Ion Concentration

The hydration number refers to the number of water molecules present within the network per cation incorporated and can be expressed through equations 1 and 2:[116]

$$\lambda = \frac{1000 \; x \; WU}{M_{H_2O} \; x \; IEC} \tag{1}$$

$$WU = \frac{m_{hyd} - m_{dry}}{m_{dry}} \times 100\% \tag{2}$$

where WU is the water uptake in the AEM as a weight percent, M_{H_2O} is the molecular mass of water (18.015 g/mol), IEC is the calculated IEC of the membrane, m_{hyd} is the hydrated mass, and m_{dry} is the dry mass.[11,117] Since λ is proportional to WU/IEC, it accounts for the impact of the cation content on the water uptake and is used to relate that relationship to the ion conduction. A larger λ corresponds to an increased hydration of the ions present in the network which corresponds to enhanced ion mobility and conduction.[87] However, this parameter only describes the amount of bulk water present within a network per cation. It does not provide insight into the state of the water. In ion conducting membranes, a large portion of the water is bound to the cations and is immobile, meaning it is not useful for enhancing ion mobility.[118–121] Therefore, understanding the ratio of bound water to free flowing water is paramount in understanding the hydration's impact on ion conduction and is not addressed with this λ parameter. Furthermore, while increasing the λ is expected to increase the ion conduction, such a correlation is not always observed, possibly due to the limited knowledge of the state of water within the network (Figure 7).[11]
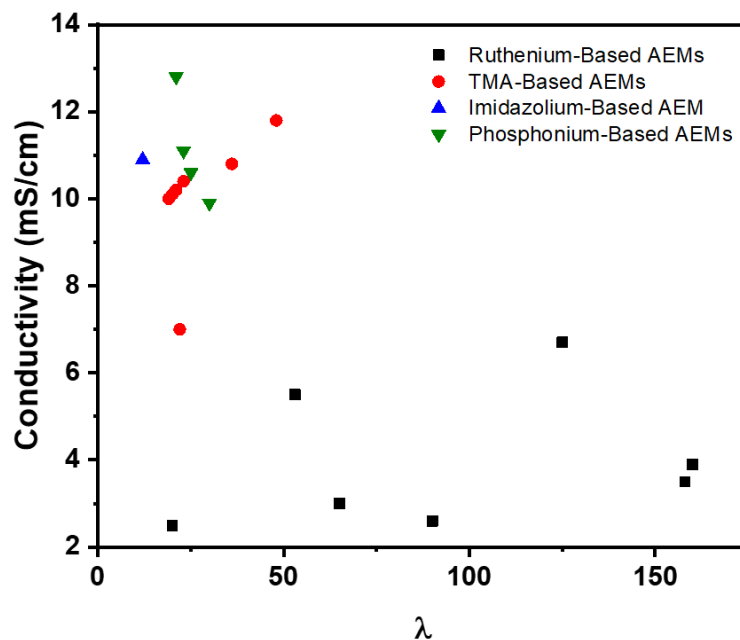
Figure 7. Plot of bicarbonate conductivity versus λ for ruthenium-, tetramethylbisphenol-, imidazolium-, and phosphonium-based AEMs at various IECs. Figure an adaption from literature.[11]

While understanding the impact of cation content on water uptake is crucial for understanding ion conduction, understanding the reverse is also critical, which is why ion concentration is another parameter frequently used to understand ion conduction. Ion concentration relates to how densely packed the ions are within an AEM, where more ions per unit volume is assumed to enhance ion conduction, and is represented by equation 3:[11]

$$c = \frac{\rho \; x \; IEC}{1 + WU} \tag{3}$$

where c is the concentration of ions in the swollen network (mmol ion/mL of AEM and water combined) and ρ is the density of the dried membrane measured by determining its dried volume and mass. Ion concentration is an attempt to account for the impact of water uptake on the ion content in the network.

Understanding both parameters is critical to understanding ion conduction since they are inverse of each other and increasing one parameter decreases the other.[72] However, this

interdependence also underlines the difficulty in using these two parameters to describe ion conduction in AEMs. It is difficult to optimize both parameters and nearly impossible to de-couple the impact of each parameter on the ultimate ion conductivity. While that is an important reason to understand both parameters, it also expresses the need to develop additional parameters to explain ion conduction.

1.4.2 D/Do and Ea

Given the interdependence between λ and ion concentration, exploring the mobility of ions within an AEM and how that impacts ion conduction has received increasing attention. Studying the mobility of the conducting ions is traditionally accomplished with two parameters: D/D_o and E_a. D/D_o corresponds to the diffusion of the anion in the network and is an attempt to elucidate the efficiency with which it moves through the network.[35] This parameter can be understood through the ratio of equation 4/equation 5:

$$D = \frac{\sigma RT}{cz^2 F^2} \tag{4}$$

$$D_o = \frac{\mu k_B T}{q} \tag{5}$$

where σ is the measured conductivity, R is the gas constant, T is the temperature, c is the ion concentration, z is the valence charge of the cation, F is Faraday's constant, μ is the dilute solution ion mobility, k_B is the Boltzmann constant, and q is the charge of the anion. D/D_o is an effective parameter for comparing conductivity from different anions as it normalizes the conductivity based on the efficiency with which an anion diffuses as compared to itself, which accounts for the differences in ion mobility for various ions.

However, despite this benefit, trends in D/D_o are rarely explained in detail or correlated between different types of membranes. Figure 8 summarizes the impact of D/D_o on bicarbonate conductivity for AEMs functionalized with ruthenium-,

21

tetramethylammonium-, imidazolium-, and phosphonium-based cations.[11] This data demonstrates that within one type of AEM a general correlation between D/D_o and ion conductivity may exist, but that correlation does not exist between AEMs with different cations. Furthermore, D/D_o is typically only discussed as the overall bulk diffusion of ions within the network, with no exploration into different states of diffusion. For example, it has been shown that anions closer to the polymer matrix diffuse more quickly than anions in the center of a hydrophilic channel.[87,92] Expanding upon the knowledge of this parameter would provide a deeper understanding of the impact of AEM structure and cation identity on ion conduction.
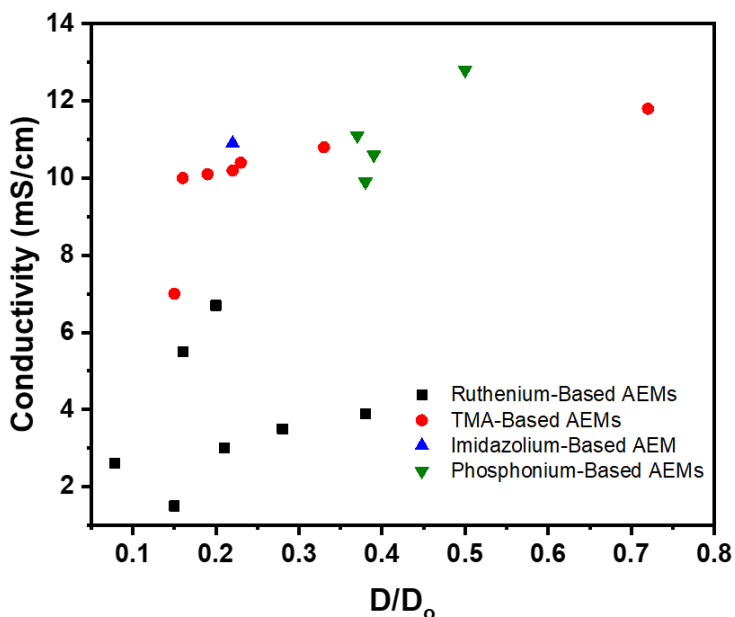
Figure 8. Plot of bicarbonate conductivity versus D/Do for ruthenium (black squares)-, tetramethylbisphenol (TMA, red circles)-, imidazolium (blue triangle)-, and phosphonium-based (green inverted triangle) AEMs at various IECs. Figure adapted from literature.[11]

The final parameter typically discussed is the E_a, which corresponds to the kinetic barrier to ion conduction within a network, and can be understood through equation 6:[11]

$$\ln(\sigma) = \ln(\sigma_o) - \frac{E_a}{RT} \tag{6}$$

where σ is the ion conductivity, σ_o is the pre-exponential factor, R is the gas constant, and T is the temperature. Theoretically, the E_a is a critical parameter for ion conduction as it describes the difficulty with which ion conduction can initially occur, but it is rarely discussed in detail in literature.[103] Furthermore, when discussed, rarely does the E_a correlate well to differences in ion conductivity, leading to this parameter receiving less attention than the other three parameters discussed.

1.5 Molecular-Level Parameters

All four of the parameters typically used to describe ion conduction (λ, ion concentration, D/D_o, and E_a) represent bulk membrane properties. While these bulk parameters inform researchers of certain aspects of AEM ion conductivity, it is clear that they do not fully capture the ion conduction phenomenon. Given the complexity with using those four parameters, the field has begun to explore other parameters that can be identified to explain and potentially predict ion conduction in AEMs. Since ion conductivity in AEMs is both a bulk- and molecular-level phenomenon, seen through both the bulk membrane hydration and molecular level ion mobility, the idea of understanding and predicting ion conduction through the development of a molecular-level parameter has recently been proposed.

Very few reports have explored the idea of developing a molecular-level understanding of ion conduction, but of the few that have, the importance of the molecular-level association strength between the cation and its counter anion has proven to be critical.[12,63] Since the counterion must first dissociate from the cation for conductivity to occur, a weaker association between the two ions would allow for more facile dissociation and lead to enhanced ion conductivity.[90] The impact of ion dissociation was first indicated in a report

studying the difference in ion conduction between materials with chloride and bicarbonate ions to identify parameters that can enhance ion conduction in these membranes.[27] That report concluded that the percentage of free ions in the network is a major factor limiting ion conduction in AEMs, proposing that increasing the steric hindrance around the cation or the basicity of the cation could lead to a larger percentage of free ions, due to a weaker association strength between the cation and its counterion.

In addition to that initial report, a recent study explored the impact of the Arrhenius basicity of different iminium cations on AEM chemical stability and ion conductivity.[12] The Arrhenius basicity of the cation was determined from the ion-exchange ratio of AEMs from the hydroxide to chloride form (termed BI) and represents the dissociation constant for the ion pair. This report correlated the Arrhenius basicity to the ion conductivity of the AEMs, showing that as the basicity of the cation increased, the ion conductivity also increased (Figure 9). Understanding a material's Arrhenius basicity could be used to predict the AEM's ultimate ion conductivity, since a larger basicity correlates to a weaker cation-counterion association.
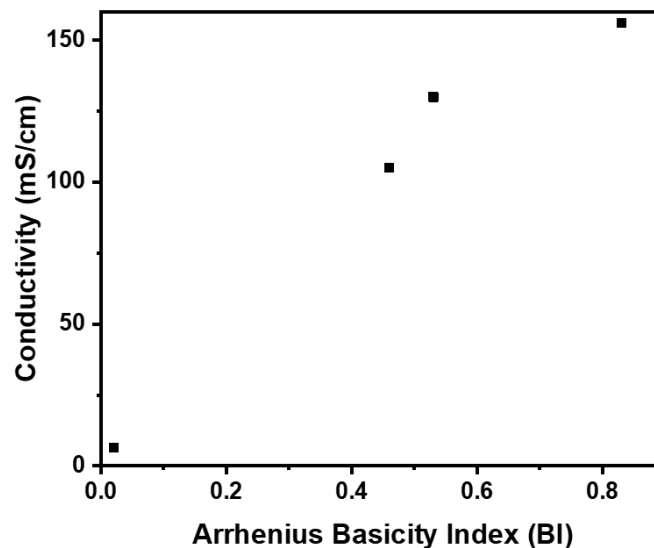
Figure 9. Plot of hydroxide conductivity versus the Arrhenius basicity of a N-methylbenzimidazole (BI = 0.02)-, N-methylimidazole (BI = 0.46)-, 4-(N,N-dimethylamino)pyridine (BI=0.53)-, and trimethylammonium (BI=0.83)-based AEM. Data adapted from literature.[12]

This Arrhenius basicity approach demonstrates the critical importance of the molecular-level association strength between the cations used in AEMs and their counterions. It shows that decreasing the association strength leads to enhanced ion conduction in the AEM. Gaining a deeper understanding of this molecular-level parameter will afford a better understanding of ion conduction and ultimately allow for the prediction of AEM conductivity, permitting the field to focus its efforts on the polymers and cations with the highest potential.

1.6 Format of the Dissertation

As described above, there is an understudied challenge for the design of an ideal AEM: elucidating the impact of both the cation's identity and polymer backbone on AEM conductivity. In this dissertation, we describe our contribution to developing that relationship and how that relationship can be used to inform the design of AEMs to have enhanced ion conductivity. Through the design and synthesis of metal cation-based AEMs

we isolated the impact of the cation's identity on AEM conductivity and used the thermodynamics of dissociation between the cation and its counterion to explain the conductivity data obtained.

As such, Chapter 2 will discuss the design and synthesis of metal cation-based AEMs synthesized using ring-opening metathesis polymerization (ROMP) to allow the incorporation of six different metal cations with four different counterions. Chapter 2 will also discuss the synthesis of AEMs specifically designed to produce micro-phase separation fabricated using the robust thiol-ene reaction. Chapter 3 will explore the two types of AEMs for their various properties, such as water uptake, mechanical stability, and ion conductivity, and correlate cation identity to those properties. Chapter 3 will also explore the traditionally used bulk membrane parameters to attempt to explain ion conductivity trends. Chapter 4 will utilize isothermal titration calorimetry (ITC) to capture the thermodynamics of dissociation quantifying the cation-counterion association strength (CCAS) and correlate the CCAS to ion conduction. Chapter 5 explores the CCAS of quaternary ammonium-based cations to identify cation design features that weaken that association strength. Finally, Chapter 6 presents the main conclusions discussed throughout this dissertation and offers potential next steps for this research.

CHAPTER 2

SYNTHESIS OF METAL CATION-BASED AEMS

2.1 Introduction

Anion exchange membranes (AEMs) are notorious for having low ion conductivity and poor chemical stability in the operating conditions of fuel cells, namely high alkaline, high temperature conditions.[1,5,17,26–30] Metal cation, ring-opening metathesis polymerization (ROMP)-based AEMs have demonstrated potential as a new class of materials available for use in AEMs as they have shown excellent chemical stability and comparable ion conductivity.[11,59] These materials were synthesized from a norbornene functionalized terpyridine ligand used to form a heteroleptic, bis(terpyridine) ruthenium complex monomer that was polymerized in the presence of dicyclopentadiene (DCPD). The combination of the heteroleptic ruthenium monomer and DCPD allowed for the systematic control of both crosslinking density and ion exchange capacities (IEC). Those studies demonstrated that a crosslinker to ruthenium monomer ratio of 5:1 showed optimal mechanical and conductive properties. Despite that potential, ruthenium is a rare metal and thus not ideal for use in AEMs.[122–125] This ROMP-based platform represents an ideal chemical approach towards incorporating a variety of different metal cations as the metal center of bis(terpyridine) complexes can easily be changed. The ability to easily change the nature of the metal cation provides an optimal approach to studying the impact of a cation's identity on AEM properties. Therefore, this work expands upon those initial

reports to incorporate a variety of different metal cations including ruthenium, nickel, cobalt, iron, zinc, and manganese, with the synthesis of these monomers and their subsequent AEMs described here. Furthermore, through the functionalization of these terpyridine ligands, the incorporation of metal cations into different synthetic platforms can also be easily accomplished, as demonstrated here with the thiol-ene reaction.

2.2 Experimental

2.2.1 Thiol-Ene-Based AEMs

2.2.1.1 Materials

2,2-azobis(isobutryonitrile) (AIBN, Sigma Aldrich) was purified by recrystallization from methanol. Tetrahydrofuran (Fisher Scientific) was dried over sodium under N_2 and then distilled before use. *Exo*-5-norbornene-2-carboxylic acid, lithium aluminum hydride (LiAlH$_4$), triethylamine (TEA), 4-(dimethylamino)pyridine (DMAP), *p*-toluenesulfonyl chloride (Tosyl-Cl), dimethylformamide (DMF), cesium carbonate, 3,5-dihydroxybenzyl alcohol, dimethyl sulfoxide (DMSO), potassium hydroxide (KOH), 4-chloro-2,2':6',2''-terpyridine, chloroform, irgacure 2959, 2,2'-(ethylenedioxy)diethanethiol, 4-vinylbenzyl chloride, sodium hydride (NaH, powder), styrene, toluene, 2-cyano-2-propyl dodecyl trithiocarbonate, nickel(II) chloride hexahydrate, dichloromethane (DCM), methanol, sodium sulfate, ethyl acetate, hexane, and diethyl ether were purchased from Sigma Aldrich, Alfa Aesar, Acros Organics, Fisher Scientific or Tokyo Chemical Industry and were used as received.

2.2.1.2 Synthesis of Monomer 3

2.2.1.2.1 5-norbornene-2-methanol.

Exo-5-nobornene-2-carboxylic acid (1.0 g, 7.2 mmol), was dissolved in THF (22.5 mL) and cooled in an ice bath. Lithium aluminum hydride solution in THF (2.4 M, 2.26 mL) was added dropwise to the solution, the flask was removed from the ice bath and the reaction was stirred overnight at room temperature. The flask was then cooled in an ice bath and quenched with RO water. The precipitated salt was filtered and the THF was removed *in vacuo*. The remaining oil was diluted with water and the product was extracted with chloroform. The chloroform was dried over Na_2SO_4 and removed *in vacuo* providing precursor monomer, (yield 0.863 g, 96 %) as a clear liquid product. δH (500 MHz, $CDCl_3$) 6.10 (2H, m), 3.71 (1H, m), 3.55 (1H, m), 2.83 (1H, s), 2.76 (1H, s), 1.62 (1H, m), 1.37-1.20 (3H, m), 1.12 (1H, m).

2.2.1.2.2 Monomer 1.

Monomer **1** was synthesized following an adaption of previously published procedures.[126] A mixture of Tosyl–Cl (9.2 g, 0.048 mol, 1.2 eq.), DMAP (catalytic amount), 5-norbornene-2-methanol (5 g, 0.04 mol, 1 eq.) and DCM (130 mL) were stirred in an ice bath and purged with N_2 gas. Once the solution was chilled, TEA (8.4 mL, 0.06, 1.5 eq.) was added dropwise. The solution was stirred under an N_2 atmosphere overnight as the solution warmed to room temperature. After the reaction was complete, the solution was washed with RO water three times after which the organic layer was dried with sodium sulfate. The salt was filtered off, solvent was removed, and the crude product was purified using a CombiFlash Isco automated silica column with an eluent mixture of ethyl acetate and hexanes. A gradient from 0-10% ethyl acetate over 40 minutes at a flow rate of 25

mL/min was sufficient for separation. Upon removal of solvent by rotary evaporation, the product was obtained as a colorless oil, which became a white solid upon drying under high vacuum and freezing at -20 °C (yield 78%). ^{1}H NMR (CDCl$_3$, ppm, 500 MHz): 7.80 (2H, d), 7.28 (2H, d), 6.05 (2H, br), 4.08 (1H, dd), 3.91 (1H, t), 2.80 (1H, s), 2.69 (1H, s), 3.73 (1H, m), 1.30 (1H, d), 1.22 (1H, dt), 1.16 (1H, d), 1.07 (1H, m). ^{13}C NMR (CDCl$_3$, ppm, 500 MHz): 144.68, 137.08, 135.99, 133.24, 129.84, 127.90, 74.39, 44.82, 43.36, 41.57, 38.19, 29.35, 21.66.

2.2.1.2.3 Monomer 2.

A mixture of monomer **1** (4.4 g, 0.016 mol, 2.2 eq.), 3,5-dihydroxybenzyl alcohol (1.01 g, 7.2 mmol, 1 eq.), and DMF (30 mL) was stirred while being purged with N$_2$ gas. Once purged, Cs$_2$CO$_3$ (5.63 g, 0.016 mol, 2.2 eq.) was added as a powder. The reaction mixture was left under an N$_2$ atmosphere and was stirred at 80 °C overnight. After complete conversion, the mixture was cooled to room temperature and diluted with DI water. The product was then extracted with diethyl ether three times and dried over sodium sulfate. The solvent was removed via rotary evaporation, where heptane was used to facilitate removal of residual DMF. The crude product was purified using a CombiFlash Isco automated silica column with an eluent mixture of ethyl acetate and hexanes. A gradient of 0-15% ethyl acetate over the first 20 minutes, 15-35% ethyl acetate over the next ten minutes and 35-50 % over the final 10 minutes was used to obtain sufficient separation at a flow rate of 25 mL/min. The solvent was removed by rotary evaporation, and after drying under high vacuum, the product was obtained as a cream colored solid (yield 79%). ^{1}H NMR (CDCl$_3$, ppm, 500 MHz): 6.53 (2H, br), 6.42 (1H, br), 6.15 (2H, m), 6.10 (2H, m), 4.63 (2H, d), 4.01 (2H, dt), 3.83 (2H, t), 2.86 (4H, br), 1.88 (2H, br), 1.35 (6H, m), 1.23

(2H, m). ^{13}C NMR (CDCl$_3$, ppm, 500 MHz): 160.59, 143.25, 136.86, 136.47, 106.13, 100.67, 72.41, 65.47, 45.07, 43.74, 41.62, 38.57, 29.68. HRMS-ESI (m/z): calcd for C$_{23}$H$_{28}$O$_3$, 352.20; found 353.20 [M + H]$^+$.

2.2.1.2.4 Monomer 3.

To DMSO (19 mL) was added KOH (0.755 g, 0.013 mol 5.73 eq.) and **2** (1 g, 2.8 mmol, 1.2 eq.). The mixture was then stirred at 60 °C for 30 minutes under N$_2$ gas, during which the solution turned orange. 4-chloro-2,2':6',2''-terpyridine (0.63 g, 2.3 mmol, 1 eq.) was then added to the solution as a powder and the solution was allowed to react for 6 hours at 60 °C. After 6 hours, a precipitate formed. The solution was then cooled to room temperature, added to methanol (180 mL), and placed in the -20 °C freezer overnight to fully precipitate the product. The precipitate was filtered, producing the product as an off-white powder (yield 87%) ^{1}H NMR (CDCl$_3$, ppm, 500 MHz): 8.7 (2H, br), 8.63 (2H, d), 8.12 (2H, s), 7.85 (2H, dt), 7.33 (2H, m), 6.67 (2H, d), 6.47 (1H, s), 6.15 (2H, m), 6.10 (2H, m), 5.26 (2H, s), 4.04 (2H, m), 3.85 (2H, t), 2.87 (4H, br), 1.89 (2H, m), 1.33 (6H, m), 1.26 (2H, m). ^{13}C NMR (CDCl$_3$, ppm, 500 MHz): 166.93, 160.58, 157.21, 156.11, 149.07, 138.30, 136.85, 136.51, 123.88, 121.39, 107.66, 106.67, 101.28, 72.45, 69.92, 45.09, 43.75, 41.63, 38.58, 29.67. HRMS-ESI (m/z): calcd for C$_{38}$H$_{37}$N$_3$O$_3$, 583.28; found 584.29 [M + H]$^+$.

2.2.1.2.5 Homopolymerization of Monomer 3

Monomer **3** (0.1 g, 0.17 mmol, 1 eq.) and 2,2'-(ethylenedioxy)diethanethiol (0.028 mL, 0.17 mmol, 1 eq.) were dissolved in DCM (0.48 mL). Irgacure 2959 (2 mg, 0.009 mmol, 5 wt %) was then added and once dissolved, the solution was irradiated with UV light (365 nm) for one hour. The solution was then diluted with CHCl$_3$ and precipitated into methanol

three times. The product was dried under high vacuum and obtained as a white solid (90 %).

2.2.1.2.6 Synthesis of Monomer 4

Monomer **4** was synthesized following an adaption from a previously published procedure.[33] Into an oven-dried round bottom flask sodium hydride (0.077g, 3.2 mmol, 2 eq.) and DMF (5 mL) with stir bar were added. The flask was placed in an ice bath and purged with N_2 gas. 5-norbornene-2-methanol (0.2g, 1.6 mmol, 1 eq.) was added dropwise over the course of 5 minutes. After stirring for 15 min., 4-vinylbenzyl chloride (0.249 mL, 1.8 mmol, 1.1 eq.) was added and the reaction was stirred overnight as it warmed to room temperature. The mixture was quenched with methanol, then extracted from water with ethyl acetate. After drying, the product was purified via silica column chromatography in a mixture of hexanes and toluene (gradient from a ratio of 4:1 to 1:1, hexanes:toluene) (yield 54%). ^{1}H NMR (CDCl$_3$, ppm, 500 MHz): 7.40 (2H, d), 7.30 (2H, d), 6.72 (1H, dd), 6.11 (1H, m), 6.05 (1H, m), 5.75 (1H, d), 5.23 (1H, d), 4.52 (2H, s), 3.51 (1H, dd), 3.36 (1H, t), 2.79 (2H, br), 1.73 (1H, m), 1.27 (3H, m), 1.11 (1H, m).

2.2.1.2.7 Polymerization of Monomer 4

2.2.1.2.7.1 Copolymerization of monomer 4 with styrene.

Into a flask containing a stir bar, styrene (2.48 mL, 0.022 mol), monomer **4** (0.25 g, 1 mmol), AIBN (0.006 g, 0.04 mmol), 2-cyano-2-propyl dodecyl trithiocarbonate (0.063 g, 0.18 mmol) and toluene (2.6 mL) were added. The solution was degassed with N_2 followed by three cycles of freeze-pump-thaw to ensure full removal of oxygen. The reaction flask was then immersed in an 80 °C oil bath and was allowed to stir for 16 hours, or until 50 % conversion was attained. The reaction products were then cooled to room temperature,

precipitated into methanol three times and dried under vacuum to afford the product **CP4** as a yellow precipitate.

2.2.1.2.7.2 Homopolymerization of monomer 4.

Into a flask containing a stir bar, monomer **4** (1 g, 4.2 mmol), AIBN (0.0024 g, 0.01 mmol), 2-cyano-2-propyl dodecyl trithiocarbonate (0.025 g, 0.07 mmol) and toluene (1 mL) were added. The solution was degassed with N_2 followed by three cycles of freeze-pump-thaw to ensure full removal of oxygen. The reaction mixture was then heated with an 80 °C oil bath and was allowed to stir for 16 hours. It was then cooled to room temperature, precipitated into methanol three times and dried under vacuum to afford the product **HP4** as a yellow precipitate.

2.2.1.2.8 Synthesis of Anion Exchange Membranes

2.2.1.2.8.1 General Procedure.

Into a 22 mL scintillation vial, the polystyrene crosslinker, either **CP4** or **HP4**, **3**, 2,2'-(ethylenedioxy) diethanethiol and NMP were added. The solution was vortexed until all compounds completely dissolved. Next, nickel(II) chloride hexahydrate and Irgacure 2959 were added and then vortexed until completely dissolved. The reaction mixture was then syringed into a rectangular Teflon mold that was then covered with a glass slide to allow UV light through. The solution was irradiated with UV, 365 nm, light for 2 hours after which it was placed into liquid water to dialyze out the NMP and any unreacted monomers and photoinitaitor. The membrane was left in the water for 2 days, during which the water was changed every few hours. The resulting transparent, brown membrane was then stored in liquid water at room temperature.

2.2.1.2.8.2 CP4-5Ni.

A general procedure was followed with the amounts: **CP4** (0.015 g), **3** (0.0177 g, 0.03 mmol), 2,2'-(ethylenedioxy) diethanethiol (0.0059 mL, 0.036 mmol), NMP (0.16 mL), nickel(II) chloride hexahydrate (3.6 mg, 0.015 mmol) and Irgacure 2959 (2-4 mg, 0.009-0.018 mmol).

2.2.1.2.8.3 CP4-10Ni.

A general procedure was followed with the amounts: **CP4** (0.01 g), **3** (0.0237 g, 0.04 mmol), 2,2'-(ethylenedioxy) diethanethiol (0.0073 mL, 0.045 mmol), NMP (0.17 mL), nickel(II) chloride hexahydrate (4.8 mg, 0.02 mmol) and Irgacure 2959 (2-4 mg, 0.009-0.018 mmol).

2.2.1.2.8.4 CP4-20Ni.

A general procedure was followed with the amounts: **CP4** (0.05 g), **3** (0.0237 g, 0.04 mmol), 2,2'-(ethylenedioxy) diethanethiol (0.0069 mL, 0.042 mmol), NMP (0.16 mL), nickel(II) chloride hexahydrate (4.8 mg, 0.02 mmol) and Irgacure 2959 (2-4 mg, 0.009-0.018 mmol).

2.2.1.2.8.5 HP4-5Ni.

A general procedure was followed with the amounts: **HP4** (0.005 g), **3** (0.0304 g, 0.052 mmol), 2,2'-(ethylenedioxy) diethanethiol (0.0102 mL, 0.063 mmol), NMP (0.19 mL), nickel(II) chloride hexahydrate (6.2 mg, 0.026 mmol) and Irgacure 2959 (2-4 mg, 0.009-0.018 mmol).

2.2.1.2.8.6 HP4-10Ni.

A general procedure was followed with the amounts: **HP4** (0.0025 g), **3** (0.0304 g, 0.052 mmol), 2,2'-(ethylenedioxy) diethanethiol (0.0093 mL, 0.057 mmol), NMP (0.176 mL), nickel(II) chloride hexahydrate (6.2 mg, 0.026 mmol) and Irgacure 2959 (2-4 mg, 0.009-0.018 mmol).

2.2.1.2.8.7 HP4-20Ni.

A general procedure was followed with the amounts: **HP4** (0.0015 g), **3** (0.0364 g, 0.062 mmol), 2,2'-(ethylenedioxy) diethanethiol (0.0107 mL, 0.066 mmol), NMP (0.2 mL), nickel(II) chloride hexahydrate (7.4 mg, 0.031 mmol) and Irgacure 2959 (2-4 mg, 0.009-0.018 mmol).

2.2.2 ROMP-Based AEMs

2.2.2.1 Materials

Tetrahydrofuran (Fisher Scientific) was dried over sodium under nitrogen gas (N_2) and then distilled before use. *Exo*-5-norbornene-2-carboxylic acid, lithium aluminum hydride ($LiAlH_4$), dimethyl sulfoxide (DMSO), potassium hydroxide (KOH), 4-chloro-2,2':6',2''-terpyridine, nickel(II) chloride hexahydrate, cobalt(II) chloride hexahydrate, ruthenium(III) chloride hydrate, manganese (II) chloride anhydrous, zinc chloride, iron (II) chloride tetrahydrate, dicyclopentadiene (DCPD), Grubb's 2nd generation catalyst (G2), n-ethylmorpholine, dihydroxyl-terminated poly(ethylene oxide) (PEO), triphenyl phosphine, diisopropyl azodicarboxylate (DIAD), 4-toluenesulfonyl chloride, 4-(dimethylamino)pyridine (DMAP), dimethylformamide (DMF), sodium hydride, dichloromethane (DCM), methanol, chloroform, sodium sulfate, ethyl acetate, hexane, and

diethyl ether were purchased from Sigma Aldrich, Alfa Aesar, Acros Organics, Fisher Scientific, or Tokyo Chemical Industry and were used as received.

2.2.2.2 Metal Cation Monomer Synthesis.

2.2.2.2.1 Norbornene-Terpyridine Ligand (P2).

P2 was synthesized as an adaption of a previous report.[59] 5-norbornene-2-methanol (2.0 g, 0.016 mol) was added to a flask containing KOH (2.6 g, 0.046 mol) in DMSO (40 mL) and was heated at 75 °C for 2 hours. 4'-chloro-2,2':6',2"-terpyridine (2.16 g, 0.0081 mol) dissolved in DMSO (40 mL) was heated at 75 °C for 2 hours then poured into the flask containing **P1**. The mixture was stirred for 48 hours at 80 °C. Once cooled, the mixture was poured into cold RO water and the product extracted with ethyl acetate. The ethyl acetate was dried over Na_2SO_4 and removed *in vacuo*. Pure **P2** (yield 2.43 g, 86 %), was recrystallized from methanol and obtained as off-white crystals. δH (500 MHz, $CDCl_3$) 8.76 (4H, br), 8.15 (2H, br), 7.99 (2H, br), 7.45 (2H, br), 6.15 (2H, m), 4.38 (1H, m), 4.21 (1H, m), 2.91 (2H, d), 1.97 (1H, m), 1.39 (4H, m).

2.2.2.2.2 Homoleptic Metal Complex General Procedure.

P2 dissolved in DCM was added to the appropriate metal chloride salt dissolved in methanol in a round bottom flask with stir bar. The solution was stirred at room temperature overnight. The solvent was removed *in vacuo* and the solid was dried under vacuum. The resulting product was used without further purification unless otherwise stated.

2.2.2.2.3 Ruthenium Complex. P2

(0.5 g, 1.4 mmol) and $RuCl_3 \cdot 3H_2O$ (0.175 g, 0.67 mmol) were dissolved in methanol (125 mL) and stirred under reflux for 2 hours. *N*-ethylmorpholine (0.147 mL, 1.1 mmol) was added and the solution was stirred under reflux overnight. The solution turned a deep

red/brown color as the reaction went. The methanol was removed *in vacuo* and the resulting deep red powder was washed with a mixture of cold RO water and CHCl$_3$. The red precipitate was then filtered and dried resulting in the pure product. **M2** (yield 0.43 g, 79 %). IR v_{max}/cm^{-1} 3343, 2963, 1606, 1542, 1466, 1417, 1396, 1358, 1339, 1283, 1207, 1158, 1114, 1040, 1022, 1001, 982, 902, 859, 787, 758, 712, 696**.** δH (500 MHz, CD$_3$OD) 8.72 (4H, d, 8.2), 8.63 (4H, s), 7.98 (4H, t, 7.8), 7.51 (4H, d, 5.2), 7.26 (4H, t, 6.6), 6.26 (4H, m), 4.67 (2H, m), 4.52 (2H, t, 9.2), 3.08 (2H, s), 3.02 (2H, s), 2.17 (2H, m), 1.63 (2H, d, 8.5), 1.55 (6H, m). δC (126 MHz; CD$_3$OD) 166.39, 158.57, 156.42, 151.95, 137.64, 136.92, 135.87, 127.40, 124.34, 110.85, 74.17, 44.63, 43.71, 41.63, 38.50, 29.18. ESI-MS m/z 267.2377 (M$^+$, 12%), 362.1364 (M^{2+}, 16), 406.2014 (M^{2+}, 72).

2.2.2.2.4 Nickel Complex.

The nickel complex was synthesized as described above with the following amounts: **2** (0.25 g, 0.7 mmol), nickel(II) chloride hexahydrate (0.084 g, 0.35 mmol), DCM (2.5 mL) and methanol (2.5 mL), resulting in a tan powder in quantitative yield that was used without further purification. IR v_{max}/cm^{-1} 2963, 1600, 1558, 1472, 1437, 1365, 1220, 1159, 1054, 1033, 1014, 1002, 859, 793. ESI-MS m/z 340.1472 (M^{2+}, 26%), 384.2060 (M^{2+}, 62), 803.3941 (M^{2+} + Cl$^-$, 12).

2.2.2.2.5 Cobalt Complex.

The cobalt complex was synthesized as described above with the following amounts: **2** (0.25 g, 0.7 mmol), cobalt(II) chloride hexahydrate (0.084 g, 0.35 mmol), DCM (2.5 mL) and methanol (2.5 mL), resulting in a deep red/brown powder in quantitative yield that was used without further purification. IR v_{max}/cm^{-1} 3303, 2961, 1600, 1554, 1472, 1438, 1364,

1254, 1219, 1159, 1054, 1029, 1000, 859, 792. ESI-MS m/z 340.6440 (M^{2+}, 34%), 384.7001 (M^{2+}, 49), 716.2576 ($M^+ + Cl^-$, 4) 804.3863 ($M^+ + Cl^-$, 13).

2.2.2.2.6 Iron Complex.

The iron complex monomer was synthesized as described above with the following amounts: norbornene terpyridine ligand (0.4 g, 1.13 mmol), iron (II) chloride tetrahydrate (0.112 g, 0.56 mmol), DCM (5 mL) and methanol (5 mL) resulting in a deep purple powder in quantitative yield that was used without further purification. ^{1}H NMR (MeOD, ppm, 500 MHz): 8.66 (4H, s), 8.58 (4H, d), 7.83 (4H, t), 7.17 (4H, br), 7.08 (4H, br), 6.17 (4H, m), 4.65 (2H, t), 4.52 (2H, t), 3.01 (2H, br), 2.91 (2H, br), 2.10 (2H, br), 1.56 (2H, m), 1.45 (6H, m). ^{13}C NMR (MeOD, ppm, 500 MHz): 168.40, 160.86, 158.37, 152.89, 138.40, 136.96, 135.90, 127.17, 123.60, 111.29, 74.52, 44.68, 43.76, 41.66, 38.53, 29.30. ESI-MS m/z 383.1944 (M^{2+}, calculated 383.14)

2.2.2.2.7 Manganese Complex.

The manganese complex monomer was synthesized as described above with the following amounts: norbornene terpyridine ligand (0.4 g, 1.13 mmol), manganese (II) chloride (0.071 g, 0.56 mmol), ethanol (10 mL) resulting in a tan powder in quantitative yield that was used without further purification. ESI-MS m/z 382.6985 (M^{2+}, calculated 382.64).

2.2.2.2.8 Zinc Complex.

The zinc complex monomer was synthesized as described above with the following amounts: norbornene terpyridine ligand (0.35 g, 0.98 mmol), zinc (II) chloride (0.067 g, 0.49 mmol), DCM (5 mL) and methanol (5 mL) resulting in a light brown powder in quantitative yield that was used without further purification. ^{1}H NMR (MeOD, ppm, 500 MHz):8.67 (4H, d), 8.37 (4H, s), 8.08 (4H, m), 7.76 (4H, br), 7.36 (4H, t), 6.13 (4H, m),

4.57 (2H, m), 4.42 (2H, m), 2.93 (2H, br), 2.88 (2H, br), 2.01 (2H, m), 1.50 (2H, m), 1.40 (6H, m). ^{13}C NMR (MeOD, ppm, 500 MHz): 171.86, 151.04, 148.13, 147.30, 141.08, 136.94, 135.81, 74.48, 44.59, 43.65, 41.61, 38.40, 29.12. ESI-MS m/z 387.1948 (M^{2+}, calculated 387.14).

2.2.2.2.9 Norbornene-functionalized PEO (with ester linkages).

The PEO, 4,000 g/mol, was functionalized with norbornene end groups using the Mitsunobu reaction as previously reported in literature.[127,12811,59,60,63] Dihydroxy PEO (1 eq.) was dried overnight in a vacuum oven at 60 °C and dissolved in a septum-sealed flask with DCM, magnetic stir bar, exo-5-norbornenecarboylic acid (6 eq.), and triphenyl phosphine (6 eq.) under nitrogen and placed in an ice bath. Diisopropyl azodicarboxylate (6 eq.) was diluted in dry DCM under nitrogen, added dropwise to the reaction, and stirred overnight. After the reaction was complete, the functionalized PEO was purified via precipitation into diethyl ether followed by vacuum filtration resulting in a white powder (80% yield) with 95% norbornene functionalization. Molecular characterization matched what has been previously reported for this molecule.[127,128]

2.2.2.2.10 Norbornene Functionalized PEO (with ether linkages).

Tosylated 5-norbornene-2-methanol (norbornene tosyl) was synthesized and used as reported above.[81] Sodium hydride (0.2 g, 8.3 mmol) was added to a 50 mL round bottom flask with a stir bar. The flask was then covered with a septum and purged with N$_2$ gas. PEO (4 kg/mol, 1 g, 0.25 mmol) was dissolved in DMF (8 mL) and added via syringe to the flask, which was kept under positive N$_2$ pressure. The solution was stirred at 80 °C for 30 minutes. Norbornene tosyl (0.36 g, 1.25 mmol) was then dissolved in DMF (2 mL) and added to the flask via syringe. The solution was then stirred at 80 °C overnight. In the

morning, the flask was cooled to room temperature, after which the remaining sodium hydride was slowly quenched with methanol until bubbling stopped. The solution was then diluted with diethyl ether (50 mL) and placed in a -20 ˚C freezer to allow the PEO to precipitate overnight. In the morning the solution was filtered, after which the resulting powder was dissolved in minimum DCM, filtered and then precipitated into diethyl ether. After precipitating overnight in a -20 ˚C freezer, the product was filtered and dried under vacuum for 24 hours resulting in a white powder product (0.94 g, 94% yield).

2.2.2.3 AEM Synthesis

2.2.2.3.1 Synthesis with no PEO crosslinker.

2.2.2.3.1.1 Membrane Preparation.

All AEMs were synthesized following an adaption of a previously reported procedure.[59] The required monomer, dicyclopentadiene, and norbornene, were dissolved in a methanol/chloroform mixture. A solution of Grubb's 2nd generation catalyst (G2) in chloroform was added and the solution was stirred vigorously for up to one minute. The solution was transferred to a pre-heated (40 °C) aluminum pan (diameter of ~7 cm and depth of ~1.5 cm) on a hot plate set to 40 °C. The pan was then covered by a glass jar (diameter of ~7.5 cm and depth of ~9 cm) to slow down evaporation of the solvent. After one hour, the cover was removed and the temperature remained at 40 °C. After another hour, the temperature was raised to 70°C. The membrane was then cooled and transferred to a glass jar. It was then swelled in 100% methanol, followed by 70% aqueous methanol, and then 30% aqueous methanol for at least 6 hours each. Finally the membrane was swelled in 100% RO water for at least 12 hours and the resulting membrane was stored in fresh RO water at all time unless otherwise stated.

2.2.2.3.1.2 $^{0.17}$Ru.

The resulting deep red, translucent membrane was generated with the following amounts: the ruthenium monomer (0.15 g, 0.15 mmol), norbornene (0.0135 g, 0.14 mmol) and dicyclopentadiene (0.078 mL, 0.58 mmol) were dissolved in a chloroform/methanol co-solvent (2.03 mL/0.225 mL, respectively). G2 (2.9 mg, 0.0034 mmol) was dissolved in chloroform (0.225 mL). The resulting deep red, translucent membrane was generated as stated above. The associated N-ethylmorpholinium chloride byproduct associated with ruthenium complexes is not shown since its presence is well documented and its thorough removal was performed as described previously.[11,59]

2.2.2.3.1.3 $^{0.33}$Ru.

The resulting deep red, translucent membrane was generated with the following amounts: the ruthenium monomer (0.05 g, 0.048 mmol), norbornene (2.3 mg, 0.024 mmol), and dicyclopentadiene (0.0098 mL, 0.073 mmol) were dissolved in a chloroform/methanol co-solvent (0.6 mL/0.25 mL, respectively). G2 (1 mg, 0.001 mmol) was dissolved in chloroform (0.15 mL). The resulting deep red, translucent membrane was generated as stated above. The N-ethylmorpholinium chloride byproduct associated with ruthenium complexes is not shown as its presence is well documented and its thorough removal was performed as described previously.[11,59]

2.2.2.3.1.4 $^{0.5}$Ru.

The resulting deep red, translucent membrane was generated with the following amounts: the ruthenium monomer (0.05 g, 0.048 mmol), norbornene (1.5 mg, 0.016 mmol), and dicyclopentadiene (0.0044 mL, 0.032 mmol) were dissolved in a chloroform/methanol co-solvent (0.6 mL/0.25 mL, respectively). G2 (1 mg, 0.001 mmol) was dissolved in

chloroform (0.15 mL). The resulting deep red, translucent membrane was generated as stated above. The N-ethylmorpholinium chloride byproduct associated with ruthenium complexes is not shown as its presence is well documented and its thorough removal was performed as described previously.[11,59]

2.2.2.3.1.5 $^{0.17}$Ni.

The resulting brown, translucent membrane was generated with the following amounts: the nickel monomer (0.15 g, 0.18 mmol), norbornene (0.0165 g, 0.18 mmol) and dicyclopentadiene (0.096 mL, 0.71 mmol) were dissolved in a chloroform/methanol co-solvent (2.03 mL/0.225 mL, respectively). G2 (2.9 mg, 0.0034 mmol) was dissolved in chloroform (0.225 mL), added to the monomers and stirred vigorously. The resulting brown, translucent membrane was generated as stated above.

2.2.2.3.1.6 $^{0.33}$Ni.

The resulting brown, translucent membrane was generated with the following amounts: the nickel monomer (0.05 g, 0.06 mmol), norbornene (2.8 mg, 0.03 mmol), and dicyclopentadiene (0.12 mL, 0.09 mmol) were dissolved in a chloroform/methanol co-solvent (0.6 mL/0.25 mL, respectively). G2 (1 mg, 0.001 mmol) was dissolved in chloroform (0.15 mL). The resulting brown, translucent membrane was generated as stated above.

2.2.2.3.1.7 $^{0.5}$Ni.

The resulting brown, translucent membrane was generated with the following amounts: the nickel monomer (0.05 g, 0.06 mmol), norbornene (1.9 mg, 0.02 mmol), and dicyclopentadiene (0.0054 mL, 0.04 mmol) were dissolved in a chloroform/methanol co-solvent (0.6 mL/0.25 mL, respectively). G2 (1 mg, 0.001 mmol) was dissolved in

chloroform (0.15 mL). The resulting brown, translucent membrane was generated as stated above.

2.2.2.3.1.8 $^{0.17}$Co.

The resulting red/brown, translucent membrane was generated with the following amounts: the cobalt monomer (0.15 g, 0.18 mmol), norbornene (0.0165 g, 0.18 mmol) and dicyclopentadiene (0.096 mL, 0.71 mmol) were dissolved in a chloroform/methanol co-solvent (2.03 mL/0.225 mL, respectively). G2 (2.9 mg, 0.0034 mmol) was dissolved in chloroform (0.225 mL). The resulting red/brown, translucent membrane was generated as stated above.

2.2.2.3.1.9 $^{0.33}$Co.

The resulting red/brown, translucent membrane was generated with the following amounts: the cobalt monomer (0.05 g, 0.06 mmol), norbornene (2.8 mg, 0.03 mmol), and dicyclopentadiene (0.12 mL, 0.09 mL) were dissolved in a chloroform/methanol co-solvent (0.6 mL/0.25 mL, respectively). G2 (1 mg, 0.001 mmol) was dissolved in chloroform (0.15 mL). The resulting red/brown, translucent membrane was generated as stated above.

2.2.2.3.1.10 $^{0.5}$Co.

The resulting red/brown, translucent membrane was generated with the following amounts: the cobalt monomer (0.05 g, 0.06 mmol), norbornene (1.9 mg, 0.02 mmol), and dicyclopentadiene (0.0054 mL, 0.04 mmol) were dissolved in a chloroform/methanol co-solvent (0.6 mL/0.25 mL, respectively). G2 (1 mg, 0.001 mmol) was dissolved in chloroform (0.15 mL). The resulting red/brown, translucent membrane was generated as stated above.

2.2.2.3.2 AEM Synthesis with PEO crosslinker containing ester linkages.

2.2.2.3.2.1 Membrane Preparation.

In order to keep the crosslink density consistent, the cationic metal complexes were polymerized in the presence of norbornene, dicyclopentadiene (DCPD), and the hydrophilic PEO.[11,59,60,127,128] The metal-containing monomer, dicyclopentadiene, norbornene, and telechelic PEO were dissolved in a methanol/chloroform mixture. A solution of Grubb's 2nd generation catalyst (G2) in chloroform was added and the solution was stirred vigorously for up to one minute. The solution was transferred to a pre-heated (40 °C) aluminum pan (diameter of ~7 cm and depth of ~1.5 cm) on a hot plate set to 40 °C. The pan was then covered with a glass jar (diameter of ~7.5 cm and depth of ~9 cm) to slow evaporation of the solvent. After one hour at 40 °C, the cover was removed and the temperature remained at 40 °C for another hour, after which the temperature was raised to 70 °C for one more hour. The membrane was then cooled and transferred to a glass jar where it was swollen in 100% methanol, followed by 70% aqueous methanol, and then 30% aqueous methanol for at least 6 hours for each solution. Finally, the membrane was swelled in 100% RO water for at least 12 hours and the resulting membrane was stored in fresh RO water until characterization unless otherwise stated.

2.2.2.3.2.2 $^{0.36}$Ru$_{PEOes}$.

The resulting deep red, translucent membrane was generated with the following amounts: the ruthenium monomer (0.1 g, 0.096 mmol), norbornene (9 mg, 0.096 mmol), dicyclopentadiene (0.0098 mL, 0.048 mmol), and PEO (0.097 g, 0.024 mmol) were dissolved in a chloroform/methanol co-solvent (1.2 mL/0.5 mL, respectively). G2 (2 mg, 0.002 mmol) was dissolved in chloroform (0.3 mL). The resulting deep red, translucent

membrane was generated as stated above. The N-ethylmorpholinium chloride byproduct associated with ruthenium complexes is not shown as its presence is well documented and its thorough removal was performed as described previously.[11,59]

2.2.2.3.2.3 [0.55]Ru[PEOes].

The resulting deep red, translucent membrane was generated with the following amounts: the ruthenium monomer (0.1 g, 0.096 mmol), norbornene (6.1 mg, 0.065 mmol), and PEO (0.0645 g, 0.016 mmol) were dissolved in a chloroform/methanol co-solvent (1.2 mL/0.5 mL, respectively). G2 (2 mg, 0.002 mmol) was dissolved in chloroform (0.3 mL). The resulting deep red, translucent membrane was generated as stated above. The N-ethylmorpholinium chloride byproduct associated with ruthenium complexes is not shown as its presence is well documented and its thorough removal was performed as described previously.[11,59]

2.2.2.3.2.4 [0.36]Ni[PEOes].

The resulting brown, translucent membrane was generated with the following amounts: the nickel monomer (0.1 g, 0.12 mmol), norbornene (11 mg, 0.12 mmol), dicyclopentadiene (0.008 mL, 0.06 mmol), and PEO (0.119 g, 0.03 mmol) were dissolved in a chloroform/methanol co-solvent (1.2 mL/0.5 mL, respectively). G2 (2 mg, 0.002 mmol) was dissolved in chloroform (0.3 mL). The resulting brown, translucent membrane was generated as stated above.

2.2.2.3.2.5 [0.55]Ni[PEOes].

The resulting brown, translucent membrane was generated with the following amounts: the nickel monomer (0.1 g, 0.12 mmol), norbornene (7.5 mg, 0.08 mmol), and PEO (0.079 g, 0.02 mmol) were dissolved in a chloroform/methanol co-solvent (1.2 mL/0.5 mL,

respectively). G2 (2 mg, 0.002 mmol) was dissolved in chloroform (0.3 mL). The resulting brown, translucent membrane was generated as stated above.

2.2.2.3.2.6 $^{0.36}CO_{PEOes}$.

The resulting red/brown, translucent membrane was with the following amounts: the cobalt monomer (0.1 g, 0.12 mmol), norbornene (11 mg, 0.12 mmol), dicyclopentadiene (0.008 mL, 0.06 mmol), and PEO (0.119 g, 0.03 mmol were dissolved in a chloroform/methanol co-solvent (1.2 mL/0.5 mL, respectively). G2 (2 mg, 0.002 mmol) was dissolved in chloroform (0.3 mL). The resulting red/brown, translucent membrane was generated as stated above.

2.2.2.3.2.7 $^{0.55}CO_{PEOes}$.

The resulting red/brown, translucent membrane was generated with the following amounts: the cobalt monomer (0.1 g, 0.12 mmol), norbornene (7.5 mg, 0.08 mmol), and PEO (0.079 g, 0.02 mmol) were dissolved in a chloroform/methanol co-solvent (1.2 mL/0.5 mL, respectively). G2 (2 mg, 0.002 mmol) was dissolved in chloroform (0.3 mL). The resulting red/brown, translucent membrane was generated as stated above.

2.2.2.3.3 AEM Synthesis with PEO crosslinker containing ether linkages.

2.2.2.3.3.1 Membrane Preparation.

In order to keep the crosslink density consistent, the cationic metal complexes were polymerized in the presence of norbornene, dicyclopentadiene (DCPD), and the hydrophilic PEO.[11,59,60,127,12811,59,60,63] The metal-containing monomer, dicyclopentadiene, norbornene, and telechelic PEO were dissolved in a methanol/chloroform mixture. A solution of Grubb's 2nd generation catalyst (G2) in chloroform was added and the solution was stirred vigorously for up to one minute. The solution was transferred to a pre-heated

(40 °C) aluminum pan (diameter of ~7 cm and depth of ~1.5 cm) on a hot plate set to 40

°C. The pan was then covered with a glass jar (diameter of ~7.5 cm and depth of ~9 cm) to

slow evaporation of the solvent. After one hour at 40 °C, the cover was removed and the

temperature remained at 40 °C for another hour, after which the temperature was raised to

70 °C for one more hour. The membrane was then cooled and transferred to a glass jar

where it was swollen in 100% methanol, followed by 70% aqueous methanol, and then

30% aqueous methanol for at least 6 hours for each solution. Finally, the membrane was

swelled in 100% RO water for at least 12 hours and the resulting membrane was stored in

fresh RO water until characterization unless otherwise stated.

2.2.2.3.3.2 $^{0.55}$Ru$_{PEOet}$.

The resulting red, translucent membrane was generated by the following: the ruthenium

monomer (0.15 g, 0.12 mmol), norbornene (11.25 mg, 0.12 mmol), norbornene

functionalized PEO (0.12 g, 0.03 mmol) were dissolved in a chloroform/methanol co-

solvent (1.8 mL/0.75 mL, respectively). G2 (3 mg, 0.003 mmol) was dissolved in

chloroform (0.45 mL). The resulting deep red, translucent membrane was generated as

stated above. The N-ethylmorpholinium chloride byproduct associated with ruthenium

complexes is not shown as its presence is well documented and its thorough removal was

performed as described previously.[11,59]

2.2.2.3.3.3 $^{0.55}$Ni$_{PEOet}$.

The resulting brown, translucent membrane was generated by the following: the nickel

monomer (0.15 g, 0.18 mmol), norbornene (11.25 mg, 0.12 mmol), norbornene

functionalized PEO (0.12 g, 0.03 mmol) were dissolved in a chloroform/methanol co-

solvent (1.8 mL/0.75 mL, respectively). G2 (3 mg, 0.003 mmol) was dissolved in

chloroform (0.45 mL). The resulting brown, translucent membrane was generated as stated above.

2.2.2.3.3.4 $^{0.55}Co_{PEOet}$.

The resulting red/brown, translucent membrane was generated by the following: the cobalt monomer (0.15 g, 0.18 mmol), norbornene (11.25 mg, 0.12 mmol), norbornene functionalized PEO (0.12 g, 0.03 mmol) were dissolved in a chloroform/methanol co-solvent (1.8 mL/0.75 mL, respectively). G2 (3 mg, 0.003 mmol) was dissolved in chloroform (0.45 mL). The resulting red/brown, translucent membrane was generated as stated above.

2.2.2.3.3.5 $^{0.55}Fe_{PEOet}$.

The resulting purple, translucent membrane was generated by the following: the iron monomer (0.15 g, 0.19 mmol), norbornene (11.25 mg, 0.12 mmol), norbornene functionalized PEO (0.12 g, 0.03 mmol) were dissolved in a chloroform/methanol co-solvent (1.8 mL/0.75 mL, respectively). G2 (3 mg, 0.003 mmol) was dissolved in chloroform (0.45 mL). The resulting purple, translucent membrane was generated as stated above.

2.2.2.3.3.6 $^{0.55}Mn_{PEOet}$.

The resulting tan, translucent membrane was generated by the following: the manganese monomer (0.15 g, 0.20 mmol), norbornene (11.25 mg, 0.12 mmol), norbornene functionalized PEO (0.12 g, 0.03 mmol) were dissolved in a chloroform/methanol co-solvent (1.8 mL/0.75 mL, respectively). G2 (3 mg, 0.003 mmol) was dissolved in chloroform (0.45 mL). The resulting tan, translucent membrane was generated as stated above.

2.2.2.3.3.7 $^{0.55}$Zn$_{PEOet}$.

The resulting tan, translucent membrane was generated by the following: the zinc monomer (0.15 g, 0.19 mmol), norbornene (11.25 mg, 0.12 mmol), norbornene functionalized PEO (0.12 g, 0.03 mmol) were dissolved in a chloroform/methanol co-solvent (1.8 mL/0.75 mL, respectively). G2 (3 mg, 0.003 mmol) was dissolved in chloroform (0.45 mL). The resulting tan, translucent membrane was generated as stated above.

2.2.3 Determination of Ion Exchange Capacity

2.2.3.1 Acid-Base Titration.

To calculate membrane IEC values for the non-PEO containing samples, membranes in the OH⁻ form were immersed in 10 mL of a 0.01 M HCl solution for 24 hours with stirring. The solutions were then back titrated, with stirring, using a 0.01 M KOH solution to pH = 7. The membranes were washed and immersed with DI water for 24 hours to remove residual salts, after which they were dried under vacuum at 50 °C for 24 hours and weighed for their dried mass. This titration was also performed on blank samples containing no membrane, as a control. The IEC was calculated using equation 7:

$$IEC = \frac{(V_c - V_s)c_{KOH}*1000}{m_s} \tag{7}$$

where V_c is the volume of the KOH solution used for the control sample, V_s is the volume of the KOH solution used for the sample, c_{KOH} is the concentration of the KOH solution and m_s is the dried mass of the sample.

2.2.3.2 Mohr's Titration.

To calculate the ion-exchange capacity (IEC), the membranes were first ion-exchanged to the chloride form by immersing it in a 1 M NaCl solution for 24 hours. The sample was

then thoroughly rinsed with deionized water to remove any excess chloride ion.

Following this, the samples were immersed in a 0.5 M aqueous solution of sodium

sulfate. This process leached out the chloride ions making them available for reaction.

The resulting solution was titrated using a 0.1 M silver nitrate solution in the presence of

a few drops of potassium chromate (0.25 M) as indicator. The IEC (mmol/g) of the

membrane was calculated from the amount of silver nitrate consumed (mmol) during the

titration and the mass of the dry membrane.

2.2.4 AEM Gel Fraction.

The gel fraction was determined as follows. The AEM was synthesized as described

previously, but instead of the standard work-up, they were instead placed in methanol and

heated at 70°C overnight. The samples were then dried in vacuum at 50°C and weighed.

2.3 Results and Discussion

2.3.1 Thiol-Ene-Based AEMs

2.3.1.1 Synthesis of Monomers and Macromonomers

To incorporate metal cations into a thiol-ene-style synthetic platform, a di-

norbornene functionalized terpyridine ligand monomer, **3**, was synthesized in four steps,

as shown in Figure 10A. The thiol-ene reaction was chosen due to its fast reaction times,

high conversions, ambient reaction conditions, and high functional group tolerance.[129–136]

To demonstrate monomer **3**'s ability to participate in the thiol-ene step-growth

polymerization, homopolymer **P3** was synthesized by reacting **3** and a dithiol in NMP with

a photoinitiator (Figure 10B). After irradiating for an hour under UV light, ^{1}H NMR

confirmed complete conversion of the double bond peak into the desired polymer and THF

gel permeation chromatography (GPC) was used to confirm polymer formation (Figures

11 and 12). This polymerization further demonstrated the versatility and functional group tolerance of the thiol-ene reaction, as it was able to polymerize despite the presence of the terpyridine group. Using **3** also allows for the facile incorporation of metal complexes into thiol-ene style linear polymers and networks, opening the door for further use of these types of functional groups in polymer applications.
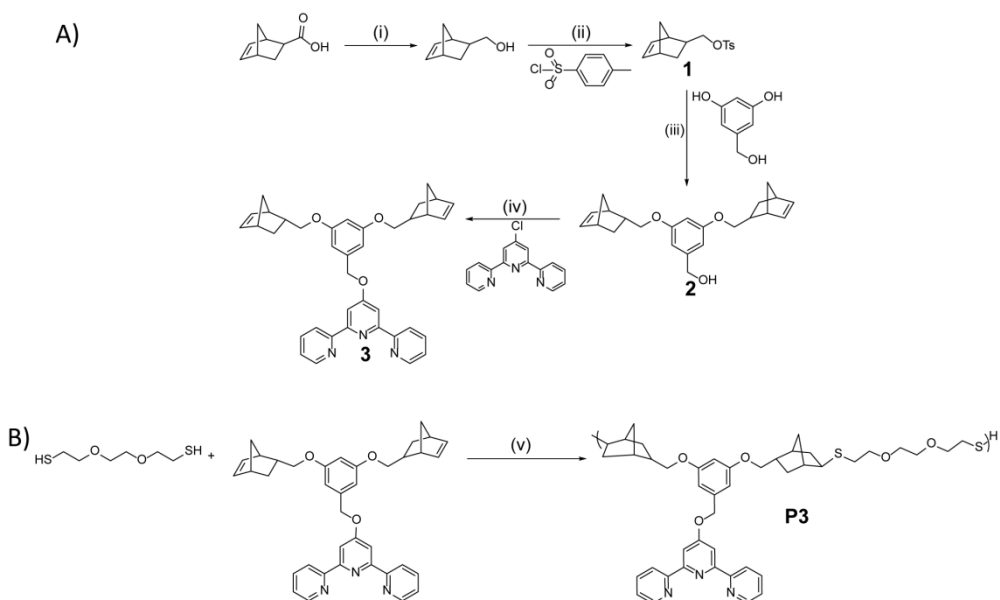
Figure 10. Synthetic procedure for A) monomer 3: (i) THF, LiAlH$_4$, 0 °C-r.t., overnight; (ii) THF, TEA, DMAP, 0 °C-r.t., overnight; (iii) DMF, Cs$_2$CO$_3$, 80 °C, overnight; (iv) DMSO, KOH, 60 °C, 6 hours, and B) polymerization of monomer **3** via the thiol-ene reaction yielding polymer **P3**: (v) CHCl3, Irgacure 2959, UV (365 nm) 1 hr.
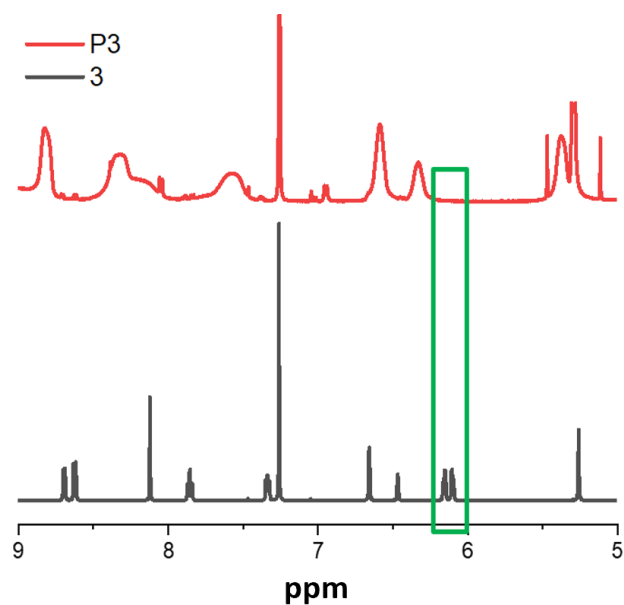
Figure 11. ^{1}H NMR in CDCl$_3$ for monomer **3** and homopolymer **P3,** showing complete disappearance of the norbornene double bond peaks highlighted with a green box.
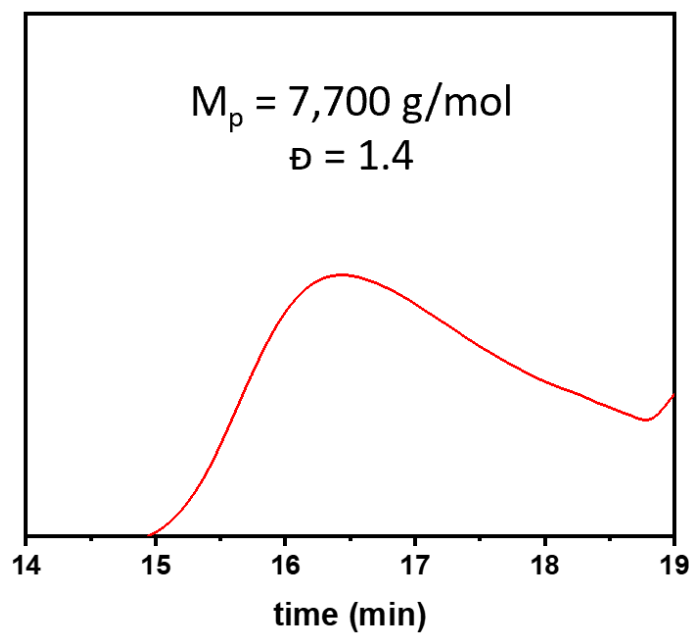
Figure 12. GPC trace with THF as an eluent for **P3** with molecular weight and dispersity showed as an inset.

Once **3** was synthesized, a second polymer was chosen that would phase separate

from **P3** in a crosslinked network. A norbornene functionalized, polystyrene (PS)-based

polymer was selected due to its chemical stability and the expectation that having the hydrophobic PS in conjunction with the nickel cation polymer would result in a phase-separated network. To accomplish this goal, monomer **4** was synthesized from 4-vinylbenzyl chloride, following an adaptation from published literature,[33] and then copolymerized with styrene using reverse addition-fragmentation chain transfer (RAFT) polymerization to produce the copolymer **CP4** (Figure 13). This polymer was then characterized using ^{1}H NMR and gel permeation chromatography (GPC). From the ^{1}H NMR it was determined that **CP4** was 23 % by weight monomer **4** (Figure 14), and the molecular weight from GPC was 6,700 g/mol with a dispersity of 1.1 (Figure 15 and Table 2), which correlated to roughly 6 repeat units of **4** and 50 repeat units of styrene per polymer chain. That meant that **CP4** would act as a multi-functional, alkaline stable, macromonomer crosslinker in the thiol-ene reaction, with a degree of functionality (f_n) of six. Furthermore, since it was synthesized by the copolymerization of **4** and styrene, the f_n can be easily controlled simply by modulating the ratio of the two monomers, adding better tunability to the resulting network. As a way to demonstrate this tunability, **4** was also homopolymerized using RAFT to produce the crosslinker **HP4**, a polymer where every repeat unit contains a norbornene functional group. From the GPC trace it was determined that **HP4** had a molecular weight of 8,200 g/mol with a dispersity of 1.75, which correlated to an average degree of polymerization, or in this case a f_n, of 34 (Figure 16 and Table 2). While **4** does not homopolymerize in a controlled, living manner, it demonstrated the ease with which a wide range of f_n can be obtained.
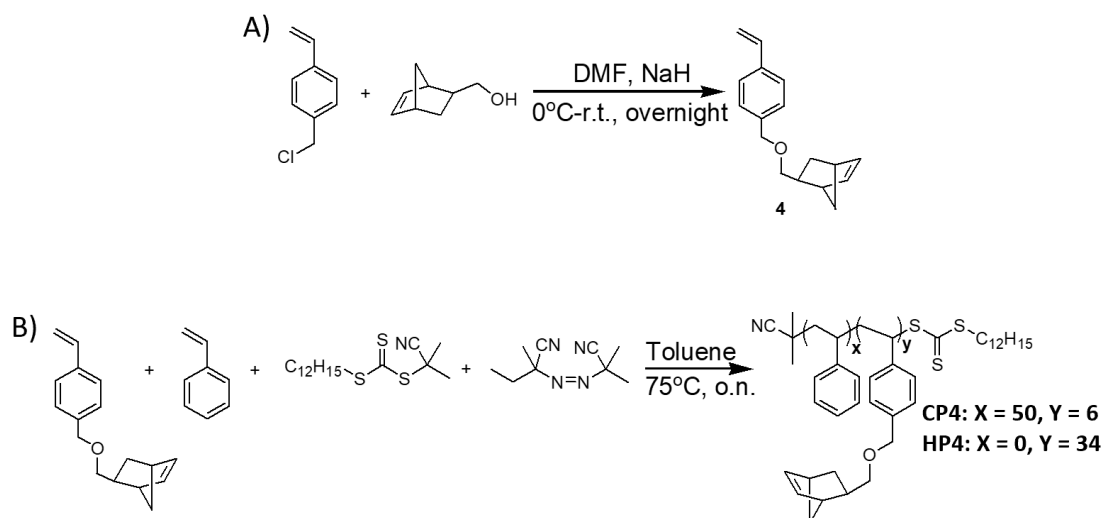
Figure 13. Synthetic procedure for A) monomer **4** and B) polymerization via RAFT for copolymer **CP4** (X=6, Y=50) or homopolymer **HP4** (X=0, Y=34).
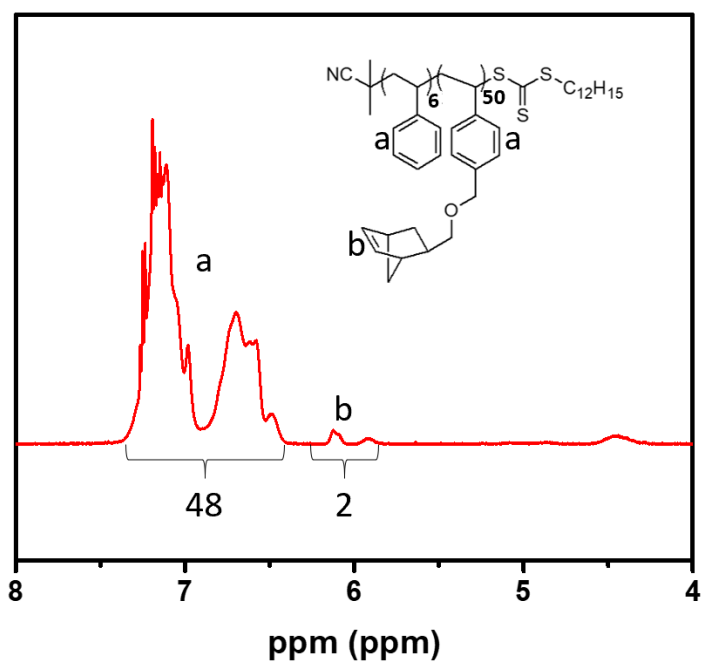
Figure 14. ^{1}H NMR spectra of **CP4** showing the integration of the norbornene peak, labeled 'b', and the benzene ring peak, labeled 'a', corresponding to an incorporation of **4** in **CP4** to be 23 wt%.
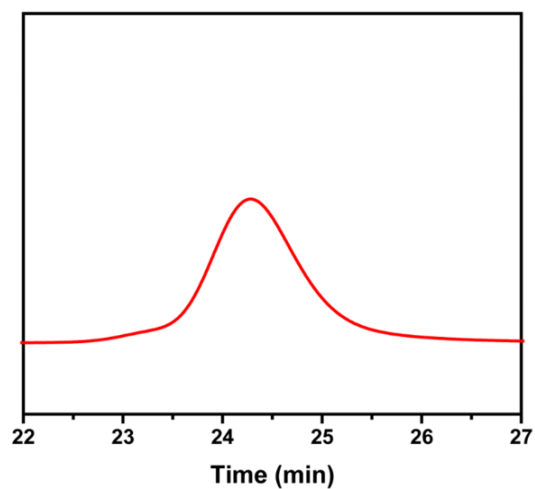
Figure 15. GPC trace with THF as an eluent for **CP4.**
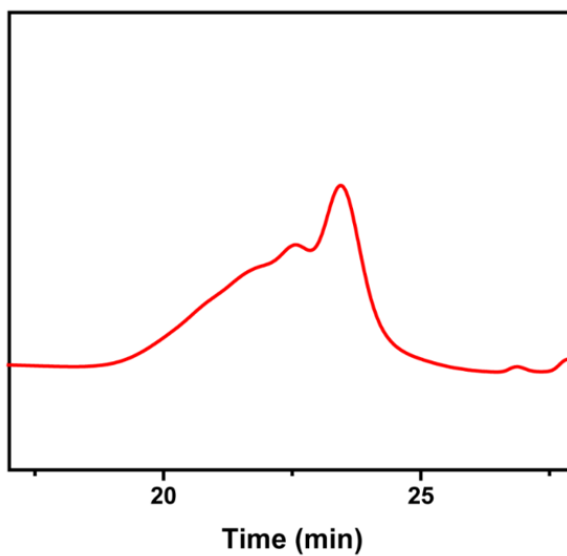
Figure 16. GPC trace with THF as an eluent for **HP4.**

Table 2. Summary of molecular weights and dispersity for **CP4** and **HP4**.

Sample	M_p	M_n	M_w	D
CP4	6,700	6,000	6,800	1.11
HP4	8,200	12,200	21,400	1.75

2.3.1.2 Synthesis of AEMs

The final step was to then synthesize the AEMs. This was accomplished by dissolving **3**, a dithiol, either **CP4** or **HP4**, photoinitiator, and nickel(II) chloride in NMP and irradiating the solution with UV light for an hour (Figure 17). Nickel was chosen for two reasons: 1) it has been shown to produce membranes with enhanced conductivity but comparable chemical stability to membranes containing the previously used ruthenium-cations,[11,59,60] and 2) synthesizing nickel-terpyridine complexes can be accomplished more easily than ruthenium complexes.[11,59,60,137] Upon mixing, monomer **3** coordinated with nickel(II) chloride, resulting in a homoleptic, bis(terpyridine) complex crosslinker with four norbornenes. Once the membrane was formed, it was transitioned from NMP to liquid water by soaking for two days in water.

Six different AEMs were fabricated, three with **CP4** and three with **HP4** as the crosslinker, where the amount of **3** added was modified so each membrane contained on average either 5, 10, or 20 repeat units of **3**, correlating to 5, 10, or 20 repeat units of nickel cations, between two PS crosslinkers. However, despite increasing the metal content, all three samples had IEC values around 1 mmol/g, as determined by an acid-base titration (Table 3).[7,117] Full nomenclature and components of each membrane can be seen in Figure 17, where the first part of the name indicates which PS crosslinker was used and the number indicates the average repeat units of **3**. The presence or absence of "Ni" indicates whether the membrane contains nickel or not. In other words, the sample **CP4-5Ni** was synthesized using the PS crosslinker **CP4**, where there should be on average 5 repeat units of **3** between two PS crosslinkers and it contains nickel. **CP4-5** on the other hand, is the same exact membrane as **CP4-5Ni**, except it does not contain nickel cations.

Table 3. Membrane IEC values for the **CP4**-based AEMs.

Sample	IEC$_{exp}$ (mmol/g)
CP4-5Ni	0.98 ± 0.09
CP4-10Ni	1.07 ± 0.07
CP4-20Ni	1.13 ± 0.20

CP4-5Ni: X = 5, Y = 6, Z = 50
CP4-10Ni: X = 10, Y = 6, Z = 50
CP4-20Ni: X = 20, Y = 6, Z = 50
HP4-5Ni: X = 5, Y = 34, Z = 0
HP4-10Ni: X = 10, Y = 34, Z = 0
HP4-20Ni: X = 20, Y = 34, Z = 0
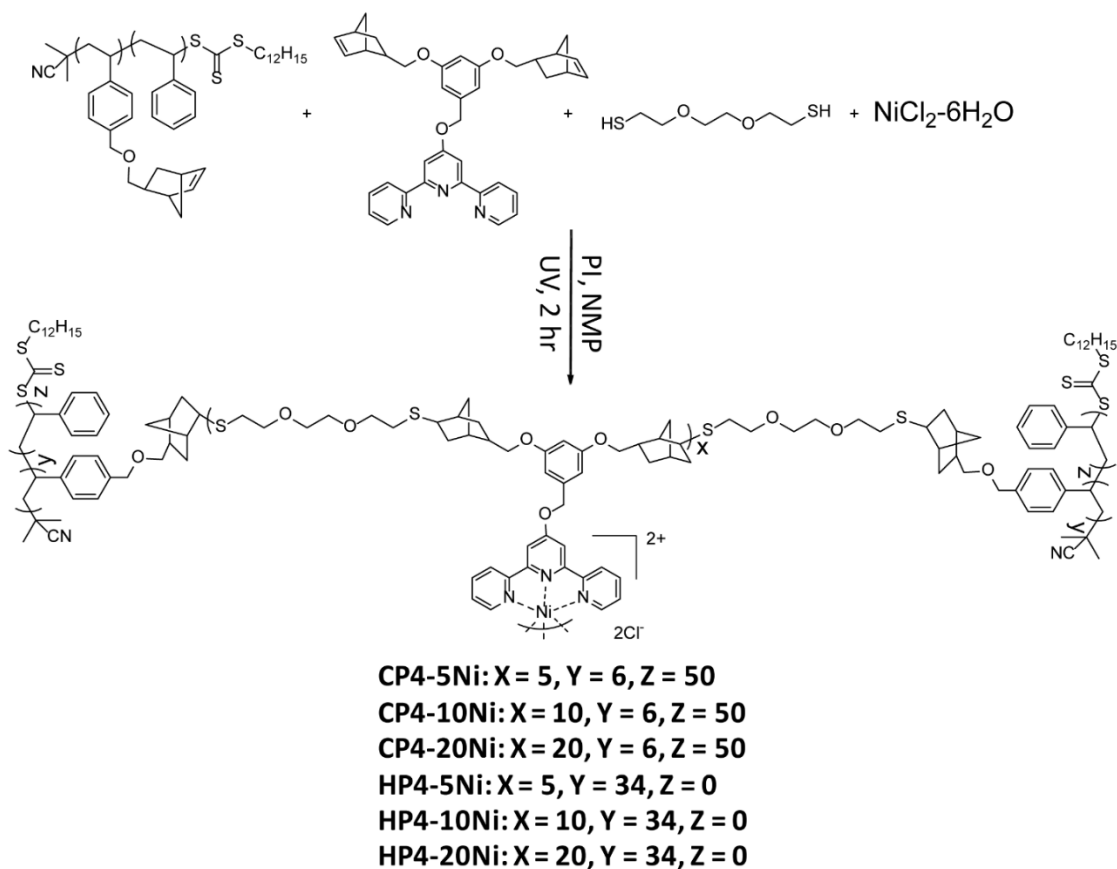
Figure 17. Synthetic scheme for synthesis of AEMs using monomer **3** and **CP4** or **HP4**.

2.3.2 ROMP-Based AEMs

Given the potential that metal cation-, ROMP-based AEMs provided, the previous work was expanded here to include a variety of metal cations including ruthenium, nickel, cobalt, iron, zinc, and manganese. In previous reports, heteroleptic ruthenium complexes were synthesized in order to decouple the crosslinking density from the IEC of the membranes. This was possible due to the stability and slow equilibrium kinetics of the

57

ruthenium-terpyridine bond allowing for a step-wise synthesis of the monomer.[11,59] However, as additional metal cations were synthesized and incorporated into the network, a heteroleptic complex was no longer easily attained, due to the increased metal-terpyridine bond equilibrium kinetics for the other five metals.[137–139] Therefore, the same norbornene-functionalized terpyridine ligand was synthesized as previously reported. In this case, however, two equivalents of the ligand were reacted with the various metal-chloride salts resulting in six homoleptic metal cations in the chloride form (Figure 18).
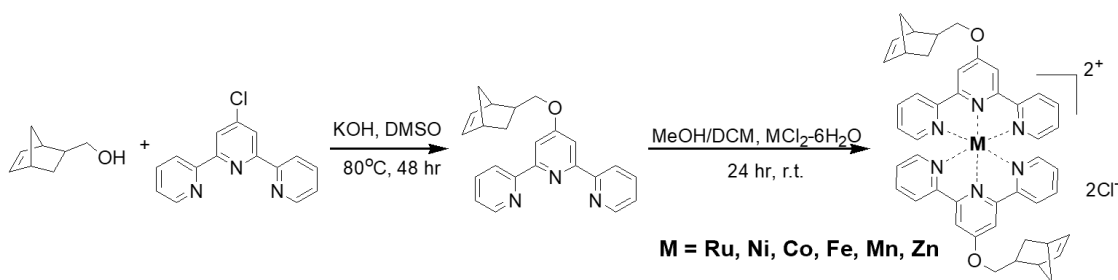
Figure 18. Synthetic scheme for the synthesis of di-norbornene bis(terpyridine) metal complex cations in the chloride form containing ruthenium, nickel, cobalt, iron, manganese, and zinc.

When designing metal cation-containing AEMs, an important factor to consider is the redox potential of the complex. If the metals are active within the operation range of the AEMFC, then potentially detrimental side reactions can occur.[1,140] However, it has been shown that three of the metal-terpyridine complexes (ruthenium, nickel, cobalt) contain redox potentials outside the range for AEMs and should not be active (Table 4).[141–146]

Table 4. Redox potentials for an AEMFC and bis(terpyridine) ruthenium, nickel, and cobalt complexes.

Metal	Redox Potential (V)	Source of redox Potential
AEMFC Electrodes.[1,140, a]	+0.4 +0.83	Reduction of oxygen at cathode Oxidation of hydrogen at anode
Ruthenium[142–144,146, b]	-0.98 to -1.08 -1.41	Oxidation wave Reduction wave
Cobalt[145, b]	+0.26 -0.77	+3/+2 transition +2/+1 transition
Nickel[141, b]	-1.07 -1.36	First wave Second wave

[a]At PH 14. [b]Coordinated to two equivalents of terpyridine.

It was not confirmed that the redox potentials for the other three metal cations (iron, manganese, and zinc) were outside of the range for AEMs, due to the fact that these three metal cations were shown to be instable to high pH conditions. UV-vis spectra for bis(terpyridine) iron, manganese, and zinc complexes in water showed that the cations immediately de-complexed upon the addition of a 2M aqueous KOH solution (Figure 19). Therefore, since these cations are already not stable under alkaline conditions, they are not feasible for the ultimate use in fuel cells and thus their redox potential are not important. However, despite this lack of chemical stability, studying these three cations in addition to ruthenium, nickel, and cobalt, allows for a fuller fundamental understanding of the cation's impact on AEM properties.
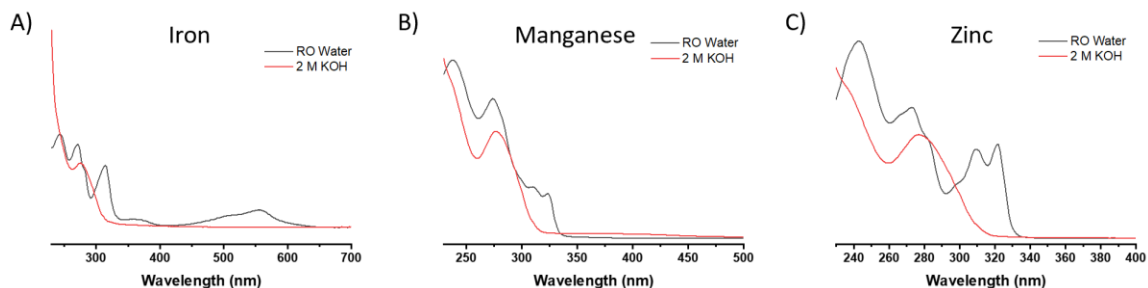
Figure 19. UV-vis spectra for bis(terpyridine) A) iron, B) manganese and C) zinc dissolved in RO water showing the complete loss of the absorption peaks associated with the metal complex upon addition of an aqueous 2 M KOH solution.

These six metal cation monomers where used to synthesize three different types of ROMP-based AEMs: 1) without a PEO crosslinker, 2) with a PEO crosslinker containing ester linkages, and 3) with a PEO crosslinker containing ether linkages (Figure 20). The first type of AEM was initially synthesized to explore the impact of different metal cations on AEM properties using ruthenium, nickel, and cobalt as they were the most stable metal cations. However, due to poor mechanical properties, the second type of AEM was synthesized, where the PEO crosslinker was intended to enhance the mechanical properties. Finally, the third type of AEM was synthesized as a deeper exploration of the influence from a cation's identity was pursued and to demonstrate the ability to incorporate a PEO crosslinker that also had alkaline stability.
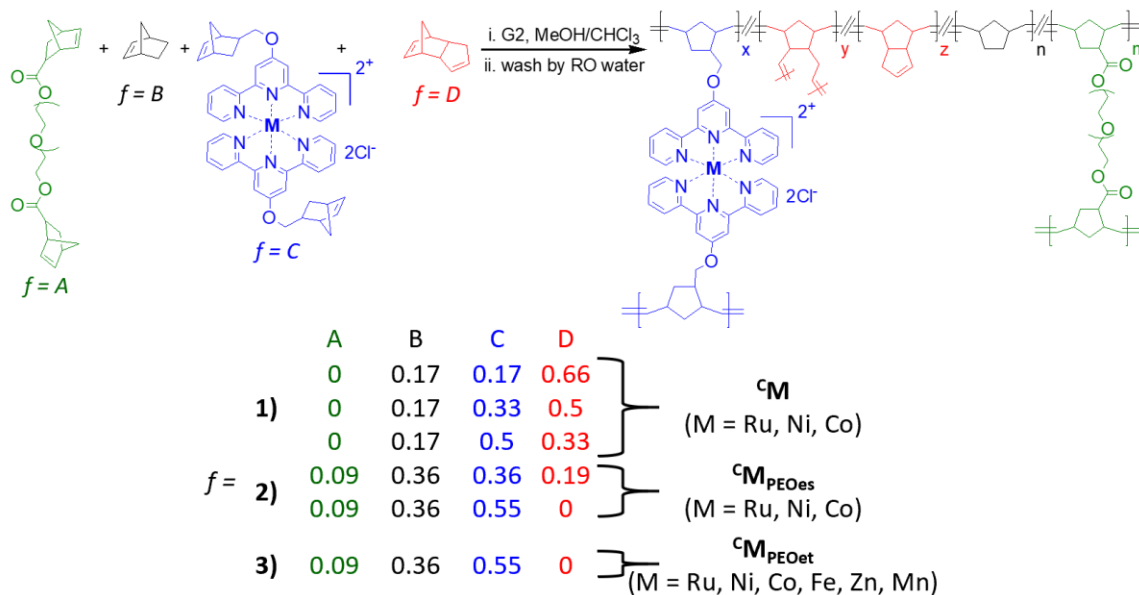
Figure 20. Synthetic scheme for the three different types of ROMP-based AEMs synthesized, where 1) corresponds to the AEMs containing no PEO crosslinker, 2) corresponds to AEMs synthesized with a PEO crosslinker containing ester linkages (shown), and 3) corresponds to AEMs synthesized with a PEO crosslinker containing ether linkages.

The first type of AEMs were synthesized from ruthenium, nickel, and cobalt monomers with DCPD and norbornene using Grubbs second-generation catalyst (G2) in a methanol/chloroform solvent mixture (Figure 20). Nine different AEMs where synthesized, three for each metal, by modifying the monomer mole fraction of DCPD (f = 0.66, 0.5, or 0.33, respectively) and the metal cation monomer (f = 0.17, 0.33, or 0.5, respectively) but keeping the amount of norbornene constant (f = 0.17). The monomer content was altered to ensure that the molar ratio of non-crosslinkers to crosslinkers remained 1:5 while the IEC of the AEMs was modified.

To confirm the incorporation of metal cations into the AEMs, the ion exchange capacity (IEC) was determined experimentally by performing an acid-based titration (Table 5). AEMs in the hydroxide from where reacted with HCl, where the amount of HCl consumed, as determined from the titration, corresponds to the number of hydroxide ions present and thus the number of cations present. This titration confirmed that the incorporation of metal cations was effectively accomplished, and that increasing the number of metal cation monomers incorporated led to the expected increase in IEC. The IEC values confirmed that the faster equilibrium kinetics for the nickel and cobalt complexes did not interfere with the polymerization and did not significantly hinder the number of cations incorporated into the network.

Table 5. IEC values for AEMs synthesized without a PEO crosslinker, determined using an acid-base titration.

Metal	IEC (mmol/g)
[0.17]Ru	0.89 ± 0.51
[0.33]Ru	1.43 ± 0.25
[0.5]Ru	1.81 ± 0.05
[0.17]Ni	0.49 ± 0.11
[0.33]Ni	1.26 ± 0.27
[0.5]Ni	1.65 ± 0.17
[0.17]Co	0.56 ± 0.29
[0.33]Co	0.86 ± 0.43
[0.5]Co	1.39 ± 0.50

To determine the impact of metal-terpyridine equilibrium kinetics on AEM formation, the gel fraction for [0.17]Ru, [0.17]Ni, and [0.17]Co was also determined (Table 6). After AEM formation, the membrane was placed in methanol and incubated at 70 ˚C overnight to remove all the sol fraction. Once dried, it was determined that the nickel- and cobalt-based AEMs had a lower gel fraction (76-79%) than the more stable ruthenium-based AEM (93%). A gel fraction of nearly 80% shows that these more labile metal cations can be used to form networks, just not as effectively as the much slower ruthenium cation, indicating a limitation for using metal cations as crosslinkers in AEMs.

Table 6. Gel fractions for the [0.17]M samples.

Sample	Gel Fraction
[0.17]Ru	93%
[0.17]Ni	79%
[0.17]Co	76%

Due to the poor mechanical properties of the first type of AEM, (discussed in detail in chapter 3), bis(norbornene) metal-terpyridine complexes containing nickel, ruthenium, and cobalt were synthesized and copolymerized *via* ROMP with norbornene, DCPD, and a long, hydrophilic poly(ethylene oxide) (PEO) crosslinker containing ester linkages, to

maintain the same crosslink density (Figure 20).[11,59,60] The di-norbornene functionalized PEO crosslinker (4 kg/mol, Figure 21), synthesized following previously reported procedures, was used to improve the water uptake and mechanical properties of the membranes for handling purposes.[105,127,128] Six AEMs were synthesized: three at a cationic $f = 0.36$ and three with $f = 0.55$ within the network. In order to maintain the same crosslink density between both sets of membranes, the lower metal content samples had DCPD at $f = 0.19$, and the higher metal content samples had no DCPD, with all six membranes having norbornene and the PEO crosslinker at $f = 0.36$ and 0.09, respectively. Full nomenclature for these samples is reported in Figure 20, where the superscript before the element indicates the metal cation monomer f in the network and the "PEOes" subscript denotes the presence of the PEO crosslinker containing ester linkages. The IEC for these samples was not determined experimentally due to the presence of the ester bonds in the PEO which could degrade in the IEC back-titration procedure. However, due to the incorporation determined for the AEMs without the PEO crosslinker, these membranes most likely demonstrated similar metal cation incorporation.
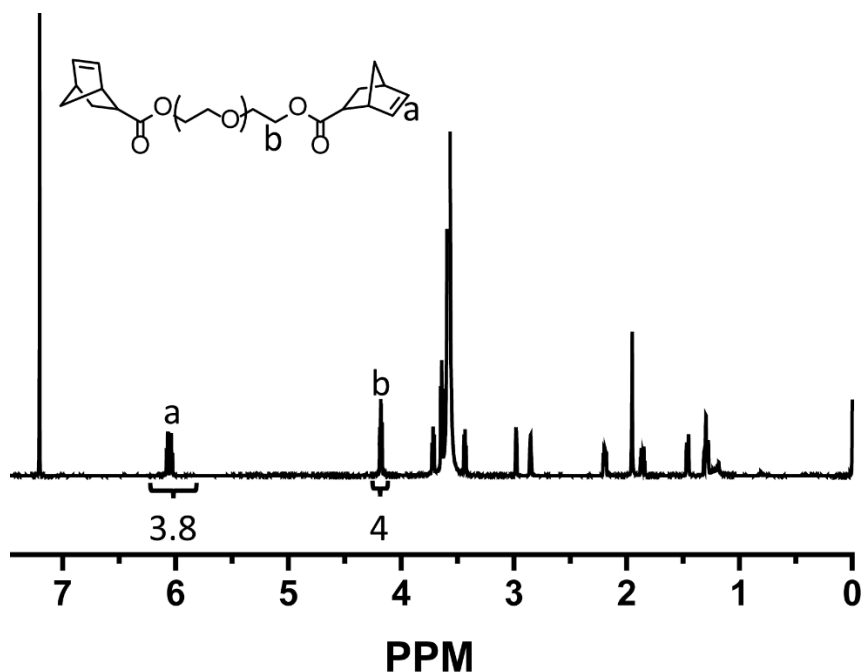
Figure 21. ^{1}H NMR (500 MHz) in CDCl$_3$ of the di-norbornene functionalized PEO containing ester linkages, showing greater than 90 % functionalization.

To further study this class of materials with a wider range of metal cations, the third type of AEM was synthesized from bis(norbornene) metal-terpyridine complexes containing either iron, nickel, ruthenium, zinc, manganese, or cobalt copolymerized with norbornene and a di-norbornene functionalized PEO (4 kg/mol) crosslinker containing ether linkages using ROMP (Figure 20).[11,59,60,63] The PEO crosslinker was synthesized *via* reaction between PEO and a tosylated norbornene and used to enhance water uptake and mechanical properties of the membrane (Figure 22). Functionalization using a tosylated norbornene was performed to demonstrate the ability to enhance mechanical properties using a PEO crosslinker that is also alkaline stable. Six AEMs were synthesized, one for each metal cation used. All membranes were synthesized with a cationic monomer, PEO crosslinker, and norbornene mole fraction (*f*) of 0.55, 0.09, and 0.36, respectively.
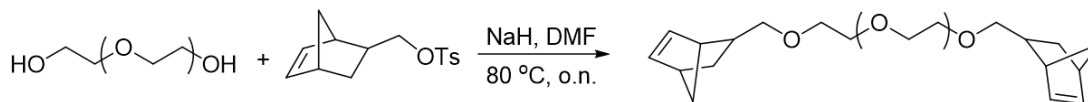
Figure 22. Synthetic scheme for the synthesis of the di-norbornene functionalized PEO containing ether linkages.

Due to the alkaline instability of iron, manganese, and zinc metal complexes, the IEC for these membranes was determined using Mohr's titration (Table 7). This approach utilizes the precipitation of silver chloride from water to determine the number of chloride ions present in the membrane by addition of silver nitrate which forms silver chloride. An indicator that reacts with nitrate was used to determine the exact amount of silver nitrate consumed, which corresponds to the amount of silver chloride that precipitates. All membranes had similar IEC values between 1.58-1.79 mmol/g, except for the zinc-based sample (1.26 mmol/g) and the manganese-based sample (0.68 mmol/g). It is possible that these two cations resulted in lower IEC values because they represent the cations with the fastest metal-terpyridine equilibrium kinetics.[137,147,148] Since the equilibrium kinetics are slowest for ruthenium, similar for nickel, cobalt, and iron, faster for zinc, and fastest for manganese, it is possible that the zinc and manganese complexes represent the limit at which the equilibrium kinetics begin to hinder metal cation incorporation.

Table 7. IEC values for AEMs synthesized with the PEO crosslinker containing ether linkages, determined using Mohr's titration.

Sample	IEC (mmol/g)
$^{0.55}\text{Ru}_{\text{PEOet}}$	1.58
$^{0.55}\text{Ni}_{\text{PEOet}}$	1.79
$^{0.55}\text{Co}_{\text{PEOet}}$	1.68
$^{0.55}\text{Fe}_{\text{PEOet}}$	1.75
$^{0.55}\text{Mn}_{\text{PEOet}}$	0.68
$^{0.55}\text{Zn}_{\text{PEOet}}$	1.26

2.4 Conclusions

Metal cation-based AEMs have shown potential has a promising new class of materials with improved chemical stability and comparable ion conduction as compared to other organic-based AEMs. The reports of ROMP-based, bis(terpyridine) ruthenium-containing AEMs have been expanded here to include two types of metal cation-based AEMs: one synthesized using the thiol-ene reaction and the other synthesized using ROMP. The thiol-ene-based membranes were successfully synthesized by reacting a norbornene-functionalized polystyrene (PS) with a di-norbornene functionalized terpyridine ligand in the presence of nickel chloride and a dithiol. These membranes were designed specifically to incorporate microphase separation into metal cation-based AEMs, as that has not been accomplished previously. This approach demonstrated the range of reactions that can be utilized to synthesize metal cation-based AEMs. However, since the thiol-ene reaction utilizes photoirradiation only certain metal cations can be incorporated into a network synthesized using this reaction. Any metals that absorb light at the same wavelength used for irradiation will render the reaction impossible as no light will reach the photo initiator to initiate the reaction. Therefore, metals such as nickel and zinc can be successfully incorporated, but ruthenium, iron and cobalt cannot be used with the commonly used irradiation wavelength of 365 nm.

In addition to demonstrating the versatility of metal cations with the thiol-ene reaction, the ROMP-based AEMs were also expanded to include a variety of different metal cations and various PEO-based crosslinkers. The AEM formation proved to not be significantly affected by the identity of the metal incorporated into the metal cation. This was shown with six different metals: ruthenium, nickel, cobalt, iron, manganese, and zinc.

While there was a slight decrease in the gel fraction and IEC values as more labile metal-terpyridine complexes were incorporated, all metals were successfully incorporated and crosslinked without noticeable defects. The ability to incorporate long, hydrophilic PEO crosslinkers was also successfully demonstrated. The ability to synthesized alkaline stable PEO crosslinkers was accomplished by incorporating ether linkages as opposed to the more facile to synthesize ester linkages. Overall, this ROMP-based approach proved to be a robust method for synthesizing AEMs.

CHAPTER 3

LIMITATIONS OF USING TYPICAL BULK ANION EXCHANGE MEMBRANE PROPERTIES TO UNDERSTAND ION CONDUCTIVITY

3.1 Introduction

AEM research has primarily focused on the most prominent challenges of current materials: poor membrane ion conductivity, weak mechanical properties, and chemical instability.[1,5,11,28,31,39,82,87,108,149] In order to understand the various AEMs that have been synthesized to solve these challenges, an array of properties are used including water uptake, mechanical properties, chemical stability, ion exchange capacity, and ion conductivity. Understanding these various properties and their impact on AEM performance is crucial, especially for ion conduction.[1,5,24,25,27,36,37,105]

The rich history of AEM research has led to a general understanding of many factors that can impact and explain membrane ion conductivity.[11] The most prominent parameters utilized for explaining ion conductivity in terms of the other bulk membrane properties include: 1) hydration number (λ), 2) fixed ion concentration, 3) activation energy of ion conduction (E_a), 4) ratio of the effective diffusion coefficient for the conducting ion, D, to the dilute solution diffusivity for the ion, D_o (D/D_o), and 5) morphology of the AEM.[11,32,35,54,81,103] The hydration number, which corresponds to the number of water molecules in a swollen membrane per cationic unit, is often used because a larger λ value indicates more water, leading to an expected increase in ion conductivity of the membrane.[116] The ion concentration corresponds to the density of conducting ions within

a swollen network, where more ions per unit volume is assumed to impart higher conductivity.[11] The final three parameters relate to the kinetic mobility of the ions in the AEM and are used to explain conductivity in terms of either a smaller barrier to ion mobility (E_a) or a more ideal movement of the ion in the membrane based on either diffusion (D/D_o) or membrane morphology.[87,150–152] Here, the various metal cation-based AEMs are characterized for these typically studied properties and parameters in the AEM field to elucidate their potential as ion conducting membranes.

3.2 Experimental

3.2.1 Instrumentation

A Blak-Ray 100 W B-110 AP/R lamp was used to irradiate samples for photopolymerization. The ^{1}H and ^{13}C NMR spectra were recorded using a Bruker 500 MHz Ascend NMR Spectrometer retrofitted with a cryo-probe with all J-values given in Hz. Mechanical properties were obtained using dynamic mechanical analysis (DMA) on a TA Instruments DMA Q800. Polymer molecular weights determined in THF were measured using gel permeation chromatography (GPC) on an Agilent 1260 series system equipped with both a refractive index (RI) and an ultraviolet (UV) detector, a PL Gel 5 μm guard column, two 5 μm analytic Mixed-C columns, and a 5 μm analytical Mixed-D column. All columns were connected in series and incubated at 40 °C with THF as an eluent at a flow rate of 1.0 mL/min with toluene as the flow marker. GPC data in DMF (with 0.1 M LiCl) were obtained on an Agilent Technologies 1260 Infinity, fitted with a Gel 5 µm guard column, a PL Gel 5 µm mix D 1° column, and a PL Gel 5 µm Mix C 1° column. All columns were incubated at 50 °C in a mobile phase of DMF with 0.1 M LiCl at a flow rate of 1 mL/min, using toluene as the flow marker. FTIR was performed using a PerkinElmer

Spectrum 100 FTIR spectrometer with a Universal ATR sampling accessory. Mass spectroscopy was recorded using a Bruker MicrOTOF ESI-TOF Mass Spectrometer at the University of Massachusetts, Mass Spectroscopy Facility. Small-angle X-ray scattering (SAXS) was performed on an Osmic MaxFlux Cu Kα X-ray source with a wavelength of 1.54 Å and a 2-dimensional, gas-filled wire array detector (both from Molecular Metrology, Inc.) at a distance of 1.476 m from the sample. The membrane impedance in liquid water was obtained using an impedance/gain phase analyzer (Solartron 1260A, Solartron Analytical, Farnborough Hampshire, ONR, UK). The membrane impedance in 95% relative humidity was obtained using a custom system that multiplexes the impedance analyzer to temperature-calibrated positions within an ESPEC SH-241 bench-top type temperature and humidity chamber

3.2.2 Monomer Water Solubility.

Norbornene-functionalized monomer's water solubility was determined using UV-vis spectroscopy. The metal cation monomers were first dissolved in methanol at five different concentration ranging from 0.006 mM to 0.096 mM. Each solution was then characterized for its UV-vis spectrum. The maximum absorbance for the peak occurring at 272 nm was then plotted against the solution's concentration, resulting in a linear line showing an increase in the absorption at 272 nm as the concentration increased. That was then fit with a linear regression forced through the data point 0,0, from which the slope of the line was determined. A saturated solution of the monomer in RO water was then prepared. The aqueous solution was filtered, and the UV-vis spectrum was determined. Using the equation determined from the five methanol solutions and the max absorbance for the saturated aqueous solution at 272 nm, the concentration of monomer dissolved in the RO

water was determined, indicating the level of water solubility for each metal cation monomer.

3.2.3 Alkaline Stability.

3.2.3.1 NMR and GPC Polymer Stability.

Polymer samples were immersed in an aqueous 2 M KOH solution and incubated at 80 °C for up to 72 hours. Samples were removed after 0, 1, 2, 4, 8, 24, or 72 hours. Once removed, the sample was dried under vacuum at 50 °C for 24 hours. ^{1}H NMR and DMF GPC were performed on each sample to monitor degradation. Neither the ^{1}H NMR spectra nor GPC trace showed any change in molecular weight over the full 72 hours.

3.2.3.2 Stability of AEMs.

All AEMs were tested in the same way. The AEM in the chloride form was converted to the hydroxide form by ion exchange in an aqueous 1 M KOH solution for 1 hour. The membrane was then washed with RO water to remove excess ions and dried for 24 hours at 50 °C under vacuum. The dried sample was weighed and then re-immersed in DI water for 24 hours to re-hydrate it. The sample was then placed in an aqueous 2 M KOH solution and incubated at 80 °C. The AEM was removed from the solution after either 6, 24 or 48 hours, washed with RO water to remove excess ions and then dried under vacuum at 50 °C for 24 hours. The AEM was weighed for its mass after incubation and the percentage of mass remaining was calculated.

3.2.4 X-Ray scattering.

3.2.4.1 Characterization of Morphology.

SAXS measurements were conducted at room temperature on samples roughly 0.9 mm thick. The samples were loaded onto the sample holder and placed in the instrument. They were then irradiated for 360 seconds, during which the scattering profile was collected. The domain spacing's were calculated from the principle scattering maximum, q, using equation 8.

$$d = \frac{2\pi}{q} \qquad\qquad (8)$$

where d is the domain spacing and q is the principle scattering peak in nm^{-1}. The domain spacing for **CP4-5Ni**, **CP4-10Ni**, **CP4-20Ni**, **HP4-10Ni** and **HP4-20Ni** where 9.96 nm, 10.9 nm, 8.65 nm, 7.98 nm and 8.19 nm, respectively. Sample **HP4-5Ni** showed no detectable scattering peak.

3.2.4.2 Stability of Morphology.

Sample **CP4-20Ni** was measured following the scattering procedure above, except it was run swollen with liquid water. To keep the samples fully hydrated, the membranes was placed in a button holder, which was filled with water and covered with Kapton, and then screwed closed to ensure an air-tight seal. The sample was then irradiated for 360 seconds, the profile collected, and the domain spacing determined using equation 8. **CP4-20Ni** was irradiated twice, the first after formation and the second after incubation in RO water at 80 ˚C for 1 hour.

3.2.5 Water Uptake.

The fully hydrated AEM was removed from liquid water and the surface was blotted to remove surface water not absorbed into the membrane. The mass of the AEM was then

recorded immediately and the membrane placed back into water for 5-10 minutes. This process of weighing the hydrated membrane was repeated 3 times. The samples were then dried for 24 hours in vacuum at 50 °C and the dried AEM was weighed for its dehydrated mass. The percent water uptake was calculated using:

$$wu = \frac{m_{hyd} - m_{dry}}{m_{dry}} \times 100\% \tag{2}$$

where *wu* is the water uptake in percent, m_{hyd} is the average hydrated mass for all three mass measurements and m_{dry} is the dry mass.

3.2.6 Dynamic Mechanical Analysis (DMA).

The mechanical properties of all AEMs were tested using DMA while swollen and in the chloride form at room temperature. All samples were cut into rectangular films 3-6 mm wide and 15-20 mm long. Samples were tested either swollen in water or after being dried for 24 hours at 50 ˚C under vacuum. The test was run with a preload force of 0.001 N followed by a force ramp of 1 N/min until the sample broke, giving the stress and strain at break.

3.2.7 Conductivity.

3.2.7.1 In 95% Relative Humidity.

Conductivity of samples in the chloride form was performed using an electrochemical impedance spectrometer (EIS). For the measurements, aluminum mounts were first sputter coated with gold using a Cressington 108 sputter coater. Samples were first measured for their thickness, in centimeters, and then placed into a sample holder containing two electrodes, with the sample in between the two electrodes. The holder was then loaded into a custom system that multiplexes the impedance analyzer to one of eight temperature-

calibrated positions within an ESPEC SH-241 bench-top type temperature and humidity chamber. Samples were then heated at 95% relative humidity to 30 °C for 7200 seconds. Impedance spectra in the frequency range of 10 MHz-0.1 Hz were recorded for each sample at repeated time intervals of 1800 seconds, totaling four spectra per temperature. This was then repeated at 40 °C, 50 °C, 60 °C, 70 °C, 80 °C, 70 °C, 60 °C, 50 °C, 40 °C, and 30 °C, in that order. The temperature was ramped up and then back down to ensure consistency at both the beginning and end of the experiment. The bulk resistance to ion conduction, R, was then determined by fitting a constant function to the first plateau of the impedance magnitude occurring at high frequencies. The conductivity was then calculated from the known sample area, A = 0.074 cm^2, and the measured sample thickness, d, as σ = d/(AR).

3.2.7.2 In Liquid Water.

The membrane resistance was obtained from the real value of the impedance where the imaginary response was zero. The sample was placed between the electrodes, immersed in liquid water and heated to 20 °C for one hour. The membrane impedance was measured over a frequency range from 1 MHz to 100 Hz by two-point probe alternating current (AC) impedance spectroscopy three times during the hour with an AC voltage of 10 mV. This was then repeated at 20 °C up to 80 °C and then back down to 20 °C. The in-plane conductivity, σ in mS/cm, of each membrane was calculated from σ = L/RA, where L is the distance between reference electrodes, R is the resistance of the sample, and A is the cross-sectional area of the sample.

3.3 Results and Discussion

3.3.1 Thiol-Ene-Based AEMs

3.3.1.1 Morphology

Inducing phase segregation was an important goal for the development of the thiol-ene-based AEMs, so the membranes were first characterized for the presence or absence of microphase-separation. The phase separation characteristics of the materials were determined by performing room temperature small-angle X-ray scattering (SAXS) on all six membranes, both with and without nickel present (Figure 23). All membranes were studied after being dried under vacuum at 50 °C for 24 hours. When the membranes were synthesized without the addition of nickel, no scattering peak was observed for any of the samples, indicating a lack of phase separation. This seemed reasonable since the membranes were essentially hydrophobic. Interestingly, however, once nickel was added, a broad scattering peak appeared for all samples except for **HP4-5Ni**. The lack of a second order peak indicated that the phase separation did not have long range order, and thus likely arose from ionic clusters.[117,153] The formation of ionic clusters, such as those observed here, has been shown to produce membranes with enhanced conductivity, due to the formation of ion conducting channels through the hydrophobic matrix.[32,33,153,154] From Figure 23 it was determined that the interdomain spacing in the samples ranged from 8-11 nm, which is a typical range for ionic clusters in polymers.[153] However, since the **HP4** series produced AEMs that were too brittle to handle, only the **CP4** series was studied further.
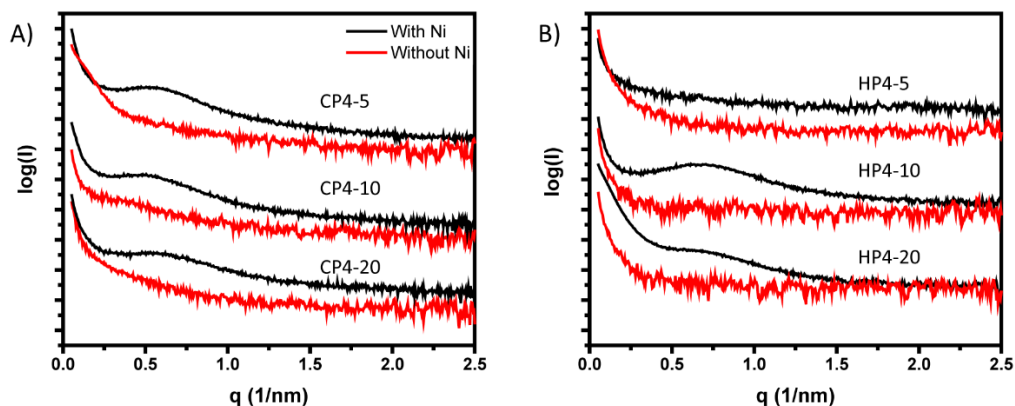
Figure 23. Room temperature SAXS patterns of A) **CP4**-based AEMs, **CP4-5** (top), **CP4-10** (middle) and **CP4-20** (bottom) and B) **HP4**-based AEMs, **HP4-5** (top), **HP4-10** (middle) and **HP4-20** (bottom), where the membranes with nickel are black and without nickel are red for both data sets.

3.3.1.2 Thermal and Alkaline Stability

The **CP4** series was then examined for the membrane's stability to high temperature and high alkaline conditions. While it was expected from the ROMP-based membranes that the nickel cation would be stable, it was important to confirm that the new chemistry used here was equally stable.[60] The thiol-ene polymer **P3** was studied for its stability in an aqueous 2 M KOH solution at 80 °C for up to 72 hours. Samples were incubated in an oven and removed after either 0, 1, 2, 4, 8, 24, or 72 hours and tested using ^{1}H NMR and GPC with DMF as an eluent. The ^{1}H NMR results are shown in Figure 24, with the GPC curves shown in Figure 25 and Table 8 for the molecular weights. As can be seen in Figure 24, there was no change in the NMR spectra of the polymer after 72 hours of incubation. Likewise, the GPC traces showed the same lack of change over the full 72 hour test. These results indicated that the polymer had excellent chemical stability, as any degradation would result in changes at one or more of the labeled peaks in the NMR and an increase in the retention time for the GPC traces, correlating to a decrease in the molecular weight.

Additionally, no insoluble fractions were observed after testing, indicating that no crosslinking occurred.
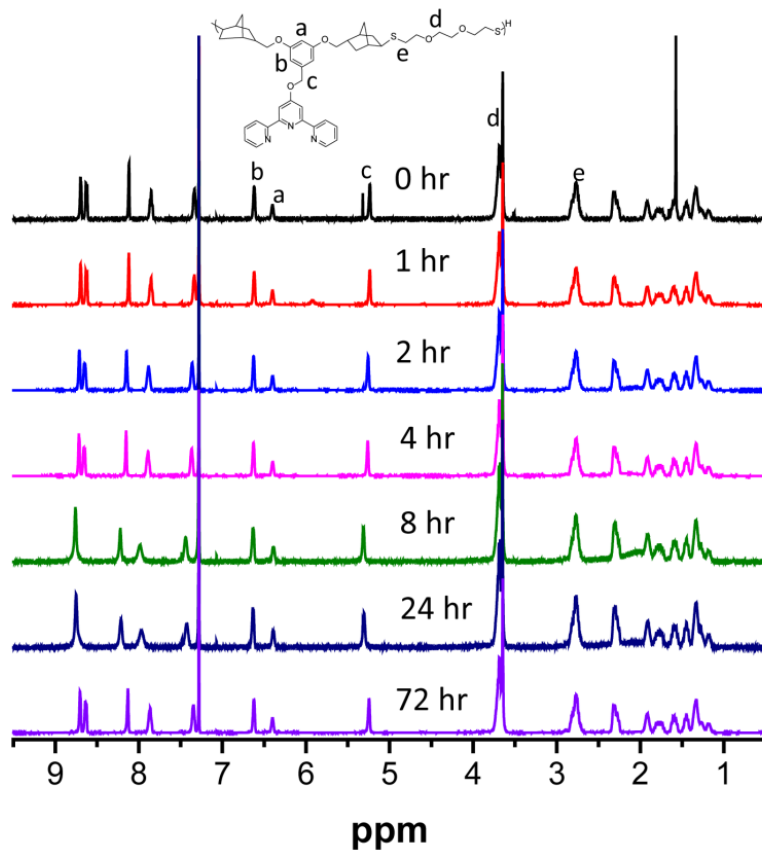
Figure 24. ^{1}H NMR spectrum, run at room temperature in CDCl$_3$ of **P3** exposed to aqueous 2 M KOH at 80 °C, at various time-points, depicting **P3's** excellent alkaline stability.
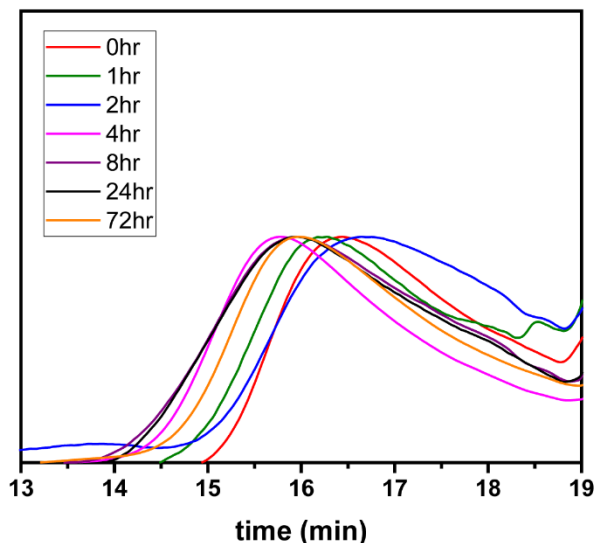
Figure 25. GPC trace with DMF as an eluent for **P3** stability after 0, 1, 2, 4, 8, 24, or 72 hours incubation at 80°C in aqueous 2 M KOH.

Table 8. Molecular weights and dispersity for **P3** stability after 0, 1, 2, 4, 8, 24, or 72 hours incubation at 80°C in aqueous 2 M KOH.

Time (hr)	M_p	M_n	M_w	D
0	7,661	5,095	7,152	1.40
1	8,754	6,221	8,446	1.36
2	6,378	3,679	6,137	1.67
4	13,275	7,025	11,708	1.67
8	11,288	6,761	11,437	1.69
24	11,529	5,891	11,949	2.03
72	9,900	5,453	8,676	1.59

The AEMs were then studied for their alkaline stability, to ensure that the nickel complex and the PS backbone had the expected stability. The alkaline stability was determined by weighing the sample for its dried mass both before and after incubation in an aqueous 2 M KOH solution at 80 °C for 48 hours, where more mass remaining indicated better alkaline stability (Figure 26). As can be seen, all samples demonstrated greater than 97 % mass remaining after 48 hours incubation, where the 2-3 % mass loss is most likely

due to the loss of any remaining sol fraction not fully removed in the transition from NMP to liquid water.
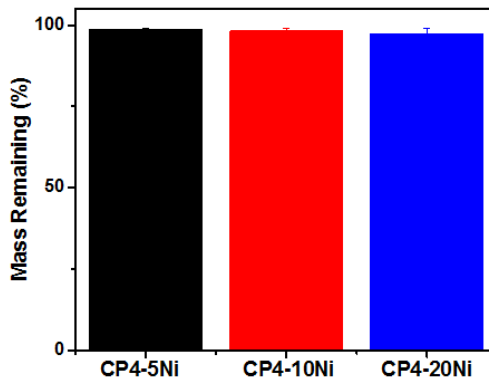
Figure 26. Mass stability of **CP4-**based AEMs in an aqueous 2 M KOH solution at 80°C for 48 hours. The data represents the amount of mass remaining in each membrane after incubation.

Lastly, the stability of the morphology to high temperature conditions was studied using room temperature SAXS of **CP4-20Ni** after first being stored in liquid water for three months and then after incubation at 80 °C for one hour. For that sample, the SAXS patterns were taken while swollen in water to ensure that only the effect of temperature was measured, although after further experiments, no difference between a dried and swollen network was observed (Figure 27). The initial scattering profile is compared to the membrane after storage for three months (Figure 28) and after heating for 1 hour at 80 ˚C (Figure 29), and the arrow on each plot represents the peak maximum. As can be seen, there was no significant change in the scattering peak after storage in liquid water at room temperature for three months. After incubation at 80 °C for one hour it is obvious that the scattering peak shifted to a lower q value, from 8.7 nm to 11.8 nm, indicating an increase in the domain spacing of the material. Upon incubation at 80 °C for another three hours,

only a minimal shift in the scattering peak was observed, indicating that the morphology became stable after the first hour (Figure 30).
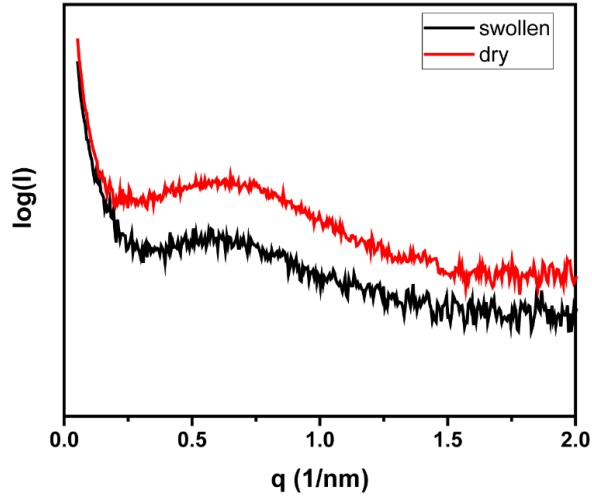
Figure 27. SAXS profile for **CP4-20Ni** swollen (black) and dried (red) demonstrating no dependence on hydration for the interdomain spacing.
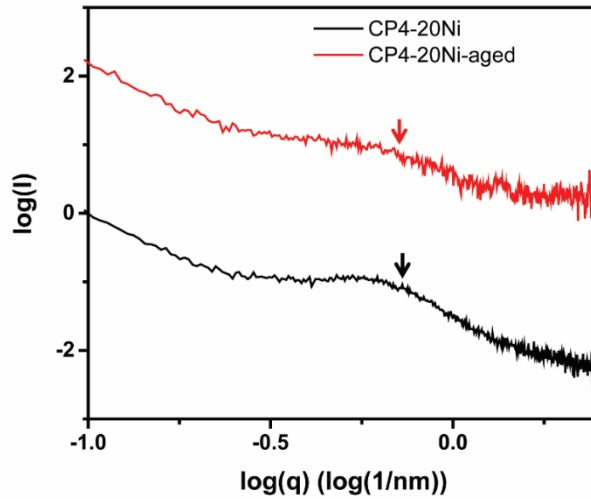
Figure 28. SAXS profile in liquid water for **CP4-20Ni** immediately after fabrication (black) and after storage for three months in liquid water (red) demonstrating no dependence on time for the morphology.
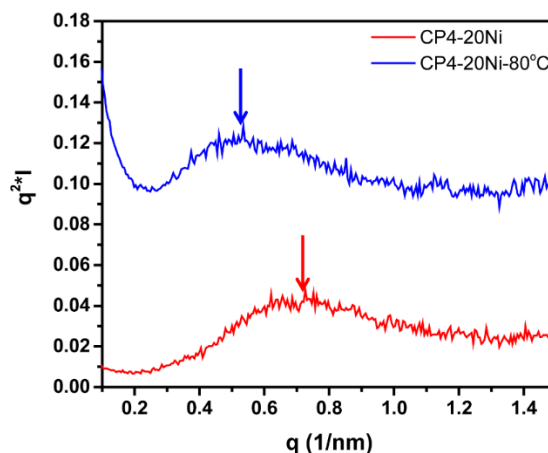
Figure 29. Room temperature SAXS patterns in liquid water showing the evolution of the AEM **CP4-20Ni** morphology with time and temperature. Peak maximum, represented by arrows, shifts to lower q after incubation at 80 °C for 1 hour.
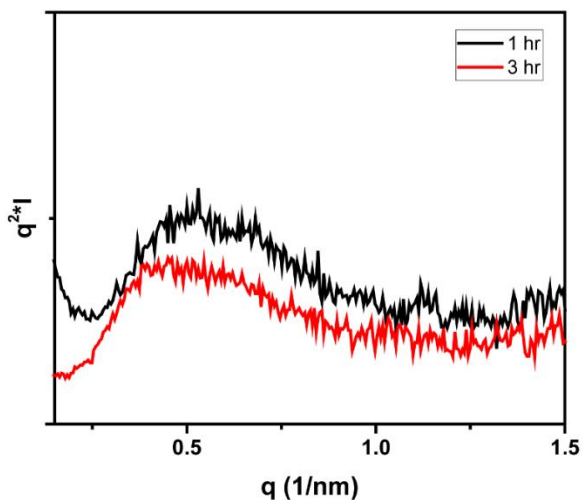
Figure 30. SAXS profile in liquid water (q^2I vs q Kratky plot) for **CP4-20Ni** after incubation in liquid water at 80 °C for one hour (black) and three hours (red) demonstrating minimal difference in interdomain spacing after additional incubation in liquid water.

3.3.1.3 Water Uptake

The **CP4**-based samples were then studied for their water uptake, as it has a direct impact on both the conductive and mechanical properties of the AEM.[31,87] Water uptake was calculated from the difference between the swollen mass and the dried mass of the

81

membrane, where it was dried for 24 hours under vacuum at 50 °C (Table 9). As can be seen, **CP4-5Ni** and **CP4-10Ni** both had water uptake around 150%, and **CP4-20Ni** showed a large increase to 240%. A lack of increase in water uptake between **CP4-5Ni** and **CP4-10Ni** was surprising, as increasing the cation content was expected to increase the water content of the material. However, the simultaneously high crosslink density could have limited the membrane's ability to swell in water. Once enough cations were incorporated, as in **CP4-20Ni**, the cation content played a more crucial role, which resulted in a large increase in water uptake. All three samples, however, demonstrated high water content, especially for a moderate IEC of 1 mmol/g, as the goal would be to keep water uptake closer to Nafion's 38%.[39]

Table 9. Membrane properties for **CP4-**based AEMs.

Sample	Water Uptake (%)[a]	IEC$_{exp}$ (mmol/g)[b]	Tensile Stress at Break (MPa)[c]	Tensile Strain at Break (%)[c]
CP4-5Ni	153.9 ± 23.4	0.98 ± 0.09	1.64 ± 0.14	6.10 ± 1.63
CP4-10Ni	156.9 ± 18.4	1.07 ± 0.07	2.55 ± 0.64	6.52 ± 3.46
CP4-20Ni	238.0 ± 13.6	1.13 ± 0.20	3.06 ± 0.73	11.42 ± 3.14

[a]Liquid water uptake values in the Cl$^-$ form at room temperature. [b]Ion exchange capacity determined by back titration, average of three trials. [c]Mechanical properties obtained using dynamic mechanical analysis in the Cl$^-$ form at room temperature while swollen with liquid water, average of three trials.

3.3.1.4 Mechanical Properties

Since water content can have a direct impact on the mechanical stability of AEMs, all three samples were then studied for their tensile strength at break using dynamic mechanical analysis (DMA). Samples were first synthesized in a rectangular mold, and once fully hydrated in liquid water, they were tested for their room temperature tensile stress and strain at break (Table 9 and Figure 31). As can be seen, all three samples showed weak mechanical properties, with **CP4-5Ni** and **CP4-10Ni** having very similar stresses and

strains at break of 1.5-2.5 MPa and 6%, respectively. **CP4-20Ni** had a similar stress at break of 3 MPa, but a strain at break about twice that of the other two samples, 11%. These values indicated that the mechanical properties were strongly influenced by the water content of the membrane, as the membranes with similar water content had similar mechanical properties and **CP4-20Ni**, which had much higher water uptake, also had a larger elongation at break. The poor mechanical properties can be attributed to both the high water content as well as the high crosslink density of the materials, since each nickel cation acted both as an ion conductor and a crosslinker. To demonstrate this, samples without the nickel cation crosslinker were tested, exhibiting more robust mechanical properties due to the lower crosslink density (Figure 32). Due to the high equilibrium kinetics for the nickel-terpyridine bond, forming non-crosslinking, heteroleptic complexes was difficult to accomplish and would have required very specific conditions.[137,155–157] Therefore, with the current chemistry, it is difficult to de-couple the crosslink density from the metal-cation content, resulting in a significant challenge facing metal complex-containing materials, such as these AEMs.
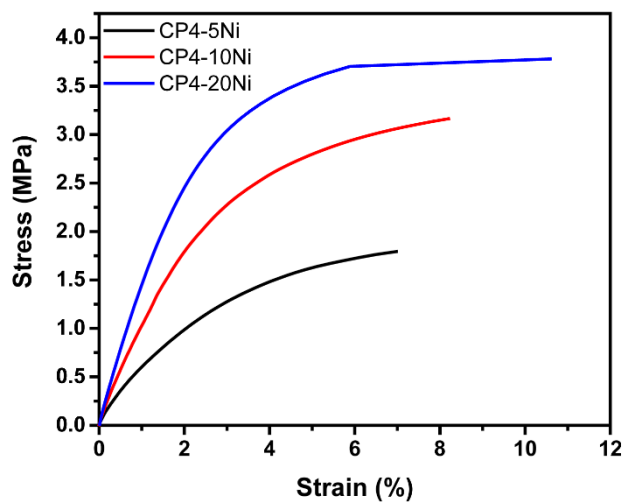
Figure 31. Representative mechanical data for the **CP4-Ni** series using dynamic mechanical analysis.
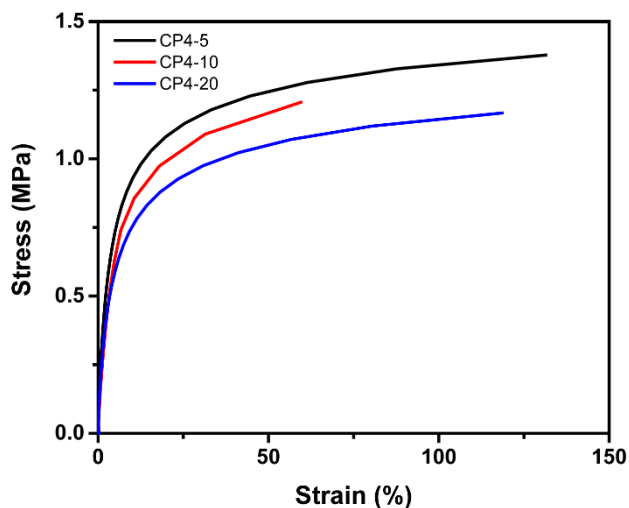
Figure 32. Representative mechanical data for the **CP4** series without nickel cation crosslinkers using dynamic mechanical analysis.

3.3.1.5 Chloride Conductivity

Finally, **CP4-20Ni** was tested for its chloride ion conductivity as a function of temperature in liquid water. **CP4-5Ni** and **CP4-10Ni** were not tested due to their weak

mechanical properties. Figure 33 represents the data as the sample was heated from 20-80 °C and then cooled back down to 20 °C, with measurements taken every 20 °C, showing that the sample maintained the same conductivity after heating to 80 °C. It is important to note, however, that the conductivity data was collected after first heating the sample to 80 °C for at least an hour. Samples that were not initially heated demonstrated an increase in conductivity from 20-50 °C, but then a sharp decrease in conductivity from 60-80 °C (Figure 34). However, when the same sample were tested a second time, the data in Figure 33 was observed. This decrease in conductivity during the first pass is most likely related to the shift in the primary scattering peak to lower q values after heating to 80 °C.[10] For the second heating, the conductivity values increased with temperature, but remain very low for **CP4-20Ni**, with a maximum conductivity of 1.34 mS/cm at 80 °C. This low conductivity could be due to the high water content, despite the moderate IEC value, which resulted in a large number of water molecules per cation in the membrane that diluted out the anions. It is also likely that the ion clusters observed did not form the interconnected ion conducting pathways required to produce high conductivity.
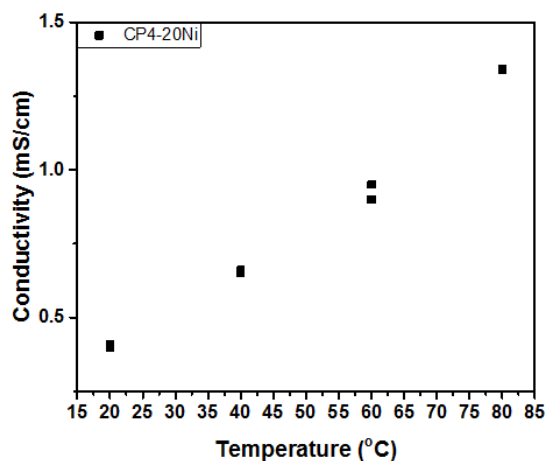
Figure 33. Representative chloride conductivity for AEM **CP4-20Ni** as a function of temperature in liquid water. Data shown is for conductivity of the second heating to account for the change in morphology observed after initial heating.
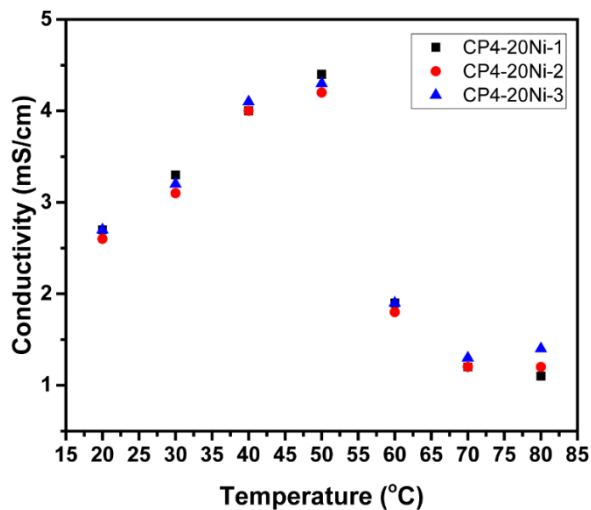
Figure 34. Initial chloride conductivity for **CP4-20Ni** as a function of temperature in liquid water showing a decrease in conductivity above 50 °C.

3.3.2 ROMP-Based AEMs

3.3.2.1 Chloride Ion Properties

3.3.2.1.1 AEMs Without a PEO Crosslinker

3.3.2.1.1.1 Water Uptake

The resulting ROMP-based membranes were first studied for their water uptake in the chloride form, as measured by comparing the masses of the hydrated and dried membranes. Initially, the membranes without a poly(ethylene oxide) (PEO) crosslinker were studied at three different metal cation contents, with a mole fraction (f) = 0.17, 0.33, and 0.5 (Table 10). This was performed to determine the effect that the cation's identity had on AEM water uptake and how that effect was impacted at different mole fractions. The swelling data indicates that changing the transition metal appears to have little effect on the amount of water absorbed into the network, as membranes at the same cationic f all had similar water uptake values. Furthermore, as the cationic f increased, that trend continued where the metal center had minimal impact on the water uptake, even at higher incorporations. Not surprisingly, as the number of metal cations in the network was increased, the average water uptake values also increased. This was expected as increasing the cationic content in an AEM enhances the hydrophilicity of the network and increases the water uptake. Typically, changing the identity of the cation leads to differences in AEM water uptake, indicating that these ROMP-based AEMs have potential to be good model membranes for understanding the impact of cation identity on AEM ion conductivity without affecting other properties.

Table 10. Membrane properties for all AEMs without a PEO crosslinker.

AEM	Water Uptake (%)[a]	Mass Remaining (%)[b]	$\sigma^*(Cl^-)_{80\,°C}$ (mS/cm)[c]	Tensile stress at break (MPa)[d]	Tensile strain at break (%)[d]
[0.17]Ru	28.0	94 ± 3.1	0.78	37 ± 22[1]	13 ± 5.8[1]
[0.33]Ru	80.2 ± 14.7	72 ± 14.7	-	4.9 ± 2.1[2]	14.8 ± 3.3[2]
[0.5]Ru	98.9 ± 15.2	59 ± 15.2	-	4.2 ± 1.2[2]	5.0 ± 1.1[2]
[0.17]Ni	36.0	98 ± 4.1	2.28	45 ± 12[1]	7.9 ± 2.9[1]
[0.33]Ni	72.5 ± 3.6	94 ± 3.6	-	8.2 ± 0.5[2]	30.2 ± 13.1[2]
[0.5]Ni	97.8 ± 8.2	89 ± 8.2	-	3.7 ± 3.0[2]	12.3 ± 8.4[2]
[0.17]Co	29.0	99 ± 0.5	0.36	56 ± 17[1]	8.3 ± 3.5[1]
[0.33]Co	68.6 ± 3.7	95 ± 3.7	-	19.3 ± 4.6[2]	24.5 ± 9.7[2]
[0.5]Co	78.6 ± 1.1	86 ± 1.1	-	9.4 ± 3.2[2]	8.0 ± 5.3[2]

[a]Liquid water uptake in the Cl^- form at room temperature, where water uptake = $[(m_{wet} - m_{dry})/m_{dry}]$. [b]Percent of dried mass remaining with membranes in the OH^- form after 48 hr at 80 °C in an aqueous 2 M KOH solution. [c]Cl^- conductivity at 95% relative humidity and 80 °C [d]Mechanical properties obtained using dynamic mechanical analysis in the Cl^- form and in either the dried[1] or swollen[2] state. Average values, with errors, from three trials.

3.3.2.1.1.2 Mechanical Properties

Membranes need enough mechanical strength to allow for facile handling while membrane characterizations are performed. Therefore, the ROMP-based AEMs without a PEO crosslinker were tested for their mechanical stability by cutting the samples into rectangular films and testing them using dynamic mechanical analysis (DMA) at a preload force of 0.001 N and a force ramp of 1 N/min to obtain the tensile stress and strain at break (Figure 35). The AEMs with a cationic $f = 0.17$ were tested dried while the samples containing a cationic $f = 0.33$ and 0.5 where tested while swollen in water. For the [0.17]M samples, all samples showed similar stresses and strains at break with a stress at break ranging from 27-56 MPa and a strain at break ranging from 8-13%. In conjunction with those membranes, the [0.33]M and [0.5]M samples showed a similar trend, where the identity of the cation had minimal effect on the stress and strain at break for these metal cation-based AEMs when swollen in water. The similarities in mechanical properties indicated that

differences in the metal-terpyridine equilibrium kinetics for the ruthenium, nickel, and cobalt metal cations did not impact mechanical stability, despite the fact that these monomers also acted as crosslinkers. It appears as though the covalent crosslinks from the DCPD dominates the mechanical properties for these membranes. Thus all samples, regardless of metal incorporated, have comparable mechanical properties both within this series as well as with respect to literature values.[39,108]
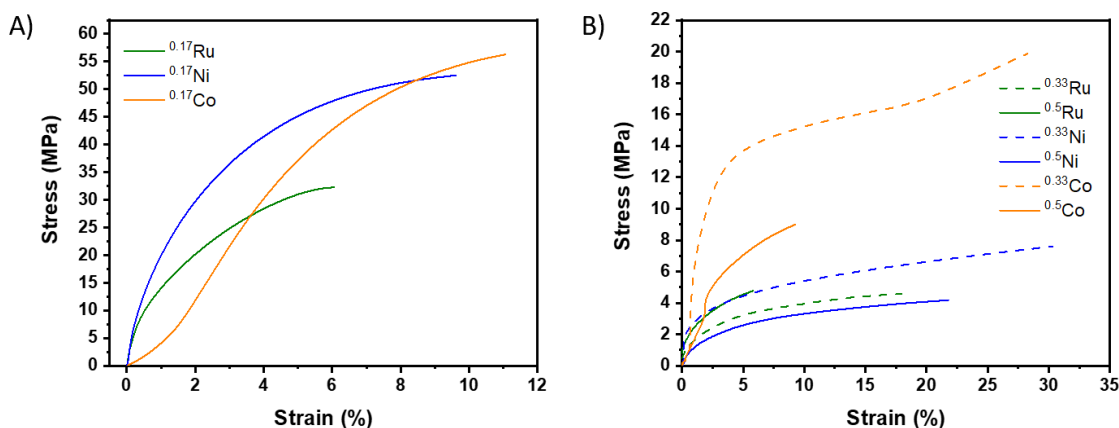
Figure 35. Representative room temperature stress and strain curves for A) $^{0.17}$M AEMs dried and B) $^{0.33}$M and $^{0.5}$M AEMs swollen in water in the chloride form.

Interestingly, the $^{0.33}$M and $^{0.5}$M samples showed that at this force ramp increasing the metal complex content resulted in mechanically weaker membranes, as both the average stress and strain at break decreased for the higher metal complex content materials. This indicated that the labile metal complex crosslinks were more easily broken than the covalent DCPD crosslinks, which would be expected. This demonstrates a challenge with using metal cations in AEMs. Due to the lability of the metal-terpyridine bonds, synthesizing non-crosslinking, heteroleptic complexes for metals other than ruthenium is very difficult, but using the metal cation monomer as a crosslinker limits the number of

cations that can be incorporated into the network while maintaining robust mechanical properties.

3.3.2.1.1.3 Alkaline Stability

The lack of alkaline stability is a major limitation for AEM materials. Therefore, the ROMP-based AEMs without a PEO crosslinker were tested for their alkaline stability by monitoring their mass loss, as measured in the dried state, after incubation in an aqueous 2M KOH solution at 80 °C for up to 48 hours (Figure 36). At the lowest cationic f, all AEMs showed excellent stability after the full 48 hours of incubation, with **0.17Ru** showing 94% of its mass remaining after incubation and **0.17Ni** and **0.17Co** samples showing greater than 98% mass remaining. As the cationic f was increased, the nickel and cobalt samples maintained very good chemical stability, while the ruthenium showed a surprising drop in mass% remaining. It is likely that the mass loss observed for the ruthenium samples was due to loss of the sol fraction, as opposed to degradation of the network, as bis(terpyridine) ruthenium complexes are known to be stable in alkaline conditions.[11,59] This shows that despite introducing more labile metal-ligand bonds into these membranes with nickel and cobalt, robust chemical stability was maintained.
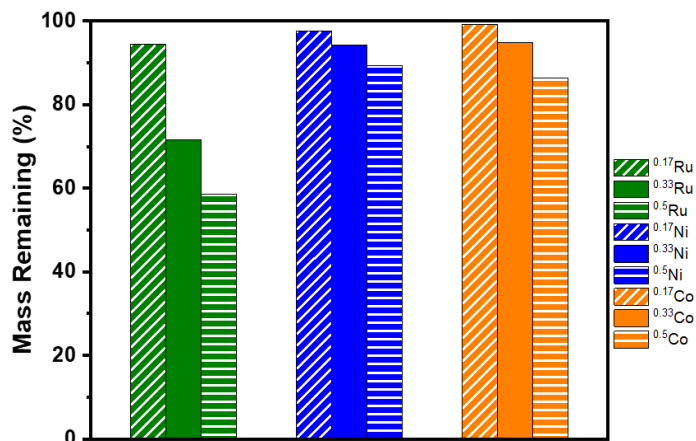
Figure 36. Mass stability in an aqueous 2 M KOH solution at 80 ˚C for 48 hours. The data indicates the amount of mass remaining after 48 hours as a percent.

3.3.2.1.1.4 Ion Conductivity

To determine how conductivity varied with metal ion, chloride conductivity was measured as a function of temperature at 95% relative humidity for the **0.17M** samples (Figure 37). As expected, all samples showed an increase in conductivity with temperature, due to the increase in ion mobility at elevated temperatures. Interestingly, different metal cations facilitated different levels of ion conduction, with the nickel-based AEM showing the highest conductivity of 2.4 mS/cm, while **0.17Ru** showed an intermediate conductivity of 0.92 mS/cm and **0.17Co** showed the lowest conductivity of 0.3 mS/cm. This enhanced ion conductivity for the nickel-based sample was not due to a larger IEC value, as all three **0.17M** samples showed similar experimental IEC values. These results highlight the impact of cation identity on AEM ion conduction, as these membranes had different levels of ion conduction but similar bulk properties. Therefore, further exploring this phenomenon and understanding what causes nickel to facilitate better chloride ion conduction was explored.
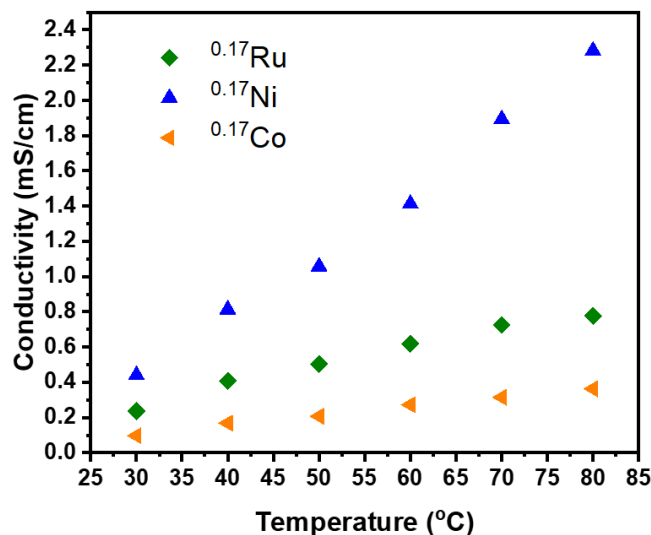
Figure 37. Chloride conductivity for the $^{0.17}$M AEMs as a function of temperature in 95% relative humidity. All samples show an increase in conductivity with temperature.

3.3.2.1.2 AEMs With the PEO Crosslinker Containing Ester Linkages

3.3.2.1.2.1 Water Uptake

To further explore the impact of the metal cation on ion conduction, membranes containing a di-norbornene functionalized PEO crosslinker containing ester linkages were synthesized from ruthenium, nickel, and cobalt cations. The PEO crosslinker was added primarily to increase the water uptake and improve mechanical stability, due to the poor mechanical properties of the AEMs without a PEO crosslinker. Not surprisingly, the PEO-containing samples demonstrated higher water uptake, 150-170 wt%, with $^{0.55}$Ni$_{PEOes}$ demonstrating 190% uptake by mass (Table 11). The addition of a PEO crosslinker increased the water uptake due to the hydrophilic nature of the PEO, which influence the water uptake similarly to increasing the cationic *f* in the network. Similar to the membranes without a PEO crosslinker, all membranes showed similar water uptake at the same cationic *f*, regardless of the metal center utilized, where the average water uptake increased as the

cationic *f* increased. The alkaline stability for the AEMs containing PEO crosslinkers was not obtained because they were designed knowing they would not have robust chemical stability, but since they were synthesized to explore the impact of cation identity on AEM ion conduction the lack of chemical stability was acceptable.

Table 11. Membrane properties for all AEMs containing the PEO crosslinker with ester linkages.

Sample	Water Uptake (%)^a	Stress at Break (MPa)^b	Strain at Break (%)^b	E_a (kJ/mol)
$^{0.36}$Ru$_{PEOes}$	169 ± 53	4.0 ± 2.1	80.5 ± 15.2	15.6
$^{0.55}$Ru$_{PEOes}$	152 ± 25	2.2 ± 2.0	37.0 ± 23.3	16.2
$^{0.36}$Ni$_{PEOes}$	162 ± 27	5.4 ± 2.9	95.5 ± 13.5	16.3
$^{0.55}$Ni$_{PEOes}$	193 ± 46	4.1 ± 2.8	66.8 ± 23.5	16.5
$^{0.36}$Co$_{PEOes}$	154 ± 12	6.8 ± 1.7	115.0 ± 23.6	15.1
$^{0.55}$Co$_{PEOes}$	152 ± 29	3.5 ± 1.2	39.7 ± 9.2	--

^{a}Liquid water uptake values, average of three trials, for AEMs in the Cl$^-$ form at room temperature, where water uptake = $[(m_{wet} - m_{dry})/m_{dry}]$. ^{b}Average of three trials, calculated using dynamic mechanical analysis for AEMs swollen in water and in the Cl$^-$ form.

3.3.2.1.2.2 Mechanical Properties

Addition of a long, hydrophilic crosslinker has been shown previously to improve the mechanical properties in AEMs.[105] Therefore, the membranes containing the PEO crosslinker with ester linkages were tested using DMA to determine their tensile stress and strain at break while swollen with water (Figure 38). No difference was observed between materials with different metal cation centers, most likely due to the similar water uptake and the covalent DCPD crosslinks playing a more dominant role in the mechanical properties than the metal identity. In addition, as the metal complex content was increased, the membranes became weaker as both the average stress and strain at break decreased for the high metal complex content materials, similar to the AEMs without a PEO crosslinker. While the lower metal complex content series had stresses at break between 4-6 MPa and

strains at break between 80-115%, the higher metal complex content series only had a stress at break of 2-4 MPa and a strain at break of 35-65%. This data, however, confirms that adding a long, hydrophilic crosslinker results in good mechanical properties for these types of materials.
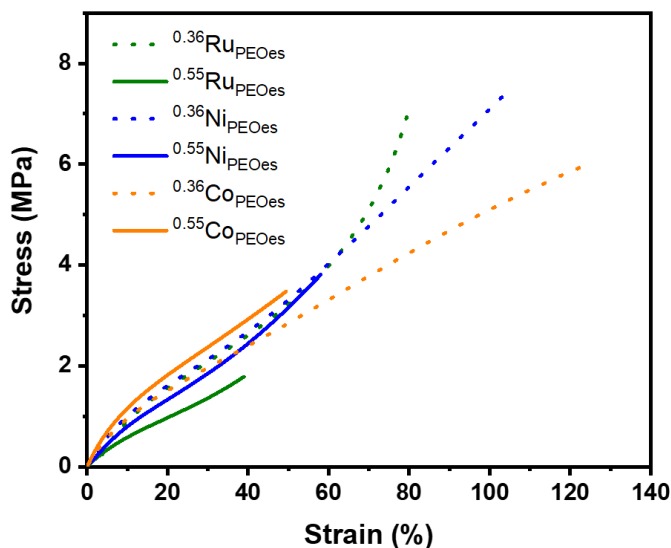
Figure 38. Representative room temperature stress and strain curves from DMA for all AEMs containing the PEO crosslinker with ester linkages while swollen with water and in the chloride form.

3.3.2.1.2.3 Ion Conductivity

To further explore the impact of metal cation identity on ion conduction, the PEO-containing samples with ester linkages were characterized for their chloride ion conductivity in liquid water as a function of temperature. Liquid water was used in this case to enhance the ion conduction in an attempt to better elucidate differences between the samples. Conductivity measurements were taken at 20 °C, 30 °C, 40 °C, 60 °C, and 80 °C, as shown in Figure 39. The conductivity of sample $^{0.55}Co_{PEOes}$ could not be studied as it was mechanically too weak and fractured when inserted into the conductivity cell. As expected, all samples demonstrated an increase in conductivity with temperature. In

addition, as the metal complex content was increased from $f = 0.36$ to 0.55, the conductivity

increased as well. All three membranes with a lower mole fraction had similar conductivity,

contrary to the $^{0.17}$M samples that showed nickel-based AEMs exhibiting better

conductivity than cobalt- and ruthenium-based AEMs. Importantly, that data was collected

at 95% RH as opposed to liquid water, which may be significant.[60] It is possible that the

combination of being tested in liquid water and the higher water content of these samples

promoted increased mobility of the chloride ions, which diminished the conductivity

differences between metal cations.[87] As the metal content increased, however, $^{0.55}$**Ni**$_{\text{PEOes}}$

showed a larger increase in conductivity than $^{0.55}$**Ru**$_{\text{PEOes}}$, consistent with the above trend.[60]
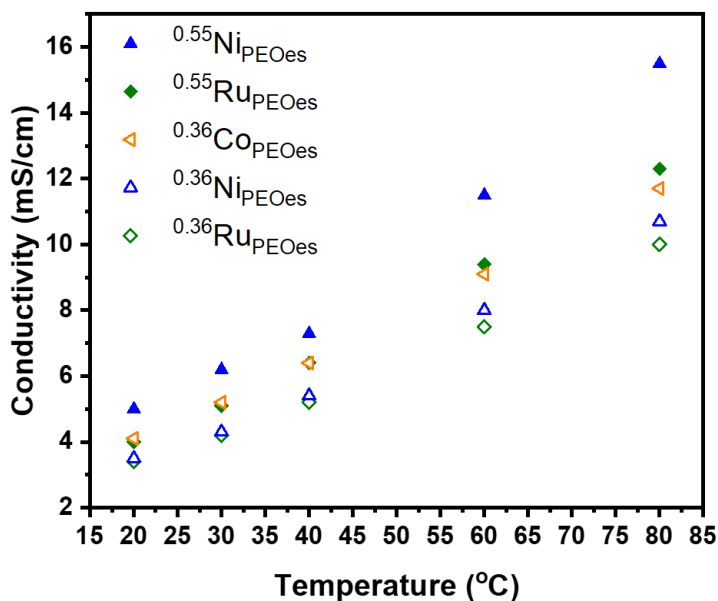
Figure 39. Chloride conductivity for the AEMs containing the PEO crosslinker with ester linkages in liquid water as a function of temperature. Sample $^{0.55}$**CoPEOes** was not tested as it was too weak and broke in the conductivity cell.

To better understand this conductivity data, the conductivity values at 80 °C for

each sample were plotted as a function of bulk hydration number (λ), as shown in Figure

40. The hydration number, or number of water molecules in the membrane per cation, for

the samples was calculated using equations 1 and 2 (reshown below), and is derived from the bulk hydration of the membrane:

$$\lambda = \frac{1000 \; x \; WU}{M_{H_2O} \; x \; IEC} \qquad (1)$$

$$WU = \frac{m_{hyd} - m_{dry}}{m_{dry}} \times 100\% \qquad (2)$$

where WU is the water uptake in percent, M_{H_2O} is the molecular mass of water, 18.015 g/mol, IEC is the calculated IEC of the membrane, m_{hyd} is the hydrated mass of the AEM, and m_{dry} is the dry mass of the AEM.[11,117] AEM [0.55]CoPEOes, not shown, had a λ of 98.
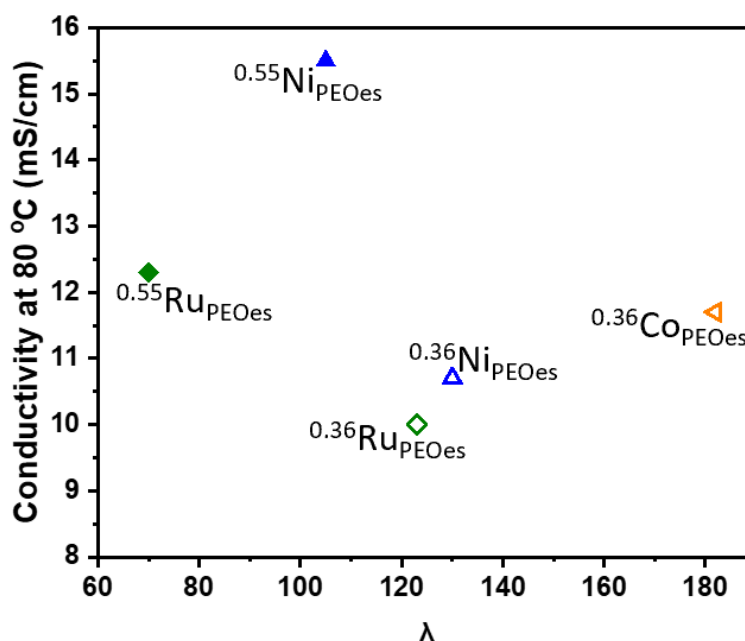
Figure 40. Chloride conductivity at 80 °C plotted versus bulk hydration number, λ, for each AEM with the PEO crosslinker containing ester linkages. Sample [0.55]CoPEO was not tested as it was too weak and broke in the conductivity cell.

When the AEM conductivity data was plotted against λ, it became clear that increasing the metal complex content, from $f = 0.36$ to 0.55, did not increase the amount of water molecules per cation (λ). While a correlation between AEM cation content and

water per cation has been observed for other AEMs and PEMs, it was surprising that here the hydration number appeared to decrease as the metal cation content increased.[29] In this case, the nickel complex showed the smallest decrease in λ, with a decrease of 20%, while ruthenium- and cobalt complex-based samples showed declines of 32% and 46%, respectively. All six samples had hydration numbers ranging from 75-130, except for **0.36CoPEOes**, and while the conductivity and λ of samples with the same *f* appeared to have a positive correlation, that correlation broke down when comparing between AEMs with different *f*. For example, **0.55RuPEOes** and **0.55NiPEOes** both had similar or lower λ values, but higher conductivity, than their corresponding 0.36 mole fraction samples, indicating the metal content had a larger impact on conductivity than λ.

The conductivity at 80 °C was then plotted as a function of ion concentration, calculated using equation 3 (reshown below) (Figure 41):

$$c = 0.001 \; x \; \frac{\rho \; x \; IEC}{1+0.01WU} \tag{3}$$

where c is ion concentration in mmol/mL and ρ is the density of the sample measured by determining its volume and mass.[11,117] AEM **0.55CoPEOes**, again not shown, had an ion concentration of 0.39 mmol/mL. AEM **0.55NiPEOes** had the largest ion concentration, greater than 0.46 mmol/mL, while all other samples had similar ion concentrations between 0.25-0.39 mmol/mL (Figure 41). While **0.55NiPEOes** had both the highest ion concentration and conductivity, ion concentration could not explain all of the conductivity data. For example, **0.36CoPEOes** had the lowest ion concentration, 0.25 mmol/mL, but also the third highest conductivity, 11.7 mS/cm at 80 °C.
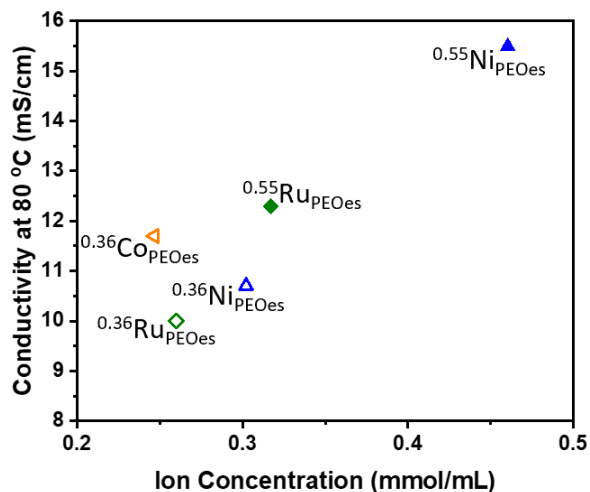
Figure 41. Chloride conductivity at 80 °C plotted versus ion concentration for each AEM with the PEO crosslinker containing ester linkages. Sample $^{0.55}$**CoPEO** was not tested as it was too weak and broke in the conductivity cell.

The observations in Figures 40 and 41 can be further explained by understanding the relationship between λ and ion concentration, as illustrated by comparing equations 9 and 10.

$$\lambda \propto \frac{WU}{IEC} \tag{9}$$

$$c \propto \frac{IEC}{WU} \tag{10}$$

From combining these two equations, λ and ion concentration become inversely related for a fixed IEC, indicating that for one to increase, the other must decrease. Since the IEC and water uptake are closely related, as the IEC of a sample increases, the water uptake usually increases by a similar, or larger factor, resulting in both λ and ion concentration remaining fairly constant.[11,29,71,105] However, Figures 40 and 41 show that as the metal content increased for all three metal cations the hydration number decreased, while the ion concentration increased. That relationship indicated that the water uptake for all three samples did not increase by as large of a margin as the IEC, most likely due to the

98

hydrophobic nature of all three metal complex monomers, counteracting the effect of the increased IEC. The addition of hydrophobic moieties to cations in AEMs, such as alkyl side chains, is a strategy that leads to lower water uptake values in the material.[71] However, in this case with relatively hydrophobic ionic comonomers, the ion content can be increased without drastically influencing the water uptake, which is unusual.

While the relationship between λ and ion concentration can be further explored through equations 9 and 10, Figures 40 and 41 ultimately show that these three parameters (λ, ion concentration, and IEC) were not sufficient to account for the nickel cation-based AEM's superior conductivity. Therefore, the activation energy of ion conduction, E_a, which relates to the kinetics of ion conduction through the Arrhenius equation, was calculated for each membrane by plotting the natural logarithm of its chloride ion conductivity versus 1000/T (Figure 42). E_a was then determined from the slope of the best fit linear regression, using the following form of the Arrhenius equation, equation 6 (reshown below):

$$\ln(\sigma_{Cl^-}) = \ln(\sigma_0) - \frac{E_a}{RT} \qquad \textbf{(6)}$$

where σ_{Cl^-} is the ion conductivity, σ_0 is the pre-exponential factor, R is the gas constant and T is the absolute temperature (Table 11 and Figure 42).[11,153] All AEMs had similar activation energies, between 15.1-16.5 kJ/mol, indicating neither metal content nor metal center had an effect on the mobility of the chloride ions within the AEM for chloride conductivity.[158]
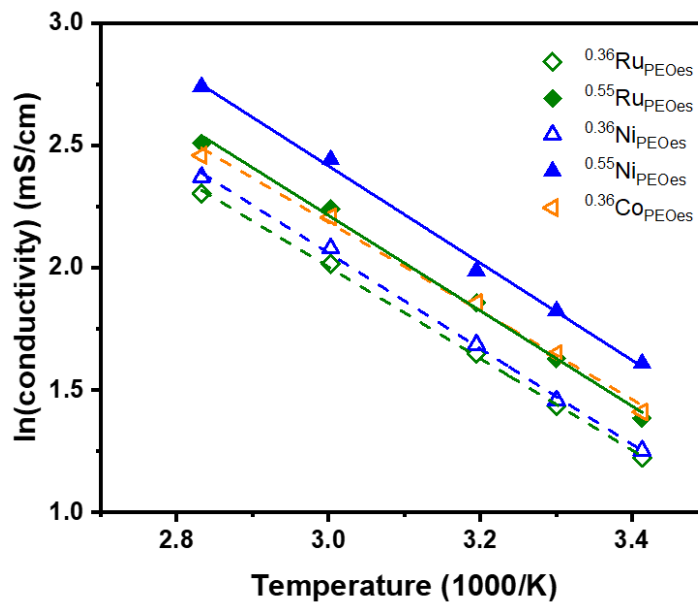
Figure 42. Chloride conductivity for the AEMs with the PEO crosslinker containing ester linkages as a function of temperature, where the E_a was calculated from the slope of the linear regression.

3.3.2.1.3 AEMs With the PEO Crosslinker Containing Ether Linkages

3.3.2.1.3.1 Water Uptake

Due to the increase in water uptake observed upon addition of the PEO crosslinker with ester linkages, the third type of AEM was synthesized with a PEO crosslinker containing ether linkages. The PEO crosslinker with ether linkages was added to demonstrate the capability of using long, hydrophilic, macromonomer crosslinkers to enhance mechanical properties in AEMs without sacrificing alkaline stability. For this type of material six metal-based cations were used: ruthenium, nickel, cobalt, iron, manganese, and zinc. All membranes showed similar water uptake values between 100-143 wt%, except for the zinc-based AEM, which had a larger water uptake of 251 wt% (Table 12). In addition to the zinc-based sample's larger water uptake, the manganese-based sample showed a larger water uptake than its IEC would predict, as compared to the other metal cations.

Since this enhanced water uptake was not due to the incorporation of a larger number of cationic monomers, as shown through the IEC values previously, the water solubility of each norbornene-functionalized metal cation monomer was determined. The water solubility was determined to confirm that the larger water uptake observed for the manganese- and zinc-based AEMs as compared to what was expected for their IEC values was not due to better water solubility of these monomers over the other four metal cations. UV-vis spectroscopy of each metal cation monomer was used to determine the water solubility. The absorbance intensity for each monomer at 243 nm was determined at five different concentrations in methanol and compared to the absorbance intensity of the monomer at 243 nm for a saturated aqueous solution (Figure 43 and Table 13). The absorbance for the aqueous solution fits onto the line obtained from the five methanol solutions and the concentration at which the monomer would produce that absorbance intensity in methanol corresponds to the concentration of monomer dissolved in the water. Since the aqueous solution was saturated, the concentration obtained represents the maximum number of monomers that can be dissolved in water, where a larger concentration corresponds to better water solubility.

The manganese- and zinc-based cations demonstrated the two lowest water solubilities, showing that the larger-than-expected water uptake values was not due to better water solubility of these monomers. Therefore, the manganese- and zinc-based AEM's higher-than-expected water uptake was likely a result of their metal-terpyridine bonds' more rapid equilibrium kinetics as compared to the other four metal-terpyridine bonds, allowing for more metal complex rearrangement and thus more expansion of the membrane as it swelled in water.[137,147,148] Given the improvement upon mechanical

properties observed for the $^{0.36}$M$_{PEOes}$ and $^{0.55}$M$_{PEOes}$ membranes, the $^{0.55}$M$_{PEOet}$ membranes were not characterized for their mechanical properties, as exploration of their conductive properties was the primary focus.

Table 12. Membrane properties for all $^{0.55}$M$_{PEOet}$ AEMs.

Sample	WU$_{Cl}$ (%)[a]	WU$_{OAc}$ (%)[b]	λ_{Cl}[c]	λ_{OAc}[d]	E$_a$ (kJ/mol)[e]	σ$_{Cl}$ (mS/cm)[f]	σ$_{OAc}$ (mS/cm)[g]
$^{0.55}$Ni$_{PEOet}$	121	86.6	38	27	27.7	21.4	10.2
$^{0.55}$Ru$_{PEOet}$	152	124.7	75	44	16.2	12.3	9.3
$^{0.55}$Co$_{PEOet}$	152	228.9	-	76	-	-	10.2
$^{0.55}$Mn$_{PEOet}$	100	428.7	82	350	13.7	6.7	1.8
$^{0.55}$Zn$_{PEOet}$	251	55	110	24	-	4.9	6.7
$^{0.55}$Fe$_{PEOet}$	143	158.3	45	50	8.4	29.6	7.9

[a]Water uptake for membranes in the chloride form at 30 °C. [b]Water uptake for membranes in the acetate form at 30 °C. [c]Hydration number for membranes in the chloride form. [d]Hydration number for membranes in the acetate form. [e]Activation energy for membranes calculated from the chloride ion conductivity. [f]Chloride ion conductivity at 80 °C. [g]Acetate ion conductivity at 80 °C. Cobalt was not characterized for chloride ion conductivity and the E$_a$ for zinc could not be determined because the chloride conductivity did not increase linearly.
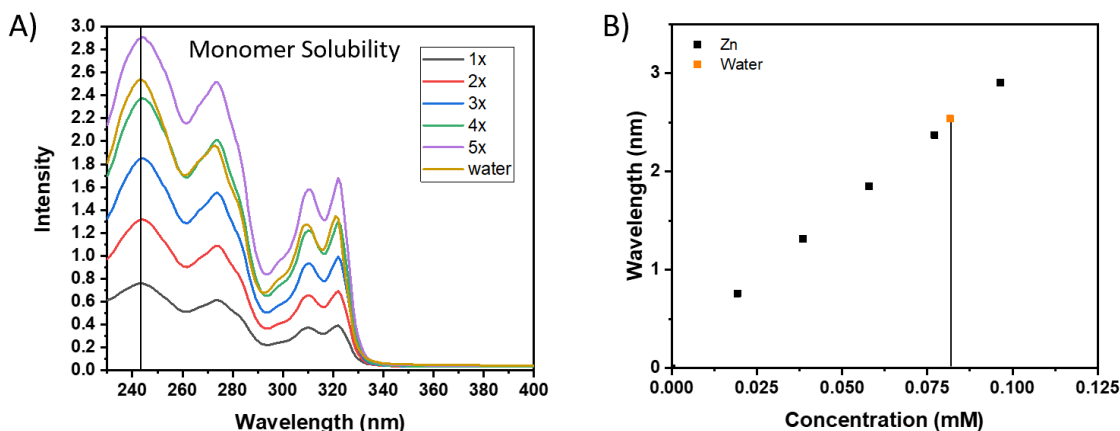
Figure 43. A) UV-vis spectra for the zinc monomer dissolved in methanol at five different concentrations as well as in a saturated aqueous solution. B) Plot of the intensity of absorbance for the peak corresponding to 243 nm against solution concentration. The other five metal cations were characterized following the same procedure, obtaining similar data.

Table 13. Monomer solubility in a saturated aqueous solution.

Metal Cation Monomer	Solubility in RO water (mM)
Fe	1.34
Ni	0.503
Ru	0.434
Co	0.455
Mn	0.019
Zn	0.082

3.3.2.1.3.2 Ion Conductivity

Similar to what was performed for nickel, ruthenium, and cobalt membranes previously, the nickel-, iron-, zinc-, and manganese-based AEMs containing the PEO crosslinker with ether linkages were characterized for their chloride ion conductivity in liquid water as a function of temperature (Figure 44). The corresponding ruthenium-based AEM from above was added to Figure 44 for comparative purposes as it had a similar chemical structure and IEC value to the membranes studied here, just ester linkages on the PEO instead of ether.[63] As expected, all samples showed increased ion conductivity at higher temperatures, due to greater water and ion mobility at elevated temperatures. More importantly, Figure 44 shows that the metal cations containing iron, nickel, ruthenium, zinc, and manganese displayed four distinct levels of chloride ion conductivity following the trend of iron > nickel > ruthenium > zinc ~ manganese. The manganese-based AEMs' low ion conductivity could be due to either the nature of the manganese-based cation or the membrane's lower IEC values as compared to the other membranes.
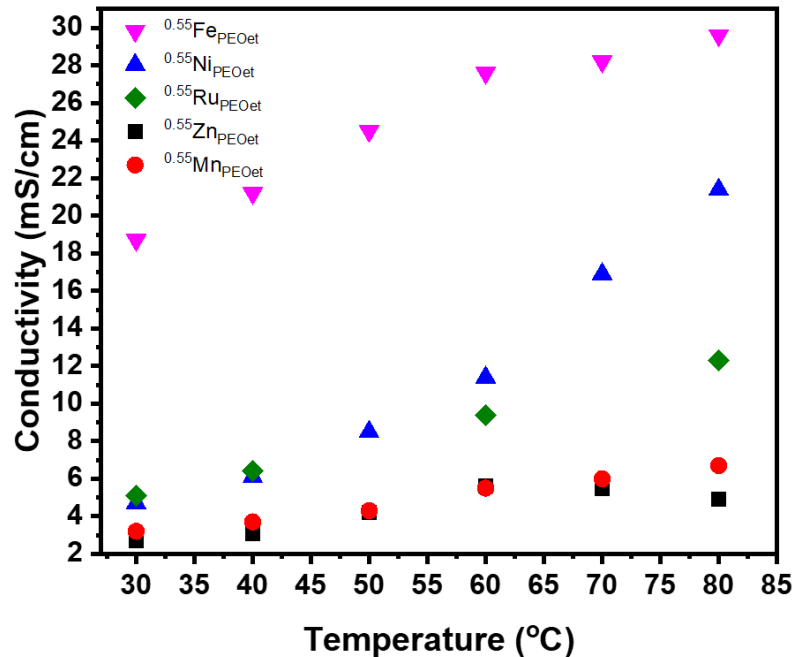
Figure 44. Chloride conductivity for iron- (magenta), nickel- (blue), ruthenium- (green), zinc- (black), and manganese- (red) based AEMs with the PEO crosslinker containing ether linkages in liquid water as a function of temperature.

Consistent with the data for the AEMs with the PEO crosslinker containing ester linkages, no strong correlations were observed between ion conductivity and bulk membrane parameters such as λ, ion concentration, and E_a of ion conductivity (Figures 45-47).[11,63] For the samples, the E_a was interesting as the iron-based sample had the highest conductivity and lowest E_a, but the nickel had the highest E_a and the second highest ion conductivity, with **$^{0.55}$Ru$_{PEOet}$** and **$^{0.55}$Mn$_{PEOet}$** samples having similar E_a values but different conductivity. That illustrates the lack of correlation for these parameters to ion conduction. Therefore, the ratio of the effective diffusion coefficient for the conducting ion (D), to the dilute solution diffusivity for the ion (D_o), termed D/D_o, was also plotted against chloride ion conductivity at 80 °C (Figure 48). The thought with D/D_o argues that as that ratio increases, the effective diffusion of the ion increases which correlates to enhance ion

conduction. However, as can be seen with [0.55]Fe[PEOet] and [0.55]Ru[PEOet], an increase in D/D$_o$ does not correlate to increased ion conduction for these samples.
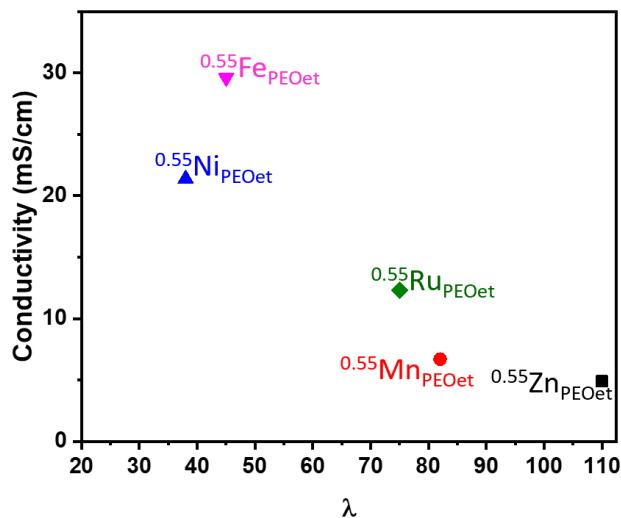
Figure 45. Chloride conductivity at 80 °C plotted versus bulk hydration number, λ, for each AEM with the PEO crosslinker containing ether linkages.
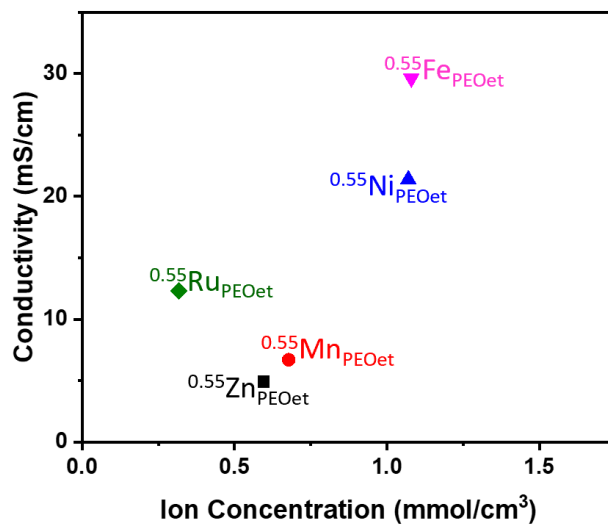
Figure 46. Chloride conductivity at 80 °C plotted versus ion concentration for each AEM with the PEO crosslinker containing ether linkages.
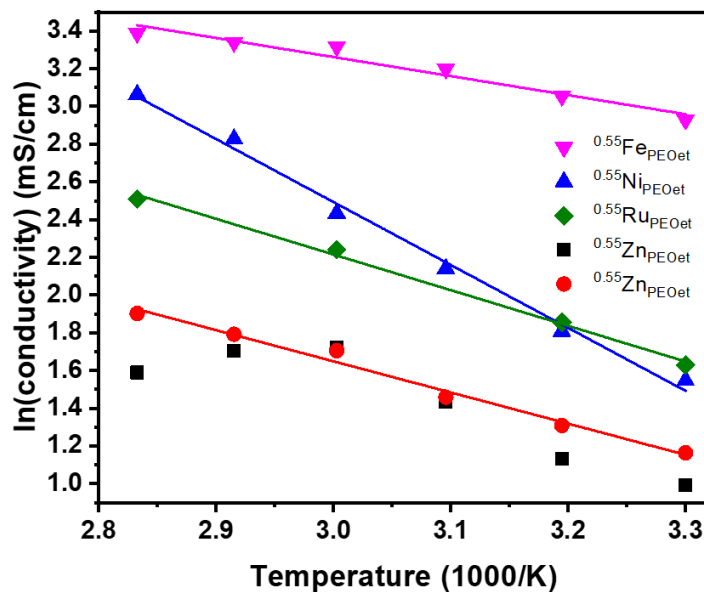
Figure 47. Chloride conductivity for the AEMs with the PEO crosslinker containing ether linkages as a function of temperature, where the E_a was calculated from the slope of the linear regression.
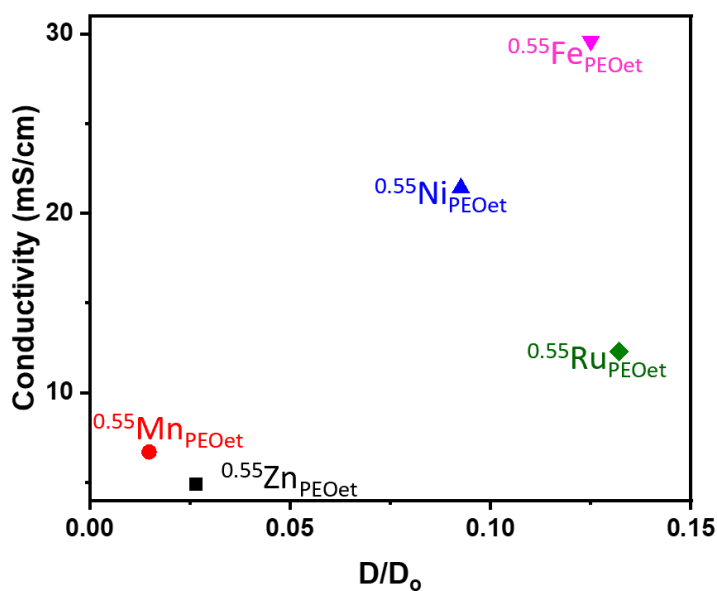
Figure 48. Chloride conductivity at 80 °C plotted versus D/D_o for each AEM with the PEO crosslinker containing ether linkages

106

3.3.2.2 Additional Ion Properties

3.3.2.2.1 Bicarbonate Ions

Given the impact the nature of the cation had on AEM ion conductivity, these metal cation, ROMP-based networks were also characterized using different counterions to explore the impact of the counterion on these materials. Three additional counterions were utilized: bicarbonate, hydroxide, and acetate. Bicarbonate and hydroxide were chosen due to the prevalence in fuel cells while acetate was chosen as one approach to improve small molecule metal cation water solubility (with further discussion of this enhanced water solubility in chapter 4).[159]

For the bicarbonate ion comparison, the water uptake was determined for AEMs containing ruthenium, nickel, and cobalt at a cationic f = 0.33 and 0.5 without a PEO crosslinker (Figure 49). Two cationic mole fractions were used to explore the impact of metal cation content on the water uptake for two different anions. Surprisingly, all three metals in the bicarbonate form facilitated similar levels of water uptake into the membrane as their chloride counterparts. This indicated that the chloride and bicarbonate ions

interacted with water in a similar fashion, producing similar water uptake into the network.
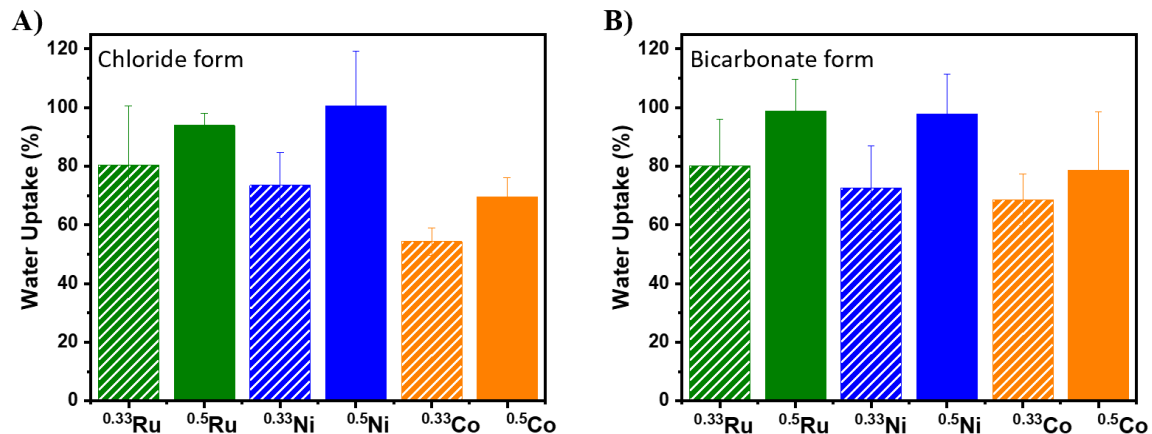
Figure 49. Water uptake values for the $^{0.33}$M and $^{0.5}$M AEMs without a PEO crosslinker in the A) chloride and B) bicarbonate form.

3.3.2.2.2 Hydroxide Ions

However, when chloride and hydroxide ions where compared, a difference was observed. For this comparison, the iron-, zinc-, and manganese-based AEMs with the PEO crosslinker containing ether linkages were used (Figure 50). At the same temperature, it can be seen that membranes in the hydroxide form demonstrated larger water uptake than membranes in the chloride form. This is most likely due to the fact that hydroxide ions interact more favorably with water molecules than chloride ions, due to the hydroxide's and water's similar structures and hydrogen-bonding capability, resulting in more absorption of water into the network.
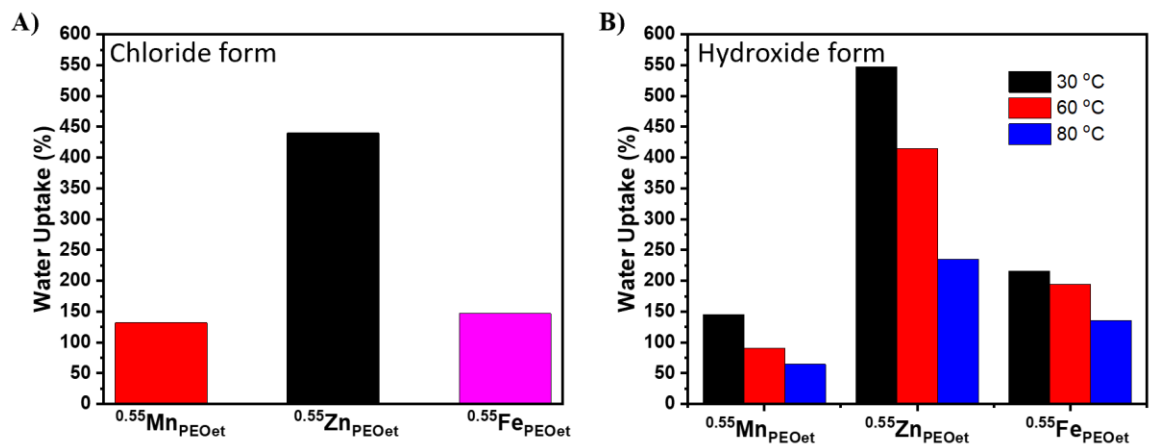
Figure 50. Water uptake values for the $^{0.55}$M$_{PEOet}$ AEMs with a PEO crosslinker containing ether linkages in the A) chloride and B) hydroxide form. Manganese-, zinc-, and iron-based AEMs were used. Water uptake was determined at 30˚C (black), 60˚C (red), and 80˚C (blue) in the hydroxide form.

Water uptake at 60 ˚C and 80 ˚C were also measured for the iron, zinc, and manganese samples in the hydroxide form to elucidate the impact of temperature on the water uptake of these metal cation-based AEMs (Figure 50). The observed decrease in water uptake as the temperature increased was most likely due to the fact that these are rubbery materials so as the temperature increases the kinetic energy of the chains also increases. The increased kinetic energy most likely results in more force on the crosslink junctions causing the membrane to shrink.

3.3.2.2.3 Acetate Ions

Finally, $^{0.55}$M$_{PEOet}$ AEMs containing iron, nickel, ruthenium, zinc, manganese, and cobalt were also characterized for the water uptake in the acetate form (Figure 51). Interestingly, the water uptake in the acetate form showed significant differences from those in the chloride form. AEMs containing iron and ruthenium demonstrated similar water uptake, AEMs containing nickel and zinc showed lower water uptake, and AEMs containing cobalt and manganese showed larger water uptake in the acetate form as

compared to their chloride form counterparts. It is not clear why these differences were observed, however it is known that acetate ions increase the water solubility of cations, which could cause drastic changes to how these metal cations interact with water and thus alter their water uptake.[159]
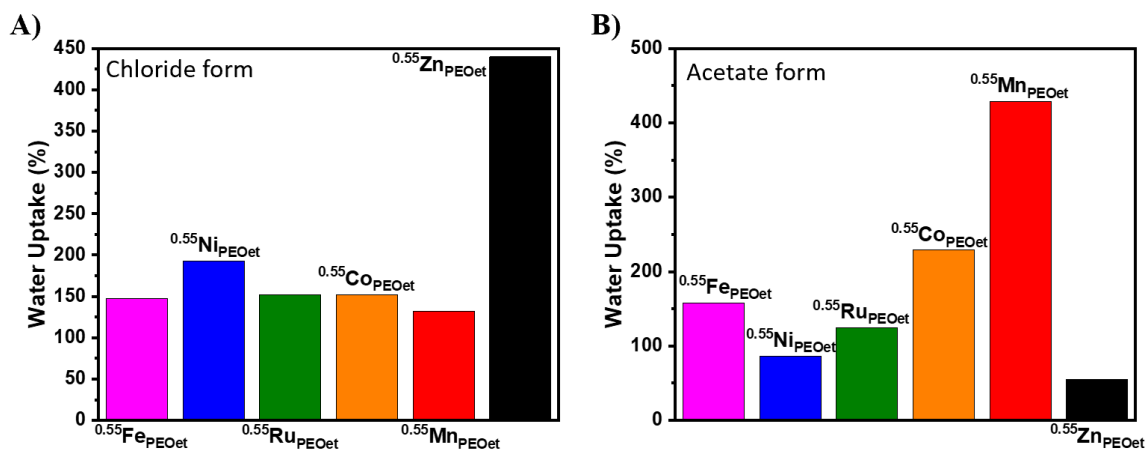
Figure 51. Water uptake values for the $^{0.55}$M$_{PEOet}$ AEMs with the PEO crosslinker containing ether linkages in the A) chloride and B) acetate form.

The membranes in the acetate form were also characterized for their acetate conductivity at 30 ˚C and 80 ˚C (Figure 52). All membranes showed reduced acetate conductivity as compared to their corresponding chloride ion conductivity, most likely due to the increased hydrated ion size, and thus decreased mobility of the acetate ions.[104,160] Not surprisingly, all membranes also showed an increase in conductivity at 80 ˚C over their conductivity at 30 ˚C. Interestingly, the trend in acetate conductivity was different from the trend in chloride conductivity, where the acetate conductivity at 80 ˚C followed a trend of nickel (10.2 mS/cm) ~ cobalt (10.2 mS/cm) > ruthenium (9.3 mS/cm) > iron (7.9 mS/cm) > zinc (6.7 mS/cm) > manganese (1.8 mS/cm).
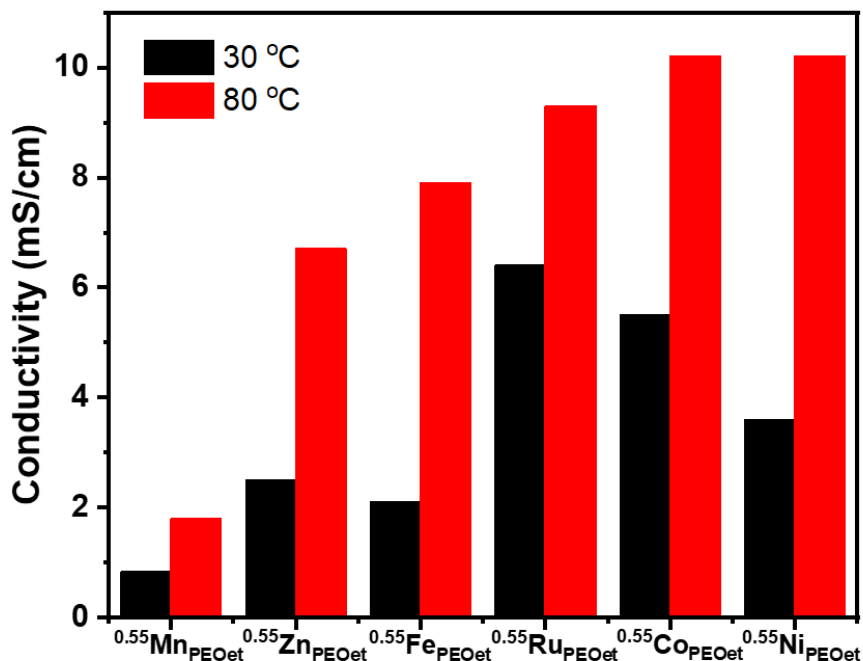
Figure 52. Acetate conductivity for manganese-, zinc-, iron-, ruthenium-, cobalt, and nickel-based AEMs with the PEO crosslinker containing ether linkages in liquid water at 30°C (black) and 80°C (red).

It was also confirmed that bulk membrane properties like λ, ion concentration, and D/D_o did not fully rationalize these trends in acetate conductivity (Figures 53-55). The E_a for these AEMs could not be determined as conductivity was only determined at two temperatures (30 °C and 80 °C). Therefore, it was not known whether the conductivity increased linearly and for Arrhenius' equation to be valid the increase must be linear. As with the chloride ion conductivity, it was not clear whether the low acetate ion conductivity observed for the manganese-based sample was a result of its low IEC or the nature of the manganese-based cation. The acetate ion conductivity data indicated that the identity of the counterion impacted the strength of the ion pair association for a cation. The impact on the association strength is exemplified with the iron cation as it facilitated the highest chloride

ion conductivity, but only facilitated an intermediate acetate ion conductivity as compared to the other metal cations.
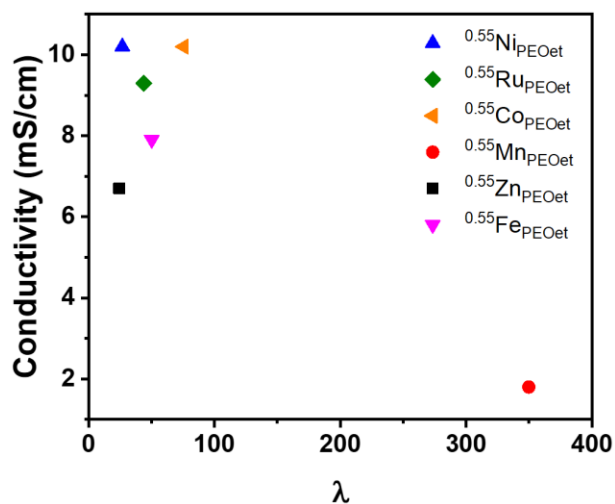
Figure 53. Acetate ion conductivity at 80°C plotted versus bulk hydration number, λ, for each AEM with the PEO crosslinker containing ether linkages.
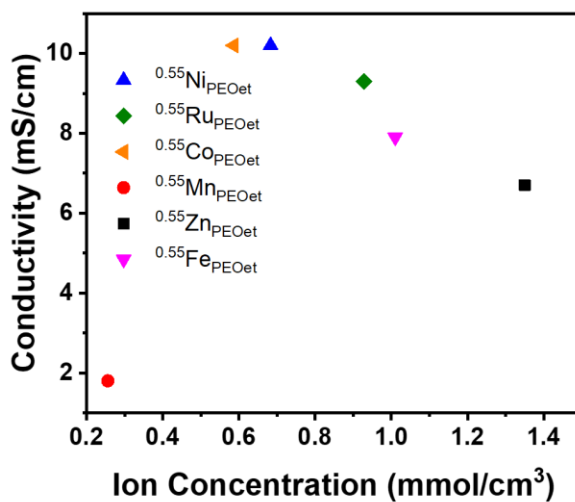
Figure 54. Acetate ion conductivity at 80°C plotted versus ion concentration for each AEM with the PEO crosslinker containing ether linkages.
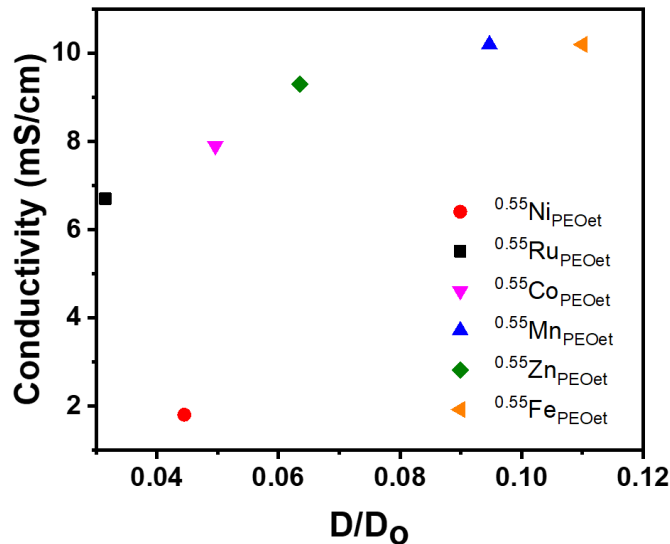
Figure 55. Acetate ion conductivity at 80°C plotted versus D/D_o for each AEM with the PEO crosslinker containing ether linkages.

3.4 Conclusions

Metal cation-based AEMs represent a promising new class of materials that can show excellent chemical stability under alkaline conditions. Two types of AEMs were characterized for their water uptake, chemical stability, mechanical properties and ion conduction: thiol-ene- and ROMP-based membranes. The thiol-ene-based AEMs demonstrated advantageous properties such as excellent chemical stability and the formation of ionic clusters. The chemical stability demonstrated the robust nature of these metal cations as well as the potential to utilize the thiol-ene reaction in AEMs as the subsequent thioether moiety showed no discernible degradation under highly alkaline conditions at elevated temperatures. Furthermore, this thiol-ene-based AEM approach demonstrated the capability of inducing microphase separation through the formation of ionic clusters for these types of membranes.

However, these thiol-ene-based AEMs also demonstrated extremely low ion conductivity, most likely a result of the ion clusters being segregated within the polymer matrix instead of forming interconnected ion-containing channels. The segregation of the ion clusters resulted in an inability of the chloride ions to easily travel through the membrane, resulting in the low ion conductivity. Furthermore, these membranes highlight another challenge facing metal cation-based AEMs: the interdependence of IEC and crosslink density. Due to the fast equilibrium kinetics of the nickel-terpyridine bond, homoleptic complexes were used, meaning each metal cation also acted as a crosslinker. Therefore, synthesizing membranes with a large IEC, needed for higher ion conduction, also resulted in extremely high crosslink density, resulting in mechanically weak membranes. The combination of low ion conduction and weak mechanical properties indicates that this thiol-ene approach is not a feasible method for synthesizing AEMs and was therefore not pursued beyond this initial report.

Alternatively, the ROMP-based AEMs proved to be an excellent model membrane to study the impact of metal cation identity on AEM ion conductivity. As the nature of the metal cation was altered with six different metal cations, the resulting AEMs showed no significant differences in their mechanical stability. All metal-based AEMs showed similar water uptake except for the zinc- and manganese-based samples, which showed elevated water uptake due to their faster terpyridine-metal bond equilibrium kinetics. The similarities in water uptake was a unique observation, and illustrated their utility as a model system, since changing the identity of the cation in an AEM traditionally results in significant changes to AEM properties, like water uptake.

Therefore, the ROMP-based AEMs were characterized for their chloride and acetate ion conductivity. This data showed that the identity of the cation influences the ion conduction, as different metal cations facilitated significantly different levels of ion conduction. Not only is the identity of the cation crucial for ion conduction, but the acetate and chloride ion conductivity also demonstrated the critical importance of the anion being conducted. From the conductivity of the two anions, it was shown that conductivity trends for a series of cations will be different for different counterions, where the best conductors with one counterion will not necessarily conduct another anion the best. This indicates that using substitutionary anion conductivity to predict hydroxide conductivity in a fuel cell may not be a fruitful approach. Furthermore, commonly studied parameters such as IEC, λ, ion concentration, D/D_o, and Ea were not sufficient to fundamentally explain the observed conductivity data. This indicated that the bulk-membrane parameters typically employed by the AEM field do not fully capture the ion conduction phenomenon, motivating the need to identify what factors or parameters have been overlooked.

CHAPTER 4

IDENTIFYING THE CATION-COUNTERION ASSOCIATION STRENGTH USING ISOTHERMAL TITRATION CALORIMETRY

4.1 Introduction

The parameters traditionally used to explain ion conduction in AEMs (λ, ion concentration, E_a, and D/D_o) failed to reliably correlate with conductivity trends for the metal cation-based AEMs. This indicates that there is a factor influencing ion conduction that has been overlooked by the AEM field. Identifying this parameter would result in a deeper understanding of AEM ion conduction, and potentially a method to reliably predict AEM performance.

This result would lead to a significant advancement in AEM research in two main ways. First, understanding and predicting factors that enhance ion conduction in an AEM will allow for the informed design of and improvements upon existing AEM technology.[25,27,161] Second, as the field attempts to improve AEM chemical stability by incorporating an increasingly wide variety of cations into AEMs, it is important to understand the effect of the cation on ion conductivity and how that understanding can be used to predict a cation's performance in an AEM.[3,15,18] The ability to predict a cation's performance in an AEM will permit the field to focus its efforts on improving the chemical stability of a smaller list of promising candidates. Here, we identify the cation-counterion association strength as a critical parameter that has been overlooked in the AEM field and show how it can be reliably assessed using isothermal titration calorimetry (ITC) to predict a cation's ability to facilitate ion conduction in AEMs.

4.2 Experimental

4.2.1 Materials

Tetrahydrofuran (Fisher Scientific) was dried over sodium under nitrogen gas (N_2) and then distilled before use. 2,2':6',2''-terpyridine, nickel(II) chloride hexahydrate, cobalt(II) chloride hexahydrate, ruthenium(III) chloride hydrate, manganese (II) chloride anhydrous, zinc chloride, iron (II) chloride tetrahydrate, iron (II) acetate, cobalt (II) acetate tetrahydrate, nickel (II) acetate tetrahydrate, manganese (II) acetate tetrahydrate, zinc acetate dihydrate, silver acetate, n-ethylmorpholine, tetra(ethylene glycol) monomethyl ether, methanol, chloroform, tetramethylammonium chloride, benzyltrimethylammonium chloride, benzyltriethylammonium chloride, benzyltributylammonium chloride, 1-ethyl-3-methylimidazolium chloride, and sodium bicarbonate were purchased from Sigma Aldrich, Alfa Aesar, Acros Organics, Fisher Scientific, or Tokyo Chemical Industry and were used as received.

4.2.2 Instrumentation

Isothermal titration calorimetry (ITC) was performed using a Malvern MicroCal Auto-ITC200.

4.2.3 Isothermal Titration Calorimetry

Isothermal titration calorimetry (ITC) was performed using a Malvern MicroCal Auto-iTC200. The calorimetric titrations were performed at atmospheric pressure and 25 °C. An aqueous solution of $NaHCO_3$ (~10 mM) was titrated into the aqueous cation solution (all with a chloride counterion concentration of 1 mM) over the course of 28 injections with a stirring speed of 750 RPM. Injection volume was 0.4 μL for the first injection, 0.5 μL for the next five injections, 1 μL for the next nine injections, and 2 μL for

the remaining 13 injections. The experiment was run using the single site binding analysis method and the first injection was removed due to probable leakage from the syringe.[162] The heat of dilution of $NaHCO_3$ into pure RO water measured by ITC and subtracted from each cation titration to ensure that $NaHCO_3$ dilution did not influence the results.

4.2.4 Bis(terpy)-metal complex synthesis.

4.2.4.1 General Procedure.

2,2':6',2''-terpyridine and the metal salt were dissolved in methanol. The solution was stirred overnight after which the solvent was removed, and the resulting powder was dried under vacuum resulting in quantitative yields. The product was used without further purification unless otherwise stated.

4.2.4.2 Ruthenium Complex in Chloride Form.

The resulting deep red powder was generated as stated above with the following amounts: 2,2':6',2''-terpyridine (0.5 g, 0.002 mol), ruthenium(III) chloride hydrated (0.255 g, 0.97 mmol), n-ethylmorpholine (0.214 mL, 1.68 mmol), and methanol (10 mL). The mixture was stirred under reflux overnight, after which the solvent was removed. The resulting solids were dissolved in RO water and washed with $CHCl_3$ three times. The RO water was removed via rotary evaporation and dried under vacuum overnight. ^1H NMR ($CDCl_3$, ppm, 500 MHz): 9.01 (4H, d), 8.75 (4H, d), 8.54 (2H, t), 8.04 (4H, td), 7.51 (4H, d), 7.31 (4H, td).

4.2.4.3 Ruthenium Complex in Acetate Form.

The non-functional, bis(terpyridine) ruthenium complex in the acetate form was synthesized by dissolving the complex in the chloride form (0.147 g, 0.23 mmol) along with silver acetate (0.077 g, 0.46 mmol)) in RO water (2.5 mL). The solution was stirred

at room temperature for 24 hours, during which a white precipitate formed. The resulting silver chloride precipitate was filtered from solution, the supernatant was concentrated, and the resulting red powder was dried under vacuum for 24 hours and used without further purification. ^{1}H NMR (MeOD, ppm, 500 MHz): 8.98 (4H, d), 8.72 (4H, d), 8.51 (2H, t), 8.01 (4H, m), 7.47 (4H, m), 7.27 (4H, m), 1.90 (6H, s).

4.2.4.4 Nickel Complex in Chloride Form.

The resulting tan powder was generated as stated above with the following amounts: 2,2':6',2''-terpyridine (0.5 g, 0.002 mol), nickel(II) chloride hexahydrated (0.237 g, 0.001 mol), and methanol (10 mL).

4.2.4.5 Nickel Complex in Acetate Form.

The nickel complex was synthesized as described above with the following amounts: terpyridine ligand (0.1 g, 0.43 mmol), nickel (II) acetate tetrahydrate (0.053 g, 0.21 mmol), DCM (2.5 mL) and methanol (2.5 mL). ESI-MS m/z 262.0991 (M^{2+}, 262.06).

4.2.4.6 Cobalt Complex in Chloride Form.

The resulting brown/red powder was generated as stated above with the following amounts: 2,2':6',2''-terpyridine (0.5 g, 0.002 mol), cobalt(II) chloride hexahydrated (0.237 g, 0.001 mol), and methanol (10 mL).

4.2.4.7 Cobalt Complex in Acetate Form.

The cobalt complex was synthesized as described above with the following amounts: terpyridine ligand (0.1 g, 0.43 mmol), cobalt (II) acetate tetrahyrdate (0.053 g, 0.21 mmol), DCM (2.5 mL) and methanol (2.5 mL). ESI-MS m/z 262.5977 (M^{2+}, 262.56).

4.2.4.8 Iron Complex in Chloride Form.

The iron complex was synthesized as described above with the following amounts: terpyridine ligand (0.5 g, 2.1 mmol), iron (II) chloride tetrahydrate (0.213 g, 1.07 mmol), DCM (5 mL) and methanol (5 mL). ^{1}H NMR (MeOD, ppm, 500 MHz): 9.02 (4H, d), 8.66 (2H, t), 8.58 (4H, d), 7.87 (4H, m), 7.08 (8H, m). ^{13}C NMR (MeOD, ppm, 500 MHz): 160.33, 158.00, 152.51, 138.75, 138.18, 127.39, 123.73, 123.59. ESI-MS m/z 216.1198 (M^{2+}, calculated 261.07).

4.2.4.9 Iron Complex in Acetate Form.

The iron complex was synthesized as described above with the following amounts: terpyridine ligand (0.1 g, 0.43 mmol), iron (II) acetate (0.037 g, 0.21 mmol), DCM (2.5 mL) and methanol (2.5 mL). ^{1}H NMR (MeOD, ppm, 500 MHz): 9.13 (4H, d), 8.78 (2H, t), 8.69 (4H, d), 7.97 (4H, m), 7.18 (8H, m), 1.91 (6H, s). ESI-MS m/z 261.1027 (M^{2+}, calculated 261.07).

4.2.4.10 Manganese Complex in Chloride Form.

The manganese complex was synthesized by dissolving terpyridine ligand (0.5 g, 2.1 mmol) and manganese (II) chloride (0.135 g, 1.07 mmol) in ethanol (10 mL) and heating at 90 °C overnight, after which the solvent was removed and the resulting powder was dried under vacuum. ESI-MS m/z 260.6281 (M^{2+}, calculated 260.57).

4.2.4.11 Manganese Complex in Acetate Form.

The manganese complex was synthesized by dissolving terpyridine ligand (0.1 g, 0.43 mmol) and manganese (II) acetate tetrahydrate (0.053 g, 0.21 mmol) in ethanol (5 mL) at 90 °C and stirring overnight. In the morning the solvent was removed and the resulting

powder was dried under vacuum. ESI-MS m/z tpyMn+OAc 347.0907 (M^{1+}, calculated 347.05).

4.2.4.12 Zinc Complex in Chloride Form.

The zinc complex was synthesized as described above with the following amounts: terpyridine ligand (0.5 g, 2.1 mmol), zinc (II) chloride (0.146 g, 1.07 mmol), and DCM (5 mL) methanol (5 mL). ESI-MS m/z 265.1189 (M^{2+}, calculated 265.06).

4.2.4.13 Zinc Complex in Acetate Form.

The zinc complex was synthesized as described above with the following amounts: terpyridine ligand (0.1 g, 0.43 mmol), zinc (II) acetate dihydrate (0.047 g, 0.21 mmol), DCM (2.5 mL) and methanol (2.5 mL). ESI-MS m/z 265.0975 (M^{2+}, calculated 265.06).

4.2.4.14 TEO Functionalized Terpyridine.

To a 100 mL round bottom flask equipped with a stir bar, potassium hydroxide (1.2 g, 0.021 mol), tetra(ethylene glycol) monomethyl ether (1.5 mL, 0.0075 mol), and DMSO (30 mL) were added. The mixture was stirred at 50 ˚C for 30 minutes after which 4-chloro-2,2':6',2''-terpyridine (1 g, 0.0037 mol) was added as a powder. The solution was stirred at 50 ˚C overnight. The reaction mixture was then diluted with RO water (150 mL) and the organic phase was extracted with diethyl ether three times. The organic phase was then dried with sodium sulfate, filtered and the remaining solvent was removed. After drying under vacuum, the product was obtained as a clear oil (yield 1.62 g, >95%). ^{1}H NMR (MeOD, ppm, 500 MHz): 8.67 (2H, m), 8.61 (2H, m), 7.99 (4H, m), 7.48 (2H, m), 4.42 (2H, m), 3.96 (2H, m), 3.76 (2H, m), 3.69 (2H, m), 3.65 (2H, m), 3.61 (4H, m), 3.50 (2H, m), 3.33 (3H, br). ^{13}C NMR (MeOD, ppm, 500 MHz): 167.20, 157.01, 155.77, 148.65,

137.27, 124.07, 121.53, 107.12, 71.53, 70.48, 70.23, 70.21, 70.13, 69.93, 69.12, 67.65, 57.65. ESI-MS m/z 462.2818 (M^{1+} + Na^+, 439.21).

4.2.4.15 TEO Functionalized Metal Complex General Procedure.

The PEO functionalized terpyridine ligand was dissolved in DCM and mixed with a solution of metal chloride salt dissolved in methanol. The mixture was then stirred overnight at room temperature after which the solvent was removed. The resulting powder was dried under vacuum to produce the desired metal complex.

4.2.4.16 TEO-Ni.

The nickel complex was synthesized as described above with the following amounts: TEO terpyridine ligand (0.25 g, 0.57 mmol), nickel (II) chloride hexahydrate (0.068 g, 0.28 mmol), DCM (5 mL), and methanol (5 mL) resulting in a tan powder. ESI-MS m/z 468.2349 (M^{2+}, 468.18).

4.2.4.17 TEO-Co.

The cobalt complex was synthesized as described above with the following amounts: TEO terpyridine ligand (0.25 g, 0.57 mmol), cobalt (II) chloride hexahydrate (0.068 g, 0.28 mmol), DCM (5 mL), and methanol (5 mL) resulting in a red/brown powder. ESI-MS m/z 468.7568 (M^{2+}, 468.68).

4.2.4.18 TEO-Fe.

The iron complex was synthesized as described above with the following amounts: TEO terpyridine ligand (0.25 g, 0.57 mmol), iron (II) chloride tetrahydrate (0.057 g, 0.28 mmol), DCM (5 mL), and methanol (5 mL) resulting in a purple powder. ^{1}H NMR (MeOD, ppm, 500 MHz): 8.79 (4H, s), 8.67 (4H, d), 7.96 (4H, m), 7.29 (4H, d), 7.19 (4H, m), 4.85 (4H, m), 4.18 (4H, m), 3.88 (4H, m), 3.79 (4H, m), 3.72, (4H, m), 3.65 (8H, m), 3.56 (4H, m),

3.34 (3H, s). ^{13}C NMR (MeOD, ppm, 500 MHz): 168.38, 160.85, 158.30, 152.84, 138.43, 127.19, 123.54, 111.36, 71.58, 70.54, 70.31, 70.19, 69.97, 69.75, 69.21, 57.68. ESI-MS m/z 467.2424 (M^{2+}, 467.18).

4.2.4.19 TEO-Mn.

The nickel complex was synthesized as described above with the following amounts: TEO terpyridine ligand (0.25 g, 0.57 mmol), manganese (II) chloride (0.036 g, 0.28 mmol), and ethanol (10 mL) resulting in a tan powder. ESI-MS m/z 466.7533 (M^{2+}, 466.68).

4.2.4.20 TEO-Zn.

The nickel complex was synthesized as described above with the following amounts: TEO terpyridine ligand (0.25 g, 0.57 mmol), zinc (II) chloride (0.039 g, 0.28 mmol), DCM (5 mL), and methanol (5 mL) resulting in a tan powder. ^{1}H NMR (MeOD, ppm, 500 MHz): 8.78 (4H, d), 8.51 (4H, br), 8.21 (4H, t), 7.89 (4H, br), 7.49 (4H, m), 4.78 (4H, br), 4.10 (4H, br), 3.83 (4H, m), 3.75 (4H, m), 3.69 (4H, m), 3.64 (8H, m), 3.55 (4H, m), 3.34 (3H, s). ^{13}C NMR (MeOD, ppm, 500 MHz): 171.82, 151.06, 148.10, 147.37, 141.10, 127.40, 122.91, 110.02, 71.57, 70.49, 70.27, 70.18, 70.16, 69.96, 69.79, 69.09, 57.68. ESI-MS m/z 471.2480 (M^{2+}, 471.18).

4.3 Results and Discussion

4.3.1 ITC in Chloride Form

Since the metrics traditionally used to explain ion conduction in AEMs failed to fully capture the ion conductivity trends observed for these metal cation-based AEMs, the thermodynamics of counterion conduction was characterized for the different cations.[158] Counterion release for conduction depends on the strength of the cation-counterion association, with a weaker association increasing the free ion concentration and ion

conductivity.[27] Therefore, the association strength between each metal cation and its corresponding chloride counterion was examined with a counterion exchange experiment using isothermal titration calorimetry (ITC) to determine if the thermodynamics of counterion exchange could account for the trends in conductivity. ITC is used for measuring the heat exchange upon binding between two species.[163,164]

However, since ITC required the analyte to be soluble in an aqueous medium, neither the AEMs nor the metal complex monomers could be characterized. Therefore, model, analogous small molecule bis(terpyridine) metal complexes were synthesized from non-functional terpyridine, **bis(terpy)Ni**, **bis(terpy)Ru**, **bis(terpy)Co**, **bis(terpy)Fe bis(terpy)Mn**, and **bis(terpy)Zn**, as shown in Figure 56, to isolate the metal center's effect on the strength of the cation-counterion pair. **Bis(terpy)Ru** was also confirmed to not contain the n-ethylmorpholinium salt by ^{1}H NMR (Figure 57). However, the zinc- and manganese-based cations in the chloride form could not be characterized in the ITC due to their water insolubility. The association strength was quantified by measuring the enthalpic response of breaking the initial ion pair between the metal cation and its chloride counterions by adding bicarbonate counterions to form new ion pairs.
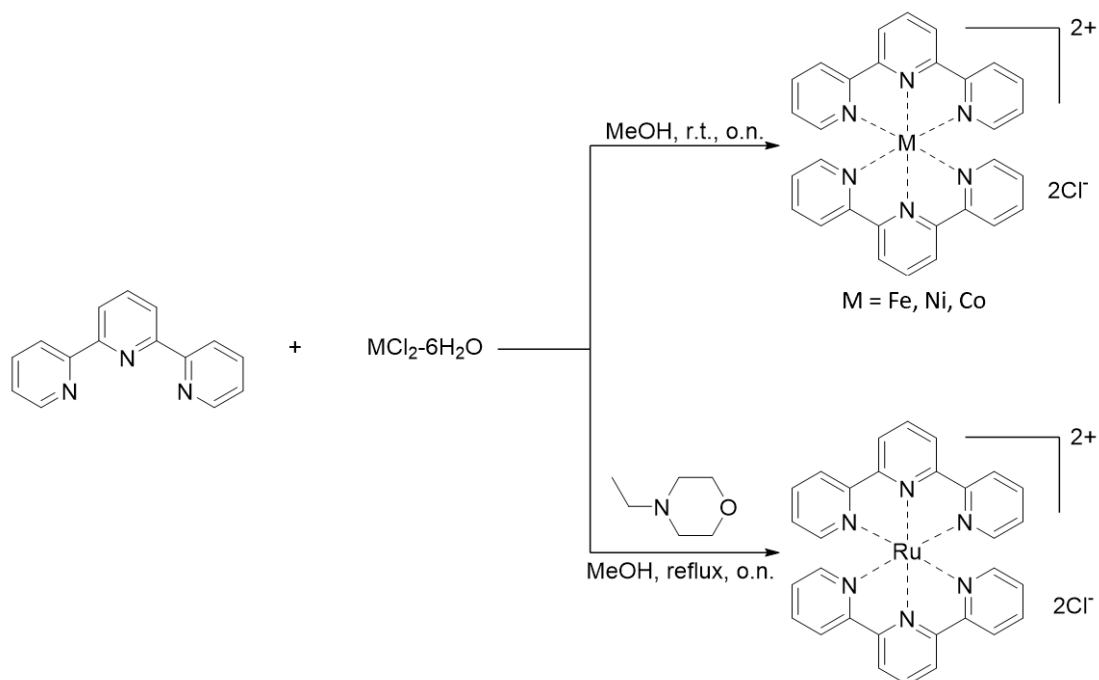
Figure 56. Synthetic scheme for model bis(terpyridine) metal complexes in the chloride form for use in ITC experiments.
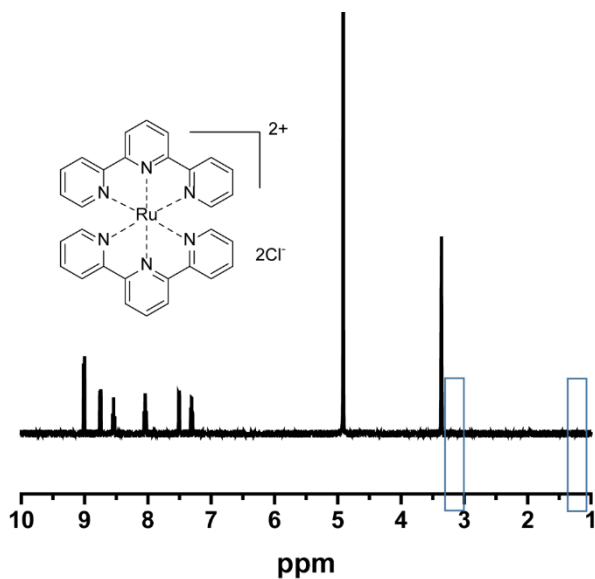
Figure 57. ^{1}H NMR (500 MHz) spectra of **bis(terpy)Ru** in methanol-d$_4$ confirming the absence of the N-ethylmorpholinium chloride salt due to a lack of peaks at 1.35 and 3.2 ppm, indicated by the boxes.

To probe the thermodynamics of the cation-counterion association, the metal complexes in the chloride form were dissolved in RO water then titrated with an aqueous sodium bicarbonate solution from zero to two molar equivalents of bicarbonate to chloride counterion. As the solutions were titrated, the heat of counterion exchange was monitored (Figures 58A) and the change in enthalpy for each injection (calculated as the area under the heat absorption spike) was plotted against the molar ratio of $NaHCO_3$ to initial chloride counterion as a binding curve (Figure 58B). All titrations were compared to a control monitoring the heat of dilution of the $NaHCO_3$ into pure RO water, where the curves in Figure 58 are corrected for this heat of dilution. The peaks in Figure 58A became larger after injections 6 and 15 since a larger volume of $NaHCO_3$ was injected after those points, but the overall ΔH for the reaction continued to decrease as shown in Figure 58B. Traditionally, the binding curve obtained would be fit to determine a binding constant, however, the nickel and iron complex did not produce curves that could be fit, as they were too noisy, most likely due to the low amount of heat exchanged.[165,166] Therefore, the total change in enthalpy, ΔH_{tot}, for all four titrations was calculated by summing each data point in the plot (Table 14), as each data point represents the ΔH for a single injection.[63,167] Interestingly, the spontaneous exchange (negative ΔG) for all metal complexes was endothermic, with positive ΔH_{tot} values, indicating that a positive change in entropy, ΔS, drove the reaction (equation 11).

$$\Delta G = \Delta H - T\Delta S \qquad \qquad (11)$$

The change in entropy should be similar for all four reactions since the same number of principle molecules were involved in each exchange and the same exchange occurred for each titration. In addition, all experiments were run at the same temperature,

126

25 °C. Therefore, differences in the measured ΔH_{tot} could be correlated to differences in the overall change in energy, ΔG, of the reaction, using equation 11. For the exchange, **bis(terpy)Fe** had a ΔH_{tot} of 361 cal/mol HCO_3^-, about half as large as **bis(terpy)Ni** at 586 cal/mol HCO_3^-, which was about half as large as **bis(terpy)Ru** and **bis(terpy)Co**, at 1003 cal/mol HCO_3^- and 1120 cal/mol HCO_3^-, respectively.
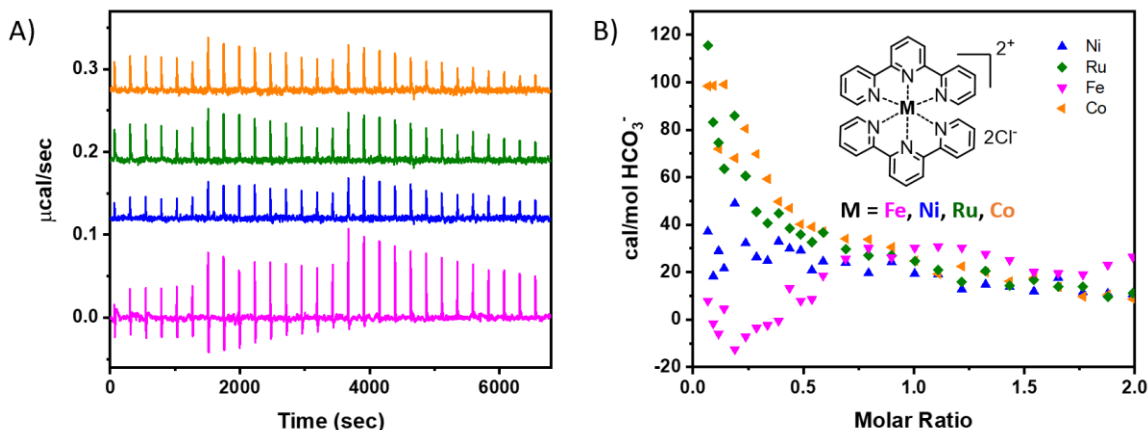
Figure 58. Counterion exchange from chloride to bicarbonate ion in MilliQ water at 25 °C plotted using ITC for various terpyridine-metal complexes. A) Raw ITC data for each metal complex stacked on the y-axis for clarity, average of two trials, which has been corrected for the heat of dilution of the NaHCO3 solution into water and B) Integration data plotted as a binding curve showing the decrease in the change in enthalpy for each injection as the molar ratio of NaHCO3 increased. Complexes contained either iron (magenta), nickel (blue), ruthenium (green), or cobalt (orange).

Since the iron complex had a smaller ΔH_{tot}, but likely a similar $T\Delta S$ term, the ΔG of counterion exchange for the iron complex was more negative than for the other metals, which suggested that there was more of a thermodynamic driving force for chloride ion release, a parameter that has previously been difficult to measure for AEMs and PEMs. Additionally, the lower ΔH_{tot} indicated that less energy needed to be absorbed by the iron system to facilitate counterion exchange, strongly suggesting that iron had weaker initial binding to its chloride counterions. Weaker initial counterion binding and a stronger

thermodynamic driving force for counterion release should increase the number of free ions and increase the AEM's conductivity.[27] Given that ion release is critical to any conductivity mechanism, and that the percentage of free ions is directly correlated to conductivity, this thermodynamic driving force for ion release appears to be the prevailing factor for the iron-based AEM's superior ion conductivity.[27,168]

Table 14. Summary of the ITC data for each bis(terpyridine) metal complex showing the total change in enthalpy for each counterion exchange reaction.

Sample	ΔH_{tot} (cal/mol HCO_3^-)		
	$Cl^- \rightarrow HCO_3^-$ [a]	$OAc^- \rightarrow HCO_3^-$ [b]	$Cl^- \rightarrow HCO_3^-$ (TEO functionalized)[c]
Ru	$1{,}003 \pm 48$	233 ± 41	-
Ni	586 ± 41	402 ± 29	654 ± 147
Co	$1{,}120 \pm 42$	637 ± 21	805 ± 151
Fe	361 ± 54	653 ± 22	709 ± 41
Zn	-	$1{,}185 \pm 55$	869 ± 59
Mn	-	$2{,}588 \pm 79$	$1{,}040 \pm 49$

[a]Counterion exchange reaction for metal complexes in the chloride form to the bicarbonate form. [b]Counterion exchange reaction for metal complexes in the acetate form to the bicarbonate form. [c]Counterion exchange reaction for tetra(ethylene oxide) (TEO) functionalized metal complexes in the chloride form to the bicarbonate form.

Interestingly, the enthalpy of ion exchange measured by ITC indicates the cation-counterion association strength and correlates well with the conductivity of an AEM. This cation-counterion association strength appears to give insight into these materials that other measurements of membrane properties do not. Figure 59 illustrates the linear correlation between the chloride conductivity at 80 ˚C for a metal cation in an AEM and the ΔH_{tot} values from ITC that relate to the cation-counterion association strength. The cobalt-based sample is not shown since it could not be characterized for its AEM chloride ion conductivity. The ΔH_{tot} values decrease as the cation-counterion association weakens, due to an increase in the ion hydration of the ion pair (discussed in detail below), which leads to enhanced chloride ion conductivity (Figure 59).[169,170] This observed correlation validates

the utility of ITC to characterize the association strength between cations and their chloride counterions in order to understand ion conductivity in these materials.
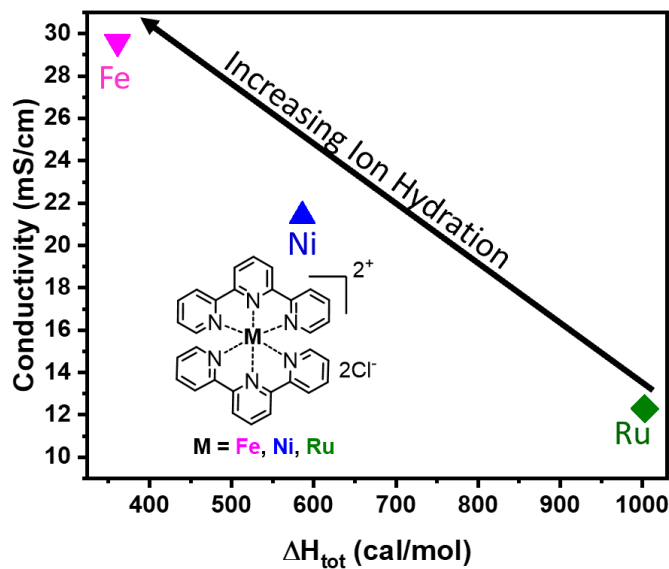
Figure 59. Plot of chloride conductivity versus ΔH_{tot} for iron (magenta), nickel (blue), and ruthenium (green) showing the linear correlation between the two properties.

4.3.2 ITC in Acetate Form

In order to verify the impact of the counterion, ITC of analogous small molecule metal cations in the acetate form were synthesized for iron, nickel, zinc, manganese, and cobalt cations following a similar procedure as for the cations in the chloride form (Figure 60). The ruthenium-based cation was synthesized in a two-step process, first by forming the cation in the chloride form and then converting it to the acetate form (Figure 61), with complete conversion being confirmed by both ^{35}Cl and ^{1}H NMR (Figure 62 and 63). Acetate counterions where chosen for their known ability to increase the water solubility of cations.[159]
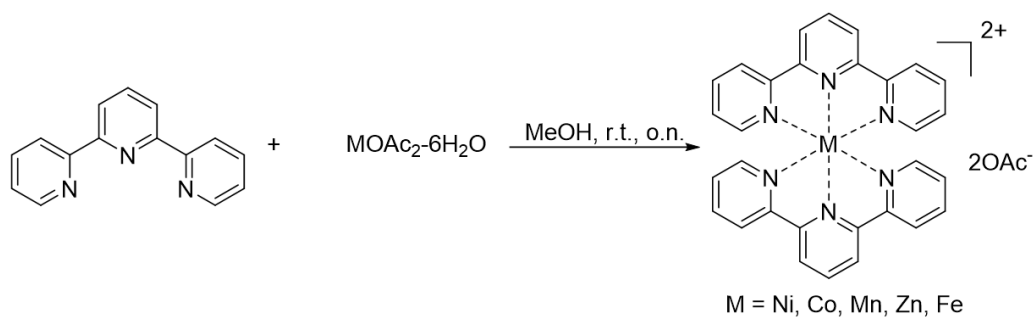
Figure 60. Synthetic scheme for model bis(terpyridine) metal complexes with acetate counterions for use in ITC experiments.

Figure 61. Synthetic scheme for conversion of the ruthenium complex from the chloride form to the acetate form.
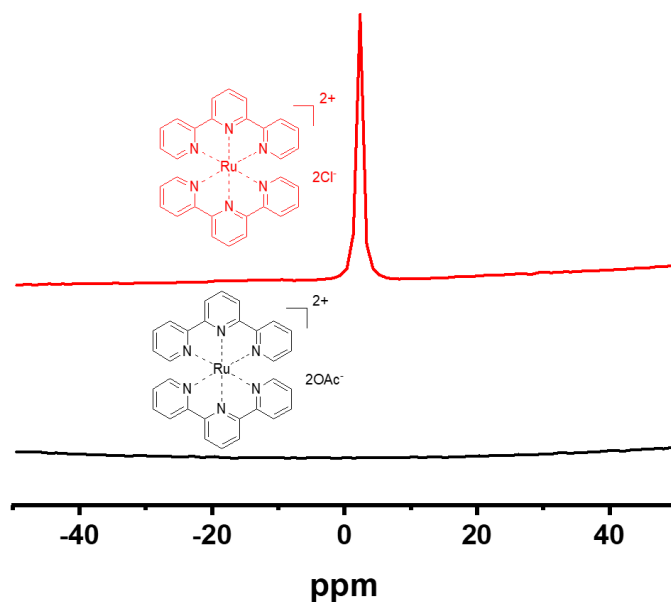
Figure 62. ^{35}Cl NMR of the ruthenium complex in the chloride form (red) and acetate form (black) showing complete loss of the chloride counterions.
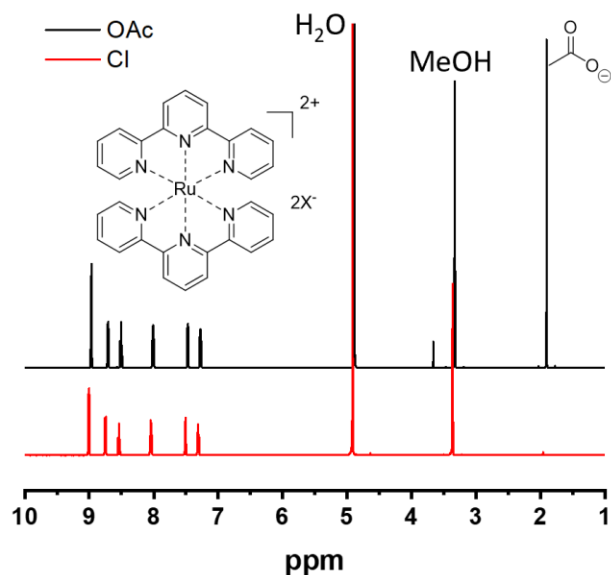
Figure 63. ^{1}H NMR of the ruthenium complex in the chloride form (red) and acetate form (black) showing the appearance of a peak corresponding to the acetate counterions.

Once the metal cations were in the acetate form, the same ITC titration method was used to perform a counterion exchange for these cations from the acetate to bicarbonate form (Figure 64). The ΔH_{tot} was calculated for each metal cation by summing each data point from the curve (Table 14). Similar to the acetate conductivity, the trend in ΔH_{tot} for the cations in the acetate form was also different from the trend observed for those in the chloride form. The ΔH_{tot} of the cations in the acetate form followed the trend of ruthenium (233 cal/mol) < nickel (402 cal/mol) < cobalt (637 cal/mol) ~ iron (653 cal/mol) < zinc (1,185 cal/mol) < manganese (2,588 cal/mol). The differences observed for the cations in the acetate form as compared to those in the chloride form further indicate differences in the ion association strength for different counterions.
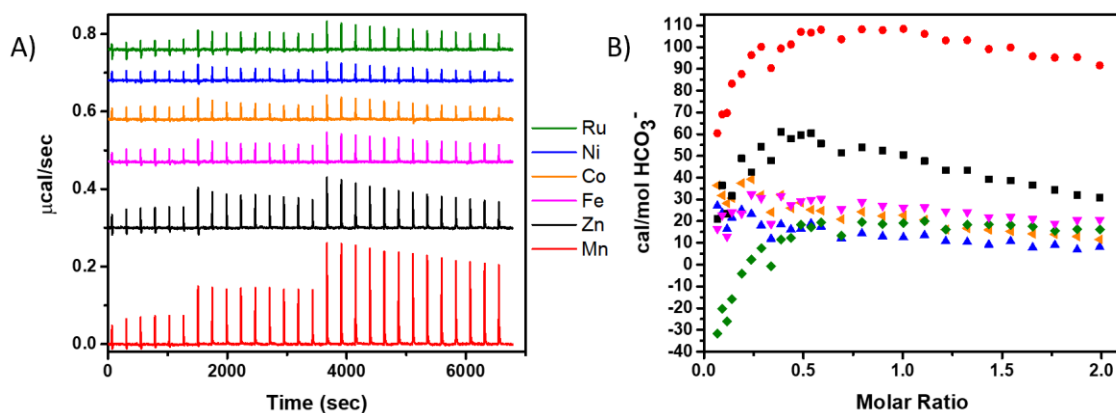
Figure 64. Counterion exchange from acetate to bicarbonate ion in Milli-Q water at 25 °C plotted using ITC for various terpyridine-metal complexes. A) Raw ITC data, average of three trials, which has been corrected for the heat of dilution of $NaHCO_3$ into water. B) Integration data plotted showing the change in enthalpy for each injection as the molar ratio of NaHCO3 increased. Complexes contained either ruthenium (green), nickel (blue), cobalt (orange), iron (magenta), zinc (black), or manganese (red).

To determine whether the cation-counterion association strength for cations in the acetate form determined by ITC can be used to reliably understand their ion conductivity, the ΔH_{tot} for each cation was plotted against the acetate conductivity at 80 ˚C for the AEM containing the corresponding metal cation (Figure 65). Similar to the chloride ions, there appears to be a linear correlation between the ΔH_{tot} and the conductivity values for acetate ions as well. This data indicates that the low ion conduction observed for the manganese-based membrane appears to be dominated by a stronger ion pair association for the manganese cation, seen through a large ΔH_{tot} value, as opposed to the low IEC value. This ΔH_{tot} data demonstrates that the ITC method is a robust approach for determining the association strength between the cation and its counterion, through determination of a ΔH_{tot} value, and that it can be used to generally predict how well a cation will conduct its counterion in an AEM for more than just chloride ions.
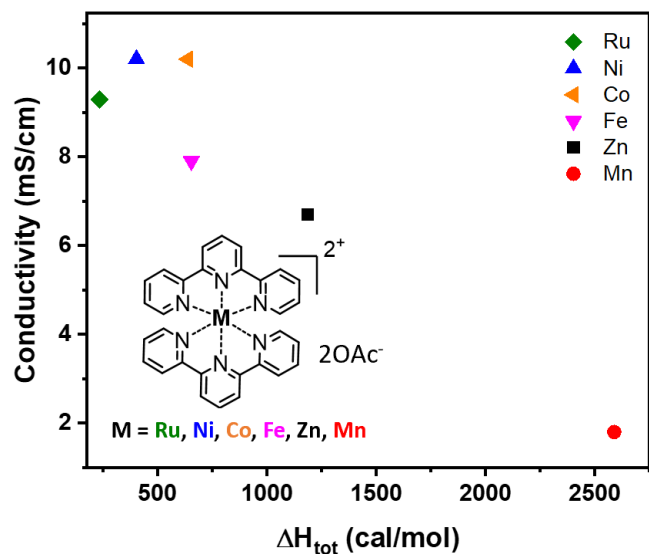
Figure 65. Plot of acetate conductivity versus ΔH_{tot} for ruthenium (green), nickel (blue), cobalt (orange), iron (magenta), zinc (black), and manganese (red) showing the correlation between the two properties for cations in the acetate form.

4.3.3 ITC of TEO-Functionalized Cations

As demonstrated with the small molecule zinc and manganese cations in the chloride form, not all cations are soluble in water, which limits the number of cations that can be characterized using this ITC method. Therefore, functionalizing cations to improve their water solubility was used to widen the scope of this characterization technique. Functionalization of the cations was accomplished by synthesizing small molecule metal cations in the chloride form that were functionalized with short tetra(ethylene oxide) (TEO) groups containing either nickel, cobalt, iron, zinc, or manganese, with the TEO groups improving water solubility of the cations (Figure 66).
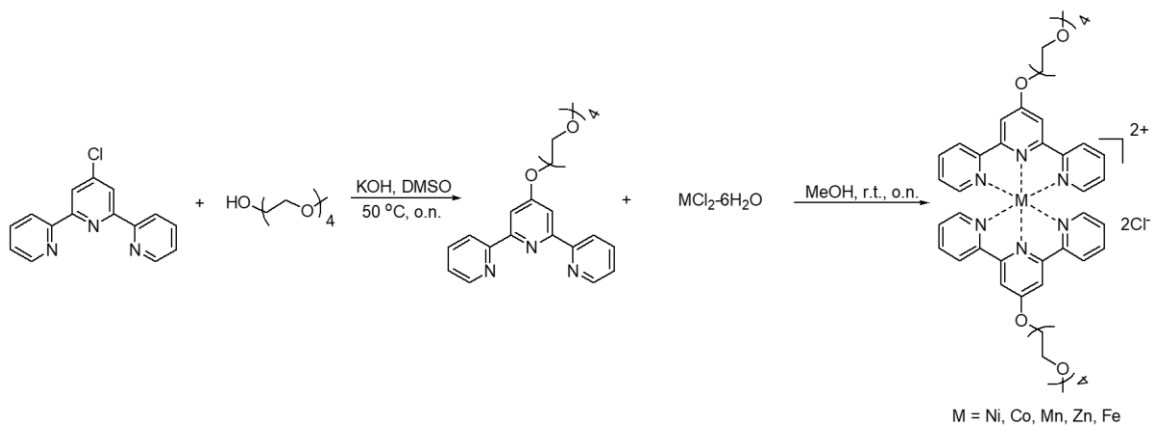
Figure 66. Synthetic scheme for TEO functionalized bis(terpyridine) metal complexes with chloride counterions for use in ITC experiments.

The functionalized cations in the chloride form were then characterized using the same ITC method that was used for the non-functionalized metal cations in the chloride and acetate forms (Figure 67). The counterion exchange measured by the ITC produced an enthalpic response that was similar for all cations, within error, regardless of the metal center (Figure 67 and Table 14). These similarities were surprising since it has already been established that changing the metal center has a strong impact on the enthalpic response to counterion exchange due to differences in the cation-counterion association strength.
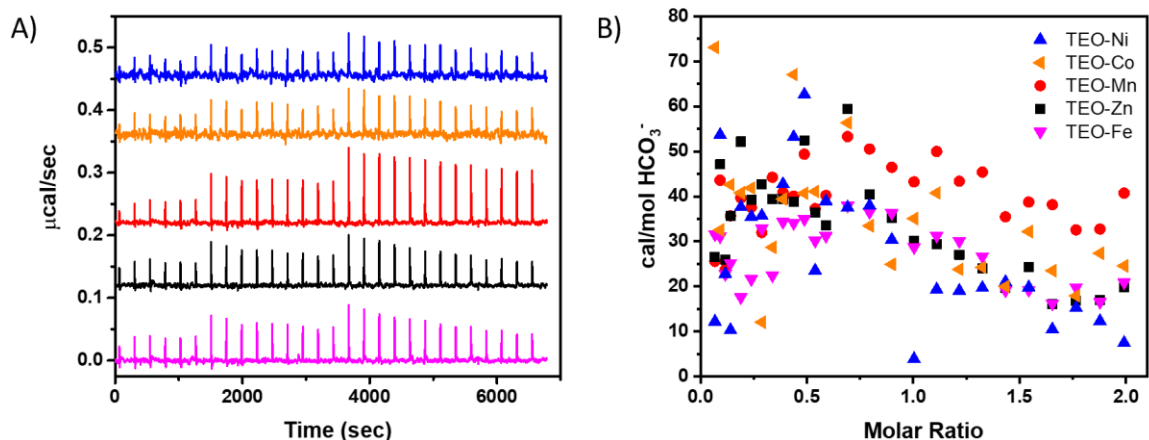
Figure 67. Counterion exchange from chloride to bicarbonate ions in Milli-Q water at 25 °C plotted using ITC for various TEO-functionalized terpyridine-metal complexes. A) Raw ITC data, average of three trials, which has been corrected for the heat of dilution of $NaHCO_3$ into water. B) Integration data plotted showing the change in enthalpy for each injection as the molar ratio of $NaHCO_3$ increased. Complexes contained either nickel (blue), cobalt (orange), manganese (red), zinc (black), or iron (magenta).

The fact that all TEO-functionalized metal cations produced a similar enthalpic response, despite the knowledge that they bind their counterions with different affinities, indicated that the TEO functional groups dominated the enthalpic response in the ITC. It has been shown previously that the ion hydration plays a key role in how strongly bound an anion is to its cation and that entropic changes in the number of water molecules involved in the ion hydration is the driving force for this counterion exchange reaction.[63,171] Therefore, it appears that the TEO groups attached to the cations dominate both of these factors. It is possible that the TEO chains influence the location of water around the molecules, thus impacting the change in water during the counterion exchange reaction and dominating the enthalpic response in the ITC. Furthermore, it is also likely that the TEO groups interact with and stabilize the metal cations, further impacting the ion hydration and thus the ion pair association strength for these functional cations. Since the water's interaction with the cations was dominated by the TEO chains, and all the functional

135

cations had the same TEO chains, this would explain the similar ΔH_{tot} values obtained for all metal cations from the ITC experiment. The impact of the TEO groups shows that while this ITC method appears to be a strong approach for characterizing cations, the functional groups attached to the cation can have significant impact on the ΔH_{tot} values.

4.3.4 ITC of Nitrogen-Based Cations

Characterizing the thermodynamic driving force for counterion release in metal cations led to a quantitative understanding of conductivity trends in the corresponding AEMs. Therefore, the same technique was used to study more traditional nitrogen-based cations in order to investigate the general applicability of ITC towards a wider range of cations. Consequently, five nitrogen-based cations, tetramethylammonium (**TMA**), benzyltrimethylammonium (**BMeA**), benzyltriethylammonium (**BEtA**), benzyltributylammonium (**BBuA**), and 1-ethyl-3-methylimidazolium (**EMI**), were studied using ITC (Figures 68-70). All five nitrogen-based cations were characterized following the same procedure used for the metal cations. The heat of counterion exchange was monitored in Figures 68A and 69A, with the change in enthalpy for each injection plotted against the molar ratio in Figures 68B and 69B. Interestingly, the titration of the nitrogen-based cations produced curves similar to the **bis(terpy)Fe** titration curve, suggesting that both types of cations had similar counterion exchange behavior. The ΔH_{tot} was again calculated and Figure 70 shows that the nitrogen-based cations were also overall endothermic reactions, yet still spontaneous, meaning that entropy dominated their counterion exchange as well. All nitrogen-based cations demonstrated low ΔH_{tot} values, where **BEtA**, **BMeA**, and **BBuA** had similar ΔH_{tot} of 207, 212, and 287 cal/mol HCO_3^-,

respectively, which were lower than **TMA** (ΔH_{tot} of 350 cal/mol HCO$_3^-$), and **EMI** (ΔH_{tot} of 481 cal/mol HCO$_3^-$).
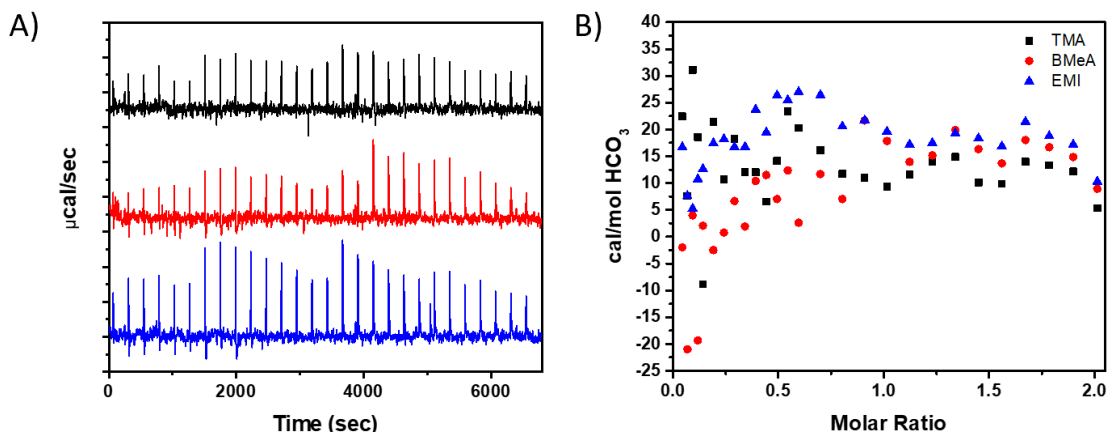
Figure 68. Counterion exchange curves for nitrogen-based cations TMA (black), BMeA (red), and EMI (blue). A) Raw ITC data for each cation shifted for clarity, average of three trials, which has been corrected for the heat of dilution of the NaHCO$_3$ solution into water and B) Integration data plotted as a binding curve showing the decrease in the change in enthalpy for each injection as the molar ratio of NaHCO3 increased. Samples were run in MilliQ water at 25°C exchanging chloride counterions for bicarbonate.
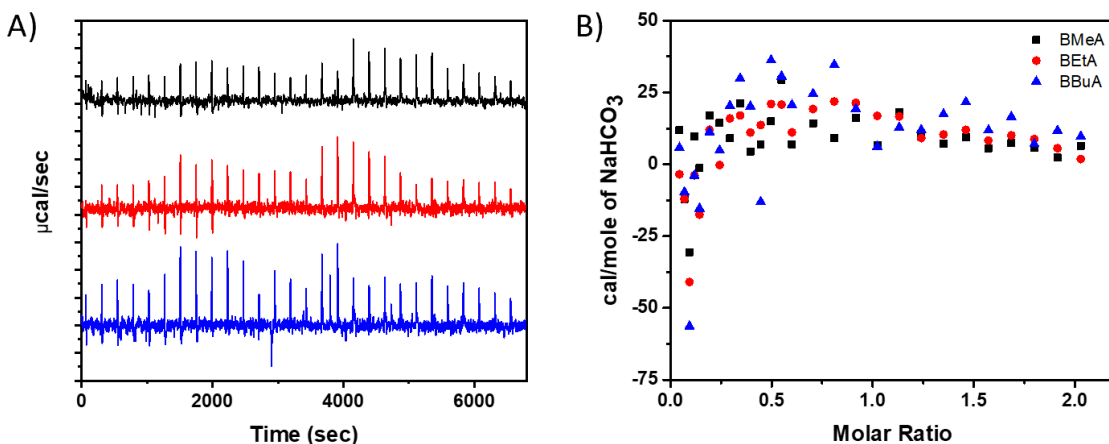
Figure 69. Counterion exchange curves for nitrogen-based cations **BMeA** (black), **BEtA** (red), and **BBuA** (blue), showing no change with increased hydrophobicity. A) Raw ITC data for each cation shifted for clarity, which has been corrected for the heat of dilution of the NaHCO3 solution into water and B) Integration data plotted as a binding curve showing the decrease in the change in enthalpy for each injection as the molar ratio of NaHCO3 increased. Samples were run in MilliQ water at 25°C exchanging chloride counterions for bicarbonate.

137

Counterion exchange experiments with **BMeA**, **BEtA**, and **BBuA** probed the effect of cation hydrophobicity and steric crowding on counterion association, as those parameters could affect how the cation interacts with the counterion and the surrounding aqueous environment (Figure 70) The titration of these cations demonstrated that increasing the alkyl chain length of the cation's substituents appeared to have little effect on counterion binding. This was surprising since increasing the hydrophobicity of the cation was expected to increase the strength of the ion pair as it becomes less water soluble, but that was clearly not the case in this instance as ΔH_{tot} was similar for all three cations.[71,172]
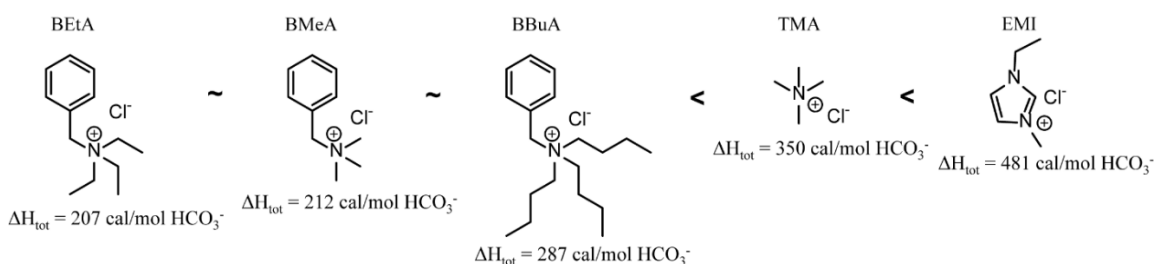
Figure 70. Nitrogen-based cations used for ITC characterization arranged in order of increasing ΔH_{tot} from left to right.

4.3.5 Importance of Ion Hydration

The differences, or lack of differences, among cations in the thermodynamics of the cation-counterion association captured by ITC were most likely related to the cation hydration on the molecular level, as opposed to the bulk hydration number obtained from the swollen membrane. It is important to note that the ion hydration relates to the number of water molecules directly interacting with the cation, which is a separate parameter from the hydration shell, which corresponds to the number of water molecules surrounding the cation, but not necessarily directly interacting with it.[170] In general, more hydrated cations have a decreased association strength with their counterions as the electrostatic interaction

with the water molecules stabilizes the charge allowing the cation to more easily release its counterion. This more facile release of counterions manifests as a decrease in the magnitude of the enthalpic response during counterion exchange as measured by ITC.[169] Furthermore, larger cations tend to have less hydration than smaller ions, as water molecules surrounding the cation interact more with each other and less with the cation, due to lower electrostatic forces and more delocalized charge associated with the larger ion.[11,170,173,174]

For example, a previous report studied the binding of various metal chloride salts to polyoxometalates using ITC.[171] As the metal was changed between Na^+, K^+, Rb^+, and Cs^+, the heat produced by binding significantly increased as the size of the cation increased. Given how increased ion size also results in reduced hydration, the increased enthalpic response was related to the decreased hydration of the ions creating stronger ion pairs. The relationship between ion hydration, ion pair strength, and the magnitude of the enthalpic response measured by ITC, regardless of whether it was exothermic or endothermic, can be understood through Figure 71. That same hydration phenomenon most likely accounts for the changes in ITC measured here. As the hydration of the cation decreases, the strength of the ion pair association between the cation and its initial counterion increases, making it more difficult to perform the counterion exchange, as expressed by a larger, more endothermic ΔH_{tot}.
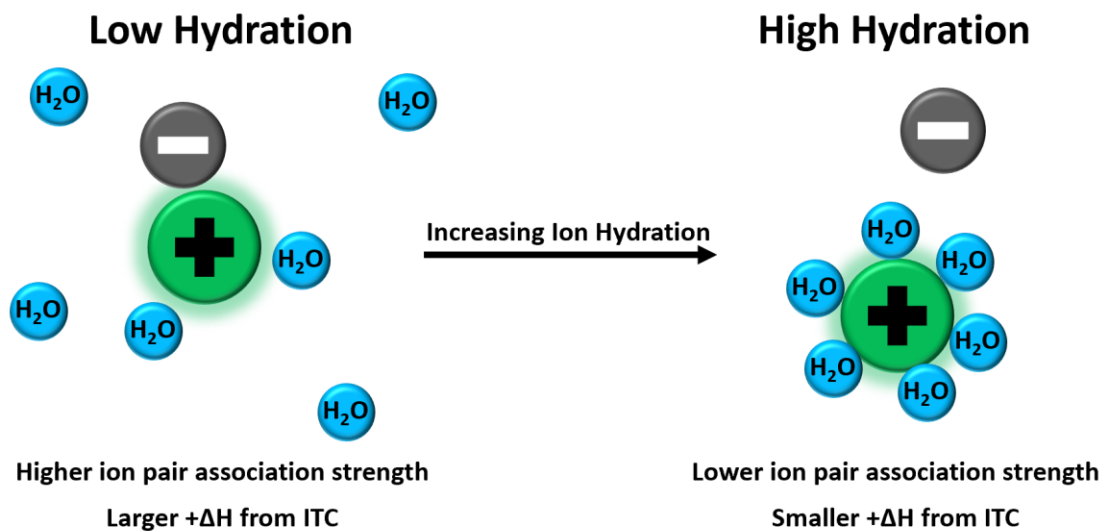
Figure 71. Illustration of the correlation between ion hydration, ion pair association strength, and the enthalpic response to breaking and forming ion pairs as measured by ITC, where green indicates the cation, grey indicates the anion, and blue indicates the water molecules.

The impact of ion hydration on the enthalpic response to counterion exchange in an ITC is perfectly exemplified with the organic cations studied. For example, despite the increased hydrophobicity, **BMeA**, **BEtA**, and **BBuA** all have similar ΔH_{tot} values, indicating they had similar levels of ion hydration. The similarity in the ΔH_{tot} values matches what is known from literature showing that tetramethylammonium and tetrabutylammonium analogues have similar levels of cation hydration, due to the water molecules' ability to penetrate the longer butyl alkyl chains and interact with the nitrogen atom.[175] Therefore, these three cations establish the connection between the enthalpic response measured by ITC and cation hydration, indicating that cation hydration had a greater impact on the enthalpic response than the cation's hydrophobicity. Furthermore, **BMeA** had a lower ΔH_{tot} than **TMA**, which was lower than **EMI**. These slight differences could also be explained by small differences in cation hydration. The stabilizing effect of the benzyl group on the cation for **BMeA** would allow the counterion to dissociate more,

140

increasing the hydration of the cation as compared to **TMA**. In addition, **TMA** should have greater hydration than **EMI** due to the increased size and delocalization of the charge on the imidazolium ring. As illustrated in Figure 71, this decreased hydration from **BMeA** to **TMA** to **EMI** would result in an increase of the initial ion pair strength with the chloride counterion, causing the larger enthalpic penalty (larger endothermic ΔH_{tot}) measured by ITC for **EMI** over **TMA**, and **TMA** over **BMeA** (Figure 70).

4.4 Conclusions

Understanding the scope in which ITC can be used to characterize the cation-counterion association strength of cations used in AEMs provides valuable insight into new material designs. Using analogous small molecule metal cations containing iron, nickel, ruthenium, zinc, manganese, and cobalt, we demonstrated that the ΔH_{tot} obtained from the counterion exchange method measured in an ITC correlates well to AEM conductivity. It was first shown that the ΔH_{tot} from ITC trends linearly with ion conductivity for nickel, ruthenium, cobalt, and iron metal cations with simple chloride counterions.

Due to the insolubility of the manganese and zinc cations in the chloride form, the ITC approach was expanded to include metal cations containing the more complex acetate counterion, which again demonstrated a linear correlation with AEM acetate conductivity similar to the correlation observed for the chloride ion. Interestingly, this data demonstrated the critical importance the nature of the counterion has on the cation-counterion association strength, where the trend in the association strength for a series of cations changes as the counter anion is changed. Modifying the terpyridine ligands with TEO to render the cations in the chloride form water soluble proved ineffective as the TEO chains appear to dominate the ITC approach so that the counterion exchange reaction yielded similar ΔH_{tot} values for

all cations. This ITC approach was expanded to characterize nitrogen-based cations, showing that measuring the enthalpic response for a counterion exchange in an ITC can be used to effectively identify the cation-counterion association strength for organic cations as well as metal cations.

The cation-counterion association strength, determined using ITC to quantify the ΔH_{tot} of a counterion exchange reaction, has proven to be a critical parameter for predicting AEM conductivity. This ITC approach has been effectively demonstrated with a series of six metal cations and two different counterions. The similarity in the ITC results for TEO functionalized cations indicates that users of this technique must take caution when attaching functional groups, as moieties that strongly interact with water or the cation will complicate results, since the technique relies on changes in the number of water molecules directly interacting with the cation. Despite the precaution of using this technique with modified cations that may influence the ITC experiment, the technique is a robust approach for determining the strength of binding between a cation and its counterion, regardless of the counterion type. The association strength between the cation and its counterion is dependent on the nature of the counterion, meaning a trend for a series of cations with one counterion will not necessarily translate to a different counterion. That demonstrates the complexity with using alternate counterions (such as chloride and bicarbonate) to explain AEM conductivity trends in fuel cells utilizing hydroxide ions. Moreover, these studies further implied that the cation hydration, as opposed to the standardly measured bulk membrane hydration, has a strong influence on the cation−counterion association thermodynamics, which accounts for the significant differences in the measured ΔH_{tot} for counterion exchange. Understanding the fundamental associations between a cation and its

counterion will inform the design of and improvements upon existing AEM materials to optimize their performance.

CHAPTER 5

USING ISOTHERMAL TITRATION CALORIMETRY TO INFORM THE SYNTHETIC DESIGN OF CATIONS FOR AEMs

5.1 Introduction

The fundamental associations between a cation and its counterion are critical for understanding and ultimately predicting AEM ion conduction. Electrostatic interactions have been well proven to weaken this cation-counterion association strength (CCAS), such as the electrostatic interaction between water and the cation, termed the ion hydration.[11,169–171,173,174] Therefore, another well-known electrostatic interaction, the cation-pi interaction, was used here to weaken the CCAS for quaternary ammonium-based cations.[74,176–178] The cations were then modified to identify design features for the strongest cation-pi interaction. Beyond the cation-pi interaction, the known stabilizing effect from proximity to electronegative groups, such as oxygen and benzene rings, was also explored as these synthetic features are common in AEM materials.

5.2 Experimental

5.2.1 Materials

Benzyl chloride, 1,3-propanediol, 1,4-butanediol, 1,6-hexanediol, 1,8-octanediol, sodium hydride, dimethylformamide (DMF), thionyl chloride, pyridine, trimethylamine (ca. 13% in tetrahydrofuran), benzyl chloromethyl ether, 2-(benzyloxy)ethanol, cyclohexanemethanol, paraformaldehyde, chlorotrimethylsilane, hexanes, ethyl acetate, diethyl ether, sodium sulfate, lithium chloride, sodium chloride, potassium chloride, rubidium chloride, sodium bicarbonate, and dimethyl sulfoxide were purchased from Sigma Aldrich, Alfa Aesar, Acros Organics, Fisher Scientific, or Tokyo Chemical Industry and were used as received.

5.2.2 Instrumentation

The ^{1}H, ^{13}C, and NOE NMR spectra were recorded using a Bruker 500 MHz Ascend NMR Spectrometer retrofitted with a cryo-probe. Isothermal titration calorimetry (ITC) was performed using a Malvern MicroCal Auto-iTC200. Effective chloride concentration was measured using a Vernier Go Direct® Chloride Ion-Selective Electrode.

5.2.3 Cation Synthesis

5.2.3.1 General Procedure.

Sodium hydride was suspended in DMF in a 50 mL round bottom flask. The flask was then purged with N_2 gas. The corresponding diol was dissolved in DMF and added to the sodium hydride solution *via* syringe. The solution was stirred for 30 minutes at room temperature after which benzyl chloride was added *via* syringe. The mixture was then stirred at room temperature overnight. In the morning, the remaining sodium hydride was quenched slowly with RO water. The solution was further diluted with RO water and extracted three times with diethyl ether. The organic phase was dried over sodium sulfate, filtered and concentrated under vacuum. The crude product was purified using a CombiFlash Isco automated silica column with an eluent mixture of ethyl acetate and hexanes. A gradient from 0% to 30% ethyl acetate over 40 min at a flow rate of 25 mL/min was sufficient for separation. The product was concentrated after which thionyl chloride and pyridine were added to the flask. The solution was then refluxed with stirring for 2 hours and then quenched with RO water. The product was extracted with diethyl ether three times and dried over sodium sulfate. The salt was filtered, and the solvent was removed under vacuum. The crude product was then dissolved in trimethylamine (ca. 13 % in

tetrahydrofuran) and heated at 100 ˚C for 24 hours. The pure product was filtered from the solution and dried under vacuum for 24 hours.

5.2.3.2 Methyl.

The **Methyl** cation was synthesized by dissolving benzyl chloromethyl ether (1.2 mL, 0.009 mol) in trimethylamine (20 mL) and stirring at room temperature for 24 hours. The product precipitated out of solution and was filtered. The pure product was dried under vacuum for 24 hours and obtained as a white powder (yield 1.53 g). ^{1}H NMR (D_2O, ppm, 500 MHz): 7.46 (5H, m), 4.92 (2H, s), 4.68 (2H, s), 3.07 (9H, s).

5.2.3.3 Propyl.

The **Propyl** cation was synthesized as described above using the following amounts: sodium hydride (2 g, 0.083 mol) was dissolved in DMF (10 mL), 1,3-propanediol (3.14 mL, 0.04 mol) was dissolved in DMF (5 mL), benzyl chloride (1 mL, 0.009 mol), thionyl chloride (20 mL, 0.27 mol), pyridine (2 mL, 0.025 mol), trimethylamine (20 mL). The product was obtained as an off-white solid (yield 0.39 g). ^{1}H NMR (D_2O, ppm, 500 MHz): 7.43 (5H, m), 4.56 (2H, s), 3.67 (2H, t), 3.37 (2H, m), 3.08 (9H, s), 2.07 (2H, m).

5.2.3.4 Butyl.

The **Butyl** cation was synthesized as described above using the following amounts: sodium hydride (2 g, 0.083 mol) was dissolved in DMF (10 mL), 1,4-butanediol (3.8 mL, 0.04 mol) was dissolved in DMF (5 mL), benzyl chloride (1 mL, 0.009 mol), thionyl chloride (20 mL, 0.27 mol), pyridine (2 mL, 0.025 mol), trimethylamine (20 mL). The product was obtained as an off-white solid (yield 0.39 g). ^{1}H NMR (D_2O, ppm, 500 MHz): 7.43 (5H, m), 4.55 (2H, s), 3.62 (2H, t), 3.27 (2H, m), 3.05 (9H, s), 1.81 (2H, m), 1.64 (2H, m).

5.2.3.5 Hexyl.

The **Hexyl** cation was synthesized as described above using the following amounts: sodium hydride (2 g, 0.083 mol) was dissolved in DMF (10 mL), 1,6-hexanediol (5 g, 0.04 mol) was dissolved in DMF (5 mL), benzyl chloride (1 mL, 0.009 mol), thionyl chloride (20 mL, 0.27 mol), pyridine (2 mL, 0.025 mol), trimethylamine (20 mL). The product was obtained as an off-white solid (yield 0.34 g). ^{1}H NMR (D$_2$O, ppm, 500 MHz): 7.42 (5H, m), 4.54 (2H, s), 3.57 (2H, t), 3.25 (2H, m), 3.06 (9H, s), 1.75 (2H, m), 1.60 (2H, m), 1.37 (4H, m).

5.2.3.6 Octyl.

The **Octyl** cation was synthesized as described above using the following amounts: sodium hydride (2 g, 0.083 mol) was dissolved in DMF (10 mL), 1,3-propanediol (6.3 g, 0.04 mol) was dissolved in DMF (5 mL), benzyl chloride (1 mL, 0.009 mol), thionyl chloride (20 mL, 0.27 mol), pyridine (2 mL, 0.025 mol), trimethylamine (20 mL). The product was obtained as an off-white solid (yield 0.31 g). ^{1}H NMR (D$_2$O, ppm, 500 MHz): 7.42 (5H, m), 4.53 (2H, s), 3.55 (2H, t), 3.26 (2H, m), 3.06 (9H, s), 1.73 (2H, m), 1.58 (2H, m), 1.32 (8H, br).

5.2.3.7 CyMethyl.

CyMethyl was synthesized by dissolving cyclohexanemethanol (1 mL, 0.008 mol) and paraformaldehyde (0.24 g, 0.008 mol) in chlorotrimethylsilane (5 mL). The mixture was stirred for 2 hours at room temperature after which the residual solvent was removed. The crude product was then dissolved in trimethylamine (20 mL) and stirred at room temperature for 24 hours. The white precipitate was filtered and dried under vacuum

resulting in the product as a white powder (yield 1.3 g). ^{1}H NMR (D$_2$O, ppm, 500 MHz): 4.61 (2H, s), 3.70 (2H, d), 3.04 (9H, s), 1.67 (6H, br), 1.19 (3H, m), 0.99 (2H, m).

5.2.3.8 EthylOMe.

EthylOMe was synthesized by dissolving 2-(benzyloxy)ethanol (1 mL, 0.007 mol) and paraformaldehyde (0.21 g, 0.007 mol) in chlorotrimethylsilane (5 mL). The mixture was stirred for 2 hours at room temperature after which the residual solvent was removed. The crude product was then dissolved in trimethylamine (20 mL) and stirred at room temperature for 24 hours. A second oil phase was observed in the morning. The remaining solvent was decanted off after which the oil was precipitated into diethyl ether and centrifuged. The diethyl ether was decanted off and the product was dried under vacuum at 50 ˚C for 24 hours. The pure product was obtained as a clear, colorless oil (yield 1.47 g). ^{1}H NMR (D$_2$O, ppm, 500 MHz): 7.43 (5H, m), 4.61 (4H, s), 4.03 (2H, m), 3.78 (2H, m), 3.03 (9H, s).

5.2.4 Isothermal Titration Calorimetry

Isotherm titration calorimetry (ITC) was performed following a previously published procedure. An aqueous solution of NaHCO$_3$ (10 mM) was titrated into an aqueous solution containing the cationic species (1 mM), made using MilliQ water, over the course of 28 injections at a stirring speed of 750 rpm. Injection volume was 0.4 µL for the first injection, 0.5 µL for the next five injections, 1 µL for the next nine injections, and 2 µL for the remaining 13 injections. The experiment was run using the single site binding analysis method and the first injection was removed due to probable leakage from the syringe. The heat of dilution of NaHCO$_3$ into pure RO water measured by ITC and subtracted from each cation titration to ensure that NaHCO3 dilution did not influence the results.

5.2.5 Chloride Ion Selective Electrode

In a typical experiment, 8 mL of a cationic solution (5 mM for organic cations, 2.98 mM for metal chloride salts) was placed in a 20 mL scintillation vial with a stir bar. The chloride ion selective electrode was then inserted into the solution with stirring. The system was allowed to equilibrate for 1-2 minutes and then the effective concentration was measured using the electrode for 180 seconds. The average effective concentration was determined from that run. This was repeated twice more for each cation solution.

5.3 Results and Discussion

5.3.1 Synthesis of Quaternary Ammonium-Based Cations

To understand the impact the cation-pi interaction and proximity to an oxygen atom have on the CCAS, a series of seven different quaternary ammonium-based small molecule cations were synthesized (Figure 72). Five cations (**Methyl**, **Propyl**, **Butyl**, **Hexyl**, and **Octyl**) were synthesized following a three-step process starting from benzyl chloride (Figure 72A). The nomenclature for these cations indicates the number of carbons between the benzyl alcohol and the trimethylammonium (TMA) cation. For example, **Methyl** has one carbon between the oxygen and the cation, while **Octyl** has eight. The other two cations (**CyMethyl** and **EthylOMe**) were synthesized following a two-step process starting from their respective alcohols (Figure 72B). The "Cy" for **CyMethyl** indicates that there is one carbon between the oxygen and TMA cation but that the oxygen is attached to a cyclohexyl group instead of a benzene ring. **EthylOMe** indicates that there is an ethyl methyl ether linker between the benzyl oxygen and the TMA cation.

149
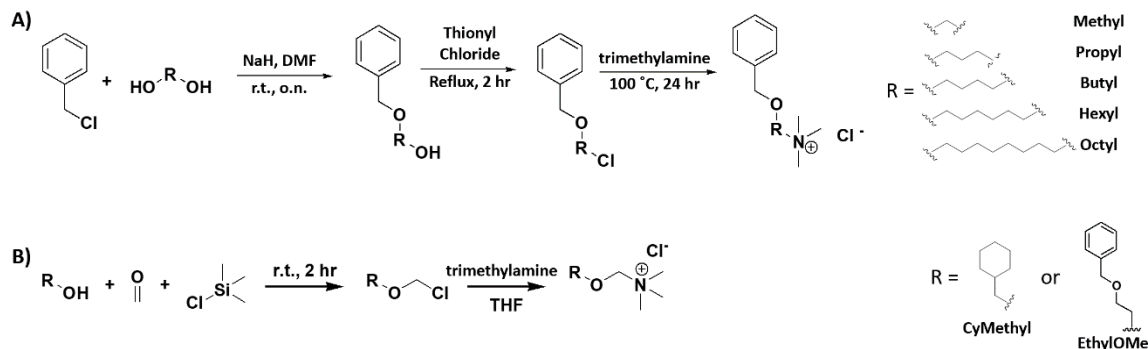
Figure 72. Synthetic scheme for A) the cation series exploring the spacer length between the benzene ring and trimethylammonium cation and B) cations exploring the impact of the benzene ring and cation proximity to the oxygen atom.

Methyl, **Propyl**, **Butyl**, **Hexyl**, and **Octyl** were designed to explore the impact of the atom linker size on the strength of the cation-pi interaction between the cation and the aromatic group. Since a ring structure needs to be formed in order for a cation-pi interaction to occur, these cations were designed to identify the optimal ring size between the two functional groups for this intramolecular interaction. However, increasing the linker size also resulted in an increased number of atoms between the cation and both the oxygen atom and benzene ring. Therefore, **CyMethyl** and **EthylOMe** were designed to elucidate the impact of proximity to the benzene ring and oxygen atom on cation stabilization, respectively.

5.3.2 NMR Characterization of Cations

5.3.2.1 1H NMR

The seven small molecule cations were first characterized using ^{1}H NMR to identify the molecule's configuration. All samples were doped with a drop of DMSO to use as a reference. Figure 73 shows the chemical shifts (δ) for the TMA peaks with the full spectrum shown in Figure 74. Shifts in the δ of the TMA peaks are the best indicators of the molecule's configuration as they indicate the presence of cation-pi interactions as well

as show the impact of proximity to the oxygen atom and benzene ring. As the number of atoms between the cation and oxygen atom increases or as the methyl groups from the TMA interact with the benzene ring more strongly, the TMA peak will shift upfield as these protons become relatively more shielded.
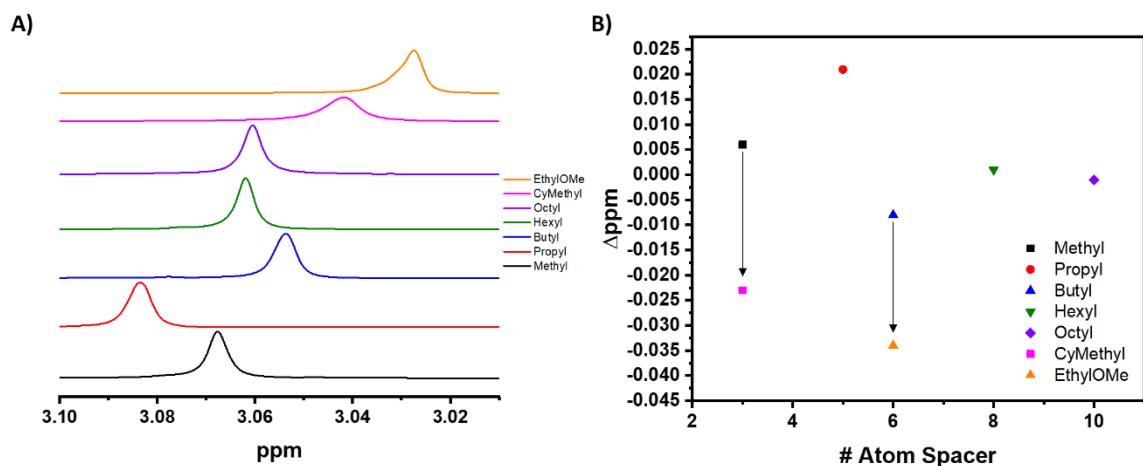
Figure 73. A) ^{1}H NMR spectrum run at room temperature in D_2O and doped with a drop of DMSO of the trimethylammonium peaks for all seven cations. B) Plot of the maximum intensity from the trimethylammonium peak in the ^{1}H NMR spectrum versus the number of atoms in the linker between the benzene ring and the ammonium cation, where a $-\Delta$ppm indicates an upfield shift as compared to the ppm for **Hexyl and Octyl.** Arrows represent the change in chemical shift based on removal of aromaticity in the molecule (Methyl $\rightarrow$ CyMethyl) and increasing the proximity to the oxygen atom (Butyl $\rightarrow$ EthylOMe).
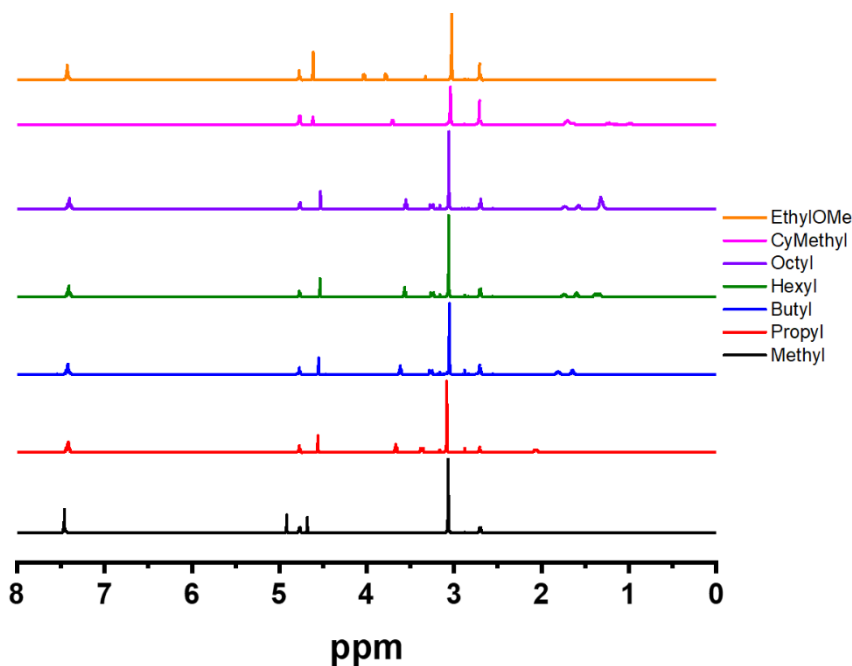
Figure 74. ^{1}H NMR spectrum run at room temperature in D$_2$O and doped with a drop of DMSO of all seven cations.

Distinct differences are observed for the δ of the methyl groups attached to the quaternary ammonium cation, however a clear trend is difficult to elucidate. The differences in chemical shifts for each cation are shown in Figure 73B and Table 15, where the difference in δ is referenced to the average chemical shift for the TMA peaks from **Hexyl** and **Octyl**, as these two cations demonstrated very little difference in δ from their interaction with the benzyl oxygen and the benzene ring. If the number of atoms between the benzyl oxygen and the TMA moiety dominated the δ of the TMA peaks, then the peaks would simply shift upfield with decreasing magnitudes from **Methyl** to **Octyl**, similar to what is seen for the methylene protons α to the nitrogen atom (Figure 75). Similarly, if the strength of the cation-pi interaction dominated the chemical shifts, then as the cation-pi interaction weakened the chemical shift of the TMA peaks would simply shift downfield.

152
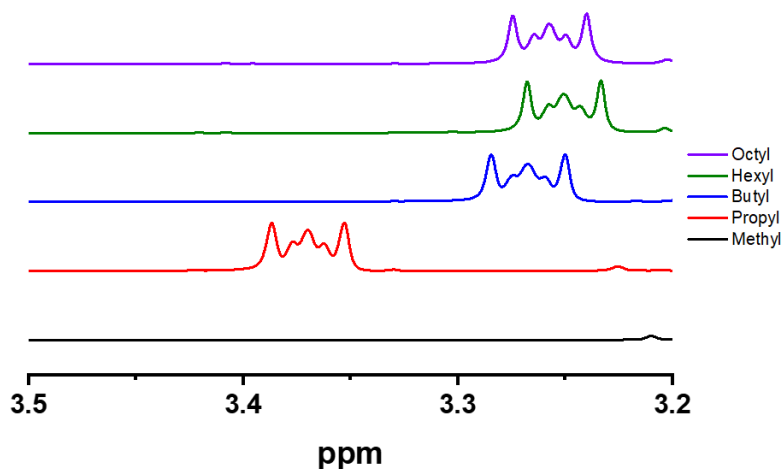
Figure 75. ^1H NMR spectrum run at room temperature in D_2O and doped with a drop of DMSO of all seven cations zoomed in on the methylene group α to the TMA group. The methylene protons α to the TMA group on **Methyl** appear at a chemical shift of 4.92 ppm.

Table 15. Summary of data for all seven organic cations.

Sample	Effective Concentration (mg/L)[a]	ΔH_{tot} (cal/mol)[b]	TMA Peak (ppm)[c]	Δppm
Methyl	312 ± 13	294 ± 92	3.07	0.01
Propyl	367 ± 33	542 ± 106	3.08	0.02
Butyl	412 ± 11	766 ± 85	3.05	-0.01
Hexyl	385 ± 6.7	750 ± 103	3.06	0
Octyl	418 ± 2.6	445 ± 91	3.06	0
CyMethyl	361 ± 5.4	573 ± 53	3.04	-0.02
EthylOMe	365 ± 6.9	489 ± 90	3.03	-0.03

[a]Measured at room temperature in RO water from a solution at a concentration of 5 mM, average of three trials with each trial measured for 180 seconds. [b]Counterion exchange reaction from chloride to bicarbonate, average of three trials. [c]Maximum intensity for the trimethylammonium peak from the ^1H NMR spectrum in D_2O doped with a drop of DMSO as a reference.

Figure 73 and Table 15 demonstrate that the influence from both the benzyl oxygen and cation-pi interactions are present in these cations. For example, when comparing **Methyl** and **Propyl**, the TMA peaks were expected to shift upfield as the number of atoms between it and the benzyl oxygen increases, however the TMA peak shifts downfield, indicating that **Methyl** has a stronger interaction with the electron cloud of the benzene

153

ring than **Propyl**. When comparing **Butyl** and **Hexyl**, a similar trend is observed as the **Butyl** TMA peaks are slightly upfield despite the closer proximity to the benzyl oxygen, again indicating a slightly stronger cation-pi interaction. Given these results, it is difficult to decouple the impact of these two factors for **Methyl**, **Propyl**, **Butyl**, **Hexyl**, and **Octyl**.

Therefore, to better understand the effect of each factor, **CyMethyl** and **EthylOMe** were synthesized and characterized. By comparing **Methyl** and **CyMethyl**, the impact of the aromatic group can be better understood, while **Butyl** and **EthylOMe** demonstrate the impact from proximity to the oxygen atom. Interestingly, removal of the aromaticity in **CyMethyl** resulted in an upfield shift for the TMA peak, opposite from the expected downfield shift in ppm due to the removal of any cation-pi interactions from the molecule. This upfield shift indicates that an inductive effect from the benzene ring may also affect the chemical shift of **Methyl** due to the closer proximity of TMA to the aromatic group.

Comparing **Butyl** and **EthylOMe** produces a clearer, although surprising result as the δ of the TMA peak shifted upfield for **EthlyOMe** as compared to **Butyl**. This result was unexpected since increasing the proximity to the oxygen atom should result in a downfield shift but converting the butyl linker into an ethyl methyl ether linker resulted in a clear upfield shift in ppm. The upfield shift indicated that **EthylOMe** participates in a stronger cation-pi interaction than **Butyl** despite the number of atoms between the cation and the benzene ring remaining the same. The stronger cation-pi interaction for **EthylOMe** is most likely due to the oxygen atom preferring the cis-configuration while the butyl alkyl chain prefers the trans-configuration.[179] The cis-configuration allows the molecule to more easily fold upon itself, thus promoting the cation-pi interaction. The ^{1}H NMR spectra indicate that there are three factors influencing the stability of the charge on these cations

that are difficult to decouple: 1) cation-pi interaction, 2) inductive effect from the oxygen atom, and 3) inductive effect from the benzene ring.

5.3.2.2 NOE NMR

To better elucidate each cation's configuration, 1D NOE NMR in D_2O was also taken for all seven cations (Figure 76). 1D NOE is a through-space technique where the peak of interest (the TMA peak) is saturated by irradiation with an RF field resulting in the peak intensity for the TMA peak shifting negative, while any proton close in space to the TMA peak has a positive intensity. Atoms that are not close to the TMA in space will not generate peaks in the 1D NOE spectrum. In other words, if the TMA peak participates in a cation-pi interaction for a molecule, the 1D NOE spectrum would have a positive peak corresponding to the benzene ring peak. Not surprisingly, the two most prominent peaks in each spectrum correspond to the α- and β-methylene protons to the TMA peak. Since these protons are located closest to the TMA peak, it is expected that they would produce the strongest signal in NOE.
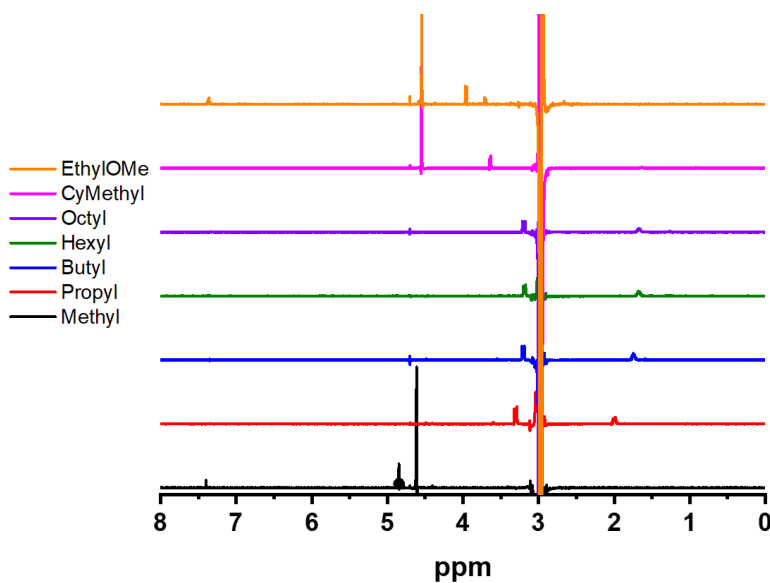
Figure 76. 1D NOE NMR spectrum run at room temperature in D_2O for all cations.

Correlating well with the ^{1}H NMR spectra, only **Methyl** and **EthylOMe** showed a significant peak corresponding to the benzene ring protons in the 1D NOE spectra, indicating they had the strongest cation-pi interaction (Figure 77). **Methyl** most likely demonstrated a strong interaction between the methyl groups from the TMA and the benzene ring because that interaction would result in a six-membered ring, which is known to be the most stable ring structure.[13] The strong interaction of **EthylOMe**, on the other hand, most likely occurred due to the preferred cis-configuration of the oxygen atom facilitating easier folding of the molecule, necessary for an intramolecular cation-pi interaction.[179] However, it was unexpected that **Butyl** did not show a response from the benzene ring protons in the 1D NOE spectrum. The ^{1}H NMR for **Butyl** indicated a slight interaction with the benzene ring, however it is possible that any interaction with the benzene ring was too weak and far away to be seen in the 1D NOE in water. Overall, the NMR data shows that controlling the ring strain is critical in facilitating cation-pi interactions for a molecule and that the ring strain can be modulated by incorporating cis-preferring moieties into the linker.
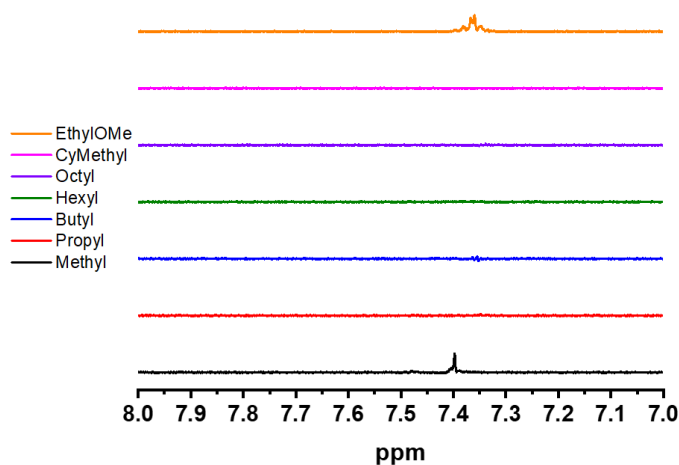
Figure 77. 1D NOE NMR spectra at room temperature in D_2O zoomed in on the area where the benzene ring peaks appear for all seven cations showing that only the ammonium cations on **Methyl and EthylOMe** have a strong interaction with the aromatic group.

5.3.3 Isothermal Titration Calorimetry

To further explore the impact cation-pi interactions and proximity to the benzyl oxygen have on the CCAS for the TMA cations, the change in enthalpy for a counterion exchange reaction was performed in an ITC (Figure 78 and Table 15). Each cation was titrated with an aqueous sodium bicarbonate solution over the course of 28 injections following the procedure previously described to perform the counterion exchange reaction from chloride to bicarbonate.[63] The change in enthalpy for each injection was measured by ITC, after which the area under the curve for each enthalpic spike measured was plotted. The total change in enthalpy (ΔH_{tot}) was then determined by summing every data point in this plot. The ΔH_{tot} was then plotted against the number of atoms between the benzene ring and the TMA cation (Figure 79). As the atom spacer was increased from three to six atoms for **Methyl**, **Propyl**, and **Butyl**, the ΔH_{tot} increased with values of 294 cal/mol, 542 cal/mol, and 766 cal/mol, respectively. Interestingly, increasing the spacer length further for **Hexyl** showed no difference from **Butyl**, with a ΔH_{tot} of 750 cal/mol, while **Octyl** showed a decrease in ΔH_{tot} to 445 cal/mol, a value similar to that of **Propyl**.
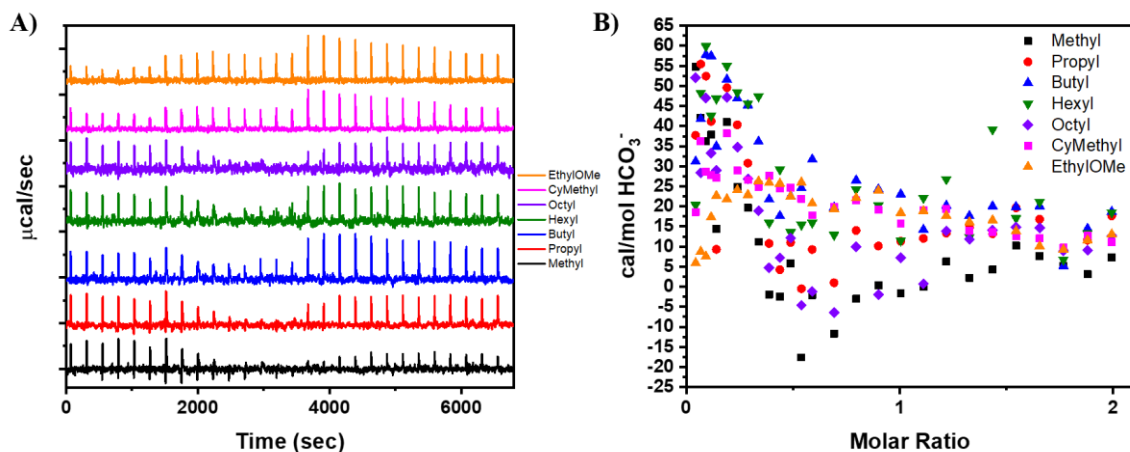
Figure 78. Counterion exchange from chloride to bicarbonate ions in Milli-Q water at 25 °C plotted using ITC for all seven quaternary ammonium-based cations: **Methyl** (black), **Propyl** (red), **Butyl** (blue), **Hexyl** (green), **Octyl** (purple), **CyMethyl** (magenta), and EthylO (orange). A) Raw ITC data, average of three trials, which has been corrected for the heat of dilution of $NaHCO_3$ into water. B) Integration data plotted showing the change in enthalpy for each injection as the molar ratio of $NaHCO_3$ increased.
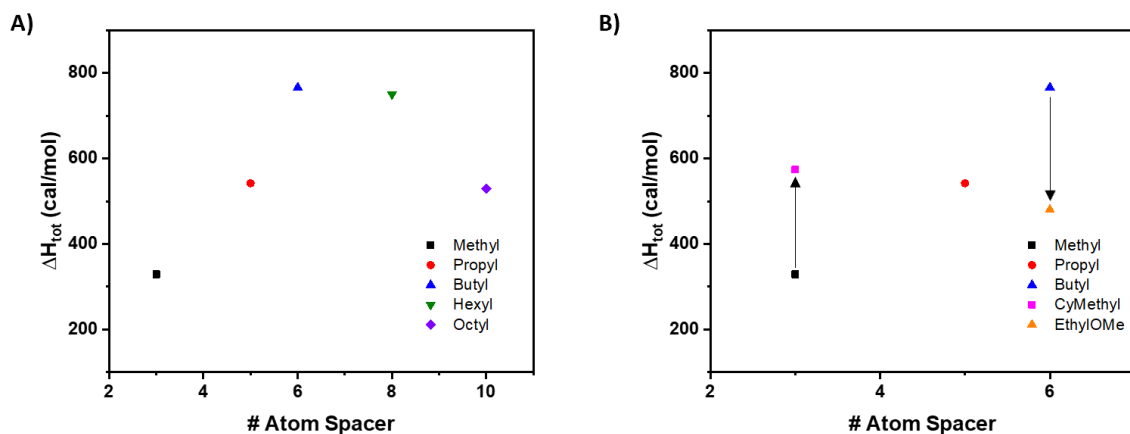
Figure 79. Plot of the ΔH_{tot} for counterion exchange from chloride to bicarbonate from an ITC versus the number of atoms between the benzene ring and ammonium cation showing the impact of A) the number of atoms between the benzene ring and ammonium cation and B) aromaticity and proximity to the oxygen atom, where the arrows represent the change in the ΔH_{tot} values based on removal of aromaticity in the molecule (**Methyl → CyMethyl**) and proximity to the oxygen atom (**Butyl → EthylOMe**).

The ITC data for **Methyl**, **Propyl**, and **Butyl** indicate that both proximity to the oxygen as well as a cation-pi interaction result in a weakened CCAS as **Methyl** was both closest to the oxygen atom and had the strongest cation-pi interaction from the NMR data.

158

It was expected that **Butyl**, **Hexyl**, and **Octyl**, would have similar ΔH_{tot} values since all three should have minimal influence from the oxygen atom and showed weak to no discernible interaction with the aromatic group. However, **Octyl** showed a significant decrease in ΔH_{tot}, indicative of a more stabilized charge and thus a weaker CCAS. The lower ΔH_{tot} value for the **Octyl** suggests that its cation was most likely stabilized through a cation-pi interaction with the benzene ring. The presence of a cation-pi interaction for **Octyl** may not have been discernible in the NMR data due to the polarizability of the water. Other than **Methyl** and **EthylOMe**, **Octyl** is the most likely candidate to form a cation-pi interaction because the **Octyl** molecule would need to form a 13-membered ring in order to participate in a cation-pi interaction, which is near the minimum ring size necessary to have the lowest possible ring strain outside of six-membered rings (Figure 80).[13]
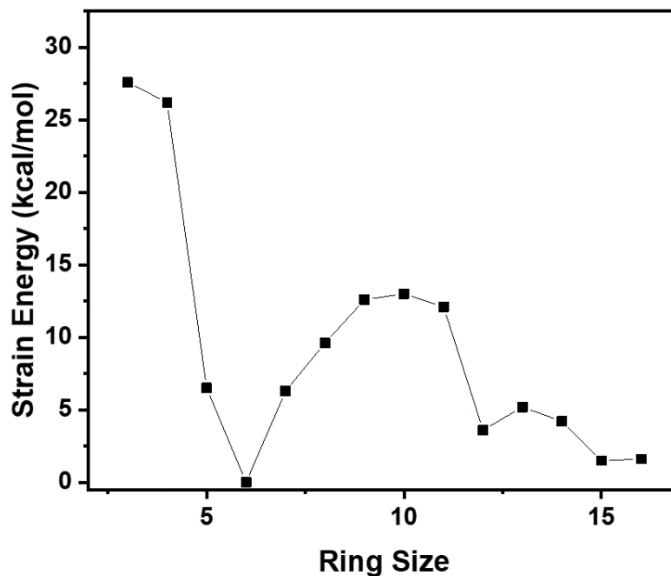
Figure 80. Plot of the strain energy versus ring size for cycloalkanes.[13]

To explore the possibility of **Octyl** having cation-pi interactions, 1D NOE NMR in CDCl$_3$ was performed to induce a stronger cation-pi interaction (Figure 81). Decreasing the dielectric constant and polarizability of the solvent is known to increase the strength of

cation-pi interactions.[180] Except for **Octyl,** no significant difference was observed for any cation as compared to the 1D NOE spectra in D_2O. In agreement with the ITC data, **Octyl** showed peaks corresponding to the benzene ring at 7.3 ppm in $CDCl_3$ as well as peaks corresponding to every linker atom, indicating stronger cation-pi interactions for this molecule in the organic solvent as opposed to water. Therefore, the longer linker between the benzene ring and TMA cation on **Octyl** seemed to favor the formation of cation-pi interactions over the shorter linkers of **Propyl**, **Butyl**, and **Hexyl** and was most likely the reason that **Octyl** showed a weaker CCAS from the ITC experiment.
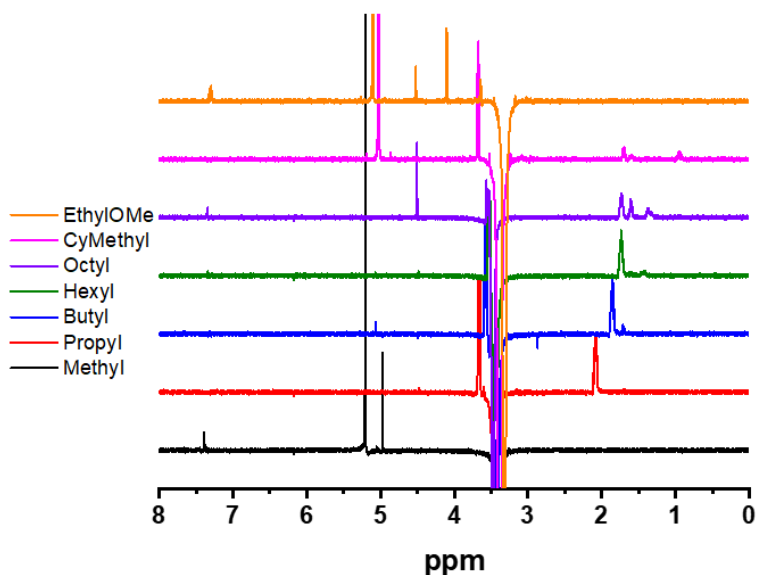
Figure 81. 1D NOE NMR spectrum run at room temperature in $CDCl_3$ for all seven cations showing that only the ammonium cations on **Methyl, Octyl** and **EthylOMe** have a strong interaction with the aromatic group.

Similar to the NMR data, **CyMethyl** and **EthylOMe** were also characterized using the counterion exchange reaction in an ITC (Figure 79B). Expectedly, removing the aromaticity for **CyMethyl** resulted in an increased CCAS while increasing the proximity of the TMA to the oxygen atom and stronger cation-pi interactions for **EthylOMe** resulted in a decreased CCAS. This observation is consistent with what was observed for the other

five cations, where proximity to the oxygen atom and cation-pi interactions weaken the CCAS and result in a lower ΔH_{tot} from the ITC experiment. Interestingly, however, **Propyl**, **Octyl**, **CyMethyl**, and **EthylOMe** all showed very similar ΔH_{tot} values and thus similar association strengths between the cation and counterion. The similarity in ΔH_{tot} values for these four cations indicates that both proximity to the oxygen atom and the cation-pi interaction have a similar stabilizing effect on the cation. For example, the **Octyl** cation is only stabilized through cation-pi interactions, but has a similar CCAS to **CyMethyl**, which is most likely only stabilized through proximity to the oxygen atom.

5.3.4 Chloride Ion Selective Electrode

To further substantiate the CCAS for these cations, the effective concentration of chloride ions in water was measured for each cation using a chloride ion selective electrode (ISE) (Figure 82A and Table 15). Each cation was dissolved in RO water at a molar concentration of 5 mM. The ISE was then inserted into the solution and the effective concentration was measured by the electrode for 180 seconds, after which the average effective concentration was determined. The measured effective chloride concentration corresponds to the activity of the chloride ions in solution as measured by the ISE, where a larger measured activity typically results in a larger effective concentration. The measured effective concentration for the cations studied here was plotted against the number of atoms in the linker between the TMA cation and the benzene ring (Figure 82B). Effective concentrations of 312 mg/L, 367 mg/L, 412 mg/L, 385 mg/L, and 418 mg/L were observed for **Methyl**, **Propyl**, **Butyl**, **Hexyl**, and **Octyl**, respectively. As the spacer size increased, the measured effective concentration also increased until a spacer of 6 atoms (**Butyl**), after which the effective concentration showed more scatter.

161
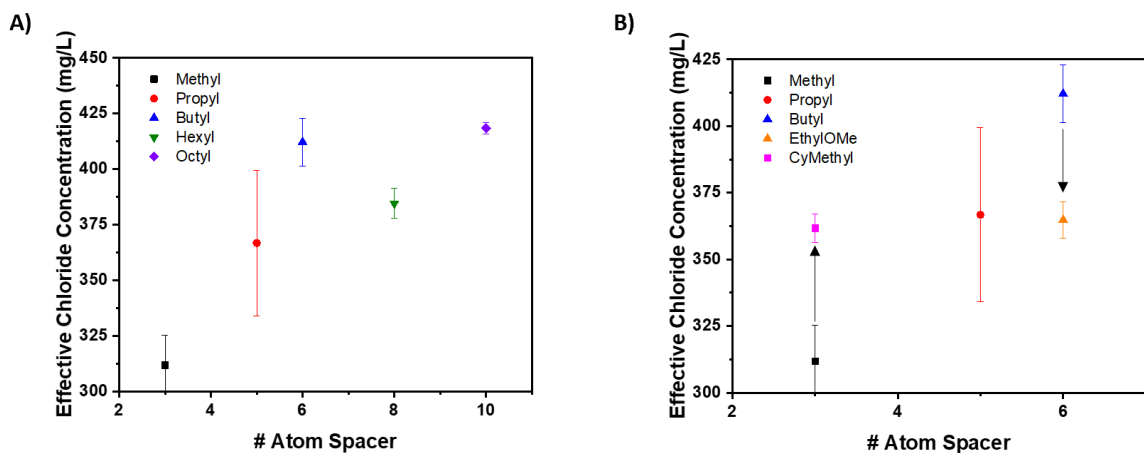
Figure 82. Plot of the effective concentration of each cation in RO water from a chloride ion selective electrode versus the number of atoms between the benzene ring and ammonium cation showing the impact of A) the number of atoms between the benzene ring and ammonium cation and B) aromaticity and proximity to the oxygen atom, where the arrows represent the change in the effective concentration based on removal of aromaticity in the molecule (**Methyl → CyMethyl**) and proximity to the oxygen atom (**Butyl → EthylOMe**).

However, the activity of the chlorine ions, represented through the measured effective chloride concentration, is highly dependent on the presence of the cation due to interactions between the two ions. These interactions cause deviations from ideal behavior, which means the activity of chloride ions cannot be considered independently from the presence of the cations, as represented through equation 12:

$$a = \gamma c \tag{12}$$

Where a is the activity (represented as the measured effective chloride concentration in mg/L), γ is the activity coefficient, and c is the concentration of total ions added to the solution (mg/L). The activity coefficient has been described as the thermodynamic degree of dissociation for ion pairs in solution, where a larger γ (approaching a value of 1) corresponds to more dissociation.[181–183] Since this activity coefficient parameter accounts for the deviation from ideal behavior, it was calculated for the seven cations studied here

and plotted against the number of atoms in the linker between the TMA cation and the benzene ring (Figure 83). γ was calculated to account for differences in molecular weights for the different cations as the measured effective chloride concentration (mg/L) was dependent on the mass of ions added, showing the impact of the molecular size on the measured activity. From the plots of γ, **Octyl** showed a slight difference from **Methyl**, **Propyl**, **Butyl**, and **Hexyl**, which all showed similar values within error. **CyMethyl** and **EthylOMe** showed slight differences from their counterparts **Methyl** and **Butyl**, respectively, however they did not show significant differences from other cations. Both were similar to **Propyl**, while **CyMethyl** was similar to **Butyl** and **EthylOMe** was similar to **Methyl**.
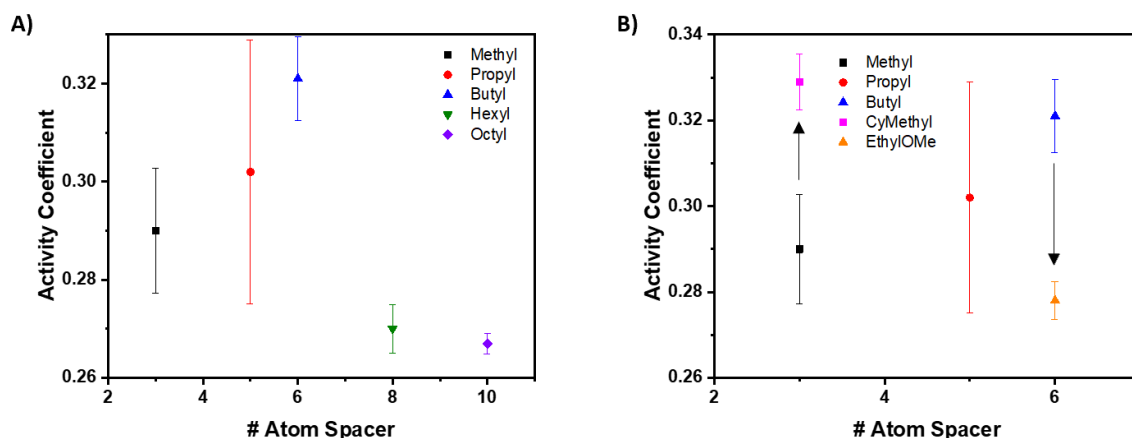
Figure 83. Plot of the activity coefficient of each cation in RO water from a chloride ion selective electrode versus the number of atoms between the benzene ring and ammonium cation showing the impact of A) the number of atoms between the benzene ring and ammonium cation and B) aromaticity and proximity to the oxygen atom, where the arrows represent the change in γ based on removal of aromaticity in the molecule (**Methyl →** **CyMethyl**) and proximity to the oxygen atom (**Butyl → EthylOMe**).

The similarities in γ were surprising since differences in the CCAS were expected to result in larger changes in γ. The expected impact of the CCAS on γ was demonstrated using alkali metal chloride salts showing that decreasing the CCAS resulted in a lower

measured effective concentration by the ISE and significantly larger γ values (Figure 84). For alkali metal salts, the CCAS in water follows the trend of Li < Na < K < Rb, meaning that Li will dissociate the most and Rb will dissociate the least.[184–190] The γ data for the metal salts matches the trend in the CCAS for these salts, as Li had a γ of 1 (most ion dissociation), while Na, K, and Rb, showed decreasing ion dissociation through decreasing γ values of 0.89, 0.70, and 0.44, respectively. The γ values measured here match well with literature.[191–193] Therefore, the alkali metal salts demonstrate that the chloride ISE can be used to quantify differences in the CCAS. Conversely, the ISE data for the alkali metal salts indicates that the ISE fails to quantify differences in the CCAS for the seven organic, quaternary ammonium-based cations studied here due to the similarities observed for their γ values. Perhaps the differences in CCAS for the organic cations in water is smaller than for the alkali metal salts, leading to the similar data from the ISE for the organic cations. Interestingly, the γ for the organic cations was significantly smaller than for the metal salts, indicating the need to develop organic cations with much larger γ values to have significantly weaker CCAS.
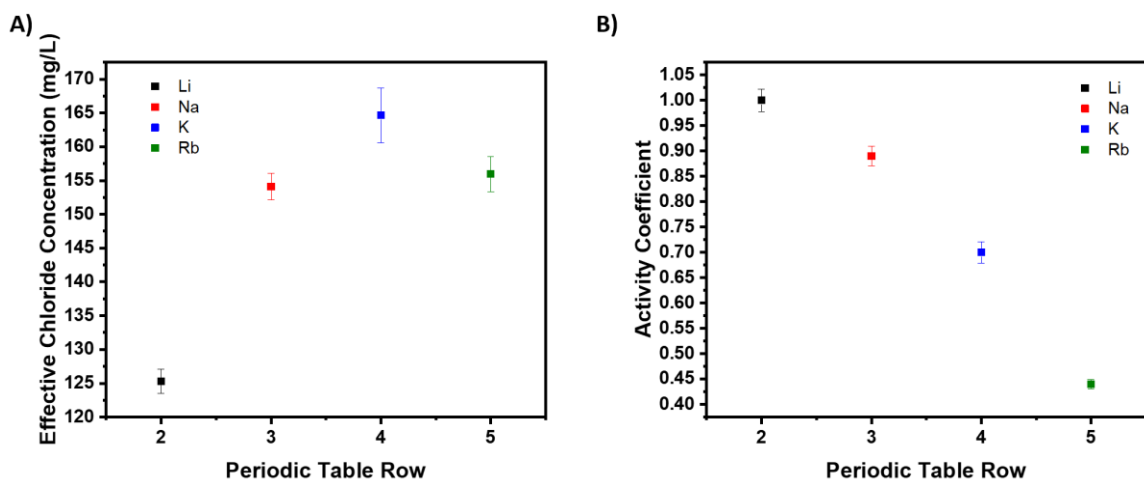
Figure 84. Plot of the A) effective chloride concentration and B) activity coefficient of LiCl, NaCl, KCl, RbCl in an aqueous 2.95 mM solution from a chloride ISE versus the row in the periodic table that each metal resides.

5.4 Conclusions

The CCAS for seven organic, quaternary ammonium-based cations was characterized to elucidate design parameters of the cations that lead to weaker association strengths. These cations were characterized using NMR to elucidate the configuration of the cations, while the CCAS was established from ITC experiments. A chloride ISE was used in an attempt to corroborate the ITC data, however the ISE did not appear to capture differences in the CCAS for the quaternary ammonium-based cations studied.

From these characterizations, two design parameters were identified as promising candidates to stabilize the cation and weaken the CCAS: 1) cation-pi interactions and 2) proximity to electronegative atoms, such as oxygen. Of special interest for AEM applications was inducing cation-pi interactions with a long linker between the aromatic group and the cation. A linker chain allowing for rings of 13 atoms or longer results in stronger cation-pi interactions than linker chains forming shorter ring structures, due to the decrease in ring strain as ring size increases beyond 12 atoms. Furthermore, the addition of moieties preferring the cis-configuration appears to be another promising route to enhancing the presence of cation-pi interactions. This increased cation-pi interaction weakens the CCAS, which has been shown to enhance ion conduction in AEMs. Increasing the number of atoms between the aromatic group and the cation by designing longer linker chains has the potential to not only enhance AEM ion conduction, but also enhance the chemical stability of the cation.[72,74,194] Therefore, synthesizing cations specifically to have cation-pi interactions appears to be a promising approach to enhancing AEM ion conductivity while simultaneously enhancing cation chemical stability.

CHAPTER 6

CONCLUSIONS AND FUTURE DIRECTIONS

This dissertation primarily focused on developing deeper, more molecular-level understandings of ion conduction in anion exchange membranes (AEMs). To accomplish this, performing a counterion exchange reaction using isothermal titration calorimetry (ITC) was established as an effective method for elucidating the cation-counterion association strength (CCAS) for various metal and organic cations. The CCAS was identified as a new molecular-level parameter that is critical for understanding and predicting ion conduction in AEMs. This dissertation utilized bis(terpyridine)metal cation-based AEMs to develop this new parameter, as these metal cations provide a unique opportunity to change the cation's identity and monitor its impact on ion conduction without also altering other AEM properties. By using metal cation-based AEMs, both the cation's and counterion's identity were established as critical components of the AEM impacting the material's ion conduction. Traditionally, hydroxide ions are substituted with alternate anions, such as chloride and bicarbonate, to elucidate conductivity trends in AEMs, however the data in this dissertation indicates that this may be more complex than initially expected. Therefore, elucidating AEM conductivity trends for hydroxide ions may be required to fully understand how a material will perform in an anion exchange membrane fuel cell. Finally, the CCAS was utilized to develop quaternary ammonium-based cations specifically designed to have a weaker association, induced by stabilization of the positive charge through cation-pi interactions. This data showed that extremely long side-chains (at least 10 atoms or longer) have potential to enhance ion conduction.

This ITC counterion exchange technique is a promising approach that can inform the design of AEMs to optimize their ion conductivity. However, questions about both the

166

technique and the CCAS parameter remain. Therefore, the next steps for this work can be summarized by three main topics: 1) further developing this ITC technique and elucidating the conclusions obtained from it, 2) relating the CCAS for small molecules to polymers and crosslinked networks, and 3) using the CCAS to develop AEMs with optimized ion conductivity.

Before the enthalpic response measured from counterion exchange in an ITC can fully reach its potential as a tool to predict AEM ion conduction, the data obtained from the reaction must be better understood. Currently, the data is summarized as a total change in enthalpy (ΔH_{tot}) value which is then correlated to the ion conductivity in an AEM. While this ΔH_{tot} value has shown potential in predicting ion conduction, a deeper analysis of the thermodynamics of counterion exchange as they relate to the thermodynamics of dissociation between the cation and its counterion would allow for a fuller understanding of this parameter and its influence on ion conduction.

First, elucidating the details that can be obtained from the enthalpy data is required. This can be accomplished in three different ways: 1) reducing the noise of the data, 2) developing or identifying a fit for the data, and 3) determining why the data does not reduce to zero enthalpic response at large molar ratios of bicarbonate to chloride ions. Currently, the data obtained from the ITC shows very weak and noisy enthalpic responses. The scatter in the data is most likely a result of systematic variations from the technique that are having large impacts on the data due to the weak enthalpic responses observed. Therefore, the first step towards elucidating the details that can be obtained from this data is to increase the enthalpic response, most easily accomplished by increasing the concentration of cations in the solution. Producing a larger enthalpic response would mean that the small systematic

167

variations in the technique would account for a much smaller percentage of the measured output, resulting in much smaller variations in the data. The low 1 mM concentration was initially chosen due to the metal cation's limited solubility in water. However, as organic cations become the focus, the water solubility will increase, and higher concentrations can be utilized. Before larger concentrations could be used, an upper concentration limit would need to be define as large pH changes from injection of the sodium bicarbonate into the solution can dominate the enthalpic response. Therefore, the initial studies would need to perform a concentration ramp to examine at what concentrations the change in pH from sodium bicarbonate becomes problematic to understand the concentration limits for the bicarbonate counterion exchange.

The increased concentration and reduced noise would also help solve the second challenge for this technique: developing or identifying an equation to fit the data. Fitting the data allows for the full thermodynamic profile of the reaction to be calculated, producing a binding constant that can be used to better quantify the association between the cation and its counterion. Since this reaction is an entropy driven reaction, due to the movement and release of water molecules, a better understanding of the entropy associated with the reaction will allow for a better understanding of what leads to the weaker CCAS for different cation-counterion pairs. The impact of entropy as it relates to the ion hydration of cations will be discussed in more detail later. The current data could not be fit due to the noise in the data, however as that is reduced, it is expected that a clearer curve will be obtained allowing for more facile fitting of the data. Initially, the fitting would be attempted with standard fitting equations assuming either single site binding or multi-site binding, where modifications are not expected to be necessary but would be performed if required.

An interesting observation from the current ITC data is that the data seems to level off at 15-30 cal/mol HCO_3^-, as opposed to the expected zero cal/mol HCO_3^-. It was expected that after the reaction reached equilibrium further addition of sodium bicarbonate would not produce an enthalpic response, as no exchange reaction should occur after that point. However, that was not the case for the data in this dissertation. Therefore, to elucidate the reason for the persisting enthalpic response at higher molar ratios, the first step is to perform a titration to much larger molar ratios to determine if the reaction requires larger molar ratios to complete the exchange reaction. Perhaps exchange of the second counterion of metal cations is more difficult than exchange of the first, thus requiring larger molar ratios of bicarbonate ions. If the data never reaches zero cal/mol HCO_3^- at larger molar ratios, then it is possible that the enthalpic value that the titration reaches corresponds to equilibrium, and thus a correction or normalization is required to account for this. This could be possible if the equilibrium includes a small percentage of counterion-exchange reactions continuously occurring, since the initial chloride ions are still present in the solution, resulting in a small enthalpic response.

Once a more complete thermodynamic profile is obtained for these ITC titrations, the next critical step is to elucidate the role of water on the CCAS and the enthalpic response in the ITC. As discussed above, this is an entropy driven process, most likely driven by release of water molecules. Furthermore, it has been well established that the level of ion hydration a cation experiences directly relates to the CCAS, where more ion hydration relates to a weaker association strength. However, for this dissertation the number of water molecules interacting with the cation has been referred to exclusively in relative terms, where a larger ΔH_{tot} value simply corresponds to less ion hydration. Once

169

the full thermodynamic profile is obtained, the number of water molecules interacting with the cation can be more accurately determined as the entropy and enthalpy of hydration for common cations is known. More accurately quantifying the amount of ion hydration would result in a deeper understanding of the role of water in the thermodynamics of dissociation for these small molecule cations, which will be critical in correlating the dissociation results for these small molecule cations to their results when incorporated into polymers and crosslinked networks.

Elucidating how the dissociation thermodynamics for small molecule cation-counterion pairs correlates to their dissociation when incorporated into polymeric structures is another important factor required to fully understand the role of the CCAS on AEM ion conduction. This relationship is important to understand because polyelectrolytes and crosslinked membranes experience an important phenomenon impacting ion conduction that small molecule cations do not: counterion condensation. Counterion condensation describes the location of counterions around a polyelectrolyte and has a critical influence on the percentage of free ions available for conduction as well as the diffusion of those ions.[92] It has also been shown that counterion condensation is directly related to the location of water around the cations of the polymer. However, the counterion condensation observed in ionic membranes is not well understood and is notoriously difficult to measure quantitatively.[90,92,195–197] Therefore, correlating the dissociation thermodynamics between small molecule cations and their counterions to the dissociation thermodynamics of polymers and crosslinked membranes would represent an advancement in understanding counterion condensation and how that impacts ion conduction.

The first step towards elucidating this relationship is to perform the same counterion exchange reactions in the ITC on linear polycations as that performed on the small molecule cations. Initial experiments would use the benzyltrimethylammonium cation as a small molecule and as the moiety on a polyelectrolyte, as that cation is facile to synthesize and is the most common cation used for AEM applications. Developing the full thermodynamic profile for each species would elucidate the role of ion hydration and counterion exchange on the thermodynamics of dissociation between the cation and its counterion in both the small molecule and polyelectrolyte. Relating the dissociation thermodynamics for small molecules and polymers would allow for a better understanding of how counterion condensation and the enthalpic response for counterion exchange of small molecules can influence and predict ion conduction in polymeric AEMs. Finally, the impact of the cation's identity and polymer backbone on the counterion condensation and the relationship between small molecules and polymers would be explored for various organic cations.

As mentioned above, not only is the identity of the cation critical to the CCAS, but the identity of the counterion is also crucial. It was shown in this thesis that metal cations in the chloride form showed a different trend in associations strengths than the same cations in the acetate form, indicating that conductivity trends for a series of cations with one counterion cannot reliably be correlated to their conductivity with another counterion. Therefore, while this work primarily focused on characterizing cations in the chloride form to develop the ITC counterion exchange technique and identify the critical importance of the CCAS, characterizing the CCAS of cations in the hydroxide form will be required in the future. This poses a challenge to this ITC technique because large changes in pH are

171

known to dominate the enthalpic response in an ITC, making results unreliable, which is why counterion exchange with chloride, acetate, and bicarbonate ions was chosen.

One possible approach to characterizing the CCAS for cations in the hydroxide form would be to synthesize cations in the hydroxide form and then perform the same counterion exchange reaction in the ITC as before, converting the cation to the bicarbonate form. This approach would take advantage of the change in pH upon release of hydroxide ions to measure the exchange reaction as any enthalpic response due to change in pH from the hydroxide ions would correlate to the exchange reaction occurring. The challenge with this approach is synthesizing cations in the hydroxide form, although a multi-step counterion exchange could be performed (such as Cl^- → PF_6^- → OH^-). A multi-step counterion exchange would take advantage of changes in water solubility between the Cl^- form and PF_6^- and then again between the PF_6^- and OH^- forms.

Using the ITC approach quantifying the CCAS to inform the design of cations specifically to have a weaker association was proposed for various small molecule, quaternary ammonium-based cations studying the impact of the linker between an aromatic group and the cation. That work indicated that inducing cation-pi interactions, either through adding moieties into the linker chain that prefer the cis-configuration or by making the linker extremely long (10 atoms or longer), results in stronger cation-pi interactions and thus weaker CCAS. The next step for this work is to fully understand the NMR and ion selective electrode (ISE) data obtained for these molecules. The NMR data is complicated due to the presence of the oxygen atoms. If the configurations of the different cations cannot be elucidated with the current molecules, synthesizing the same molecules

without the oxygen atom in the linker would simplify the NMR data and allow for easier determination of the molecule's configuration.

Furthermore, the activity coefficient (γ) calculated from the measured effective chloride concentration from the ISE indicates that the ISE was not able to capture the differences in the CCAS for the organic cations studied here. Therefore, developing an approach to significantly increasing γ or identifying another technique for quantifying the CCAS for organic cations is needed. Increasing γ would most likely require drastic changes to the cation, so initial studies would explore different cations, such as imidazolium, phosphonium, and sulfonium. Furthermore, different functionalities would be studied, such as moieties that induce cation-pi interactions for the different types of cations.

Once the data for the small molecule cations is understood and the best cations are identified, the next step is to design and synthesize AEMs that take advantage of the design parameters determined from the small molecules. Based on the design features identified in this thesis, enhanced ion conduction could be accomplished by synthesizing aromatic-containing, polymeric materials that contain extremely long linkers between the polymer backbone and the cationic head group. The linkers would include both long alkyl chains as well as ether-containing chains, to determine if extremely long linkers containing moieties preferring the cis-configuration result in an even greater enhancement of ion conduction through a weaker CCAS. These materials would most likely also have the added benefit of demonstrating enhanced chemical stability as longer linkers have been shown to improve cation chemical stability. These AEMs would represent the first materials designed to specifically contain a weaker CCAS to enhance ion conduction while simultaneously improving AEM chemical stability.

BIBLIOGRAPHY

(1)   Hickner, M. A.; Herring, A. M.; Coughlin, E. B. *J. Polym. Sci. Part B Polym. Phys.* **2013**, *51* (24), 1727–1735.

(2)   Arges, C. G.; Ramani, V. *Proc. Natl. Acad. Sci.* **2013**, *110* (7), 2490–2495.

(3)   Sun, Z.; Lin, B.; Yan, F. *ChemSusChem* **2018**, *11* (1), 58–70.

(4)   Clark, T. J.; Robertson, N. J.; Kostalik IV, H. A.; Lobkovsky, E. B.; Mutolo, P. F.; Abruña, H. D.; Coates, G. W. *J. Am. Chem. Soc.* **2009**, *131* (36), 12888–12889.

(5)   Ertem, S. P.; Tsai, T.-H.; Donahue, M. M.; Zhang, W.; Sarode, H.; Liu, Y.; Seifert, S.; Herring, A. M.; Coughlin, E. B. *Macromolecules* **2016**, *49* (1), 153–161.

(6)   Park, E. J.; Kim, Y. S. *J. Mater. Chem. A* **2018**, *6* (32), 15456–15477.

(7)   Kostalik, H. A.; Clark, T. J.; Robertson, N. J.; Mutolo, P. F.; Longo, J. M.; Abruña, H. D.; Coates, G. W. *Macromolecules* **2010**, *43* (17), 7147–7150.

(8)   Robertson, N. J.; Kostalik, H. A.; Clark, T. J.; Mutolo, P. F.; Abruña, H. D.; Coates, G. W. *J. Am. Chem. Soc.* **2010**, *132* (10), 3400–3404.

(9)   Wang, L.; Hickner, M. A. *Polym. Chem.* **2014**, *5* (8), 2928.

(10)   Mohanty, A. D.; Ryu, C. Y.; Kim, Y. S.; Bae, C. *Macromolecules* **2015**, *48* (19), 7085–7095.

(11)   Disabb-Miller, M. L.; Zha, Y.; DeCarlo, A. J.; Pawar, M.; Tew, G. N.; Hickner, M. A. *Macromolecules* **2013**, *46* (23), 9279–9287.

(12)   Ko, B.-S.; Yoshimura, K.; Warapon, S.; Shishitani, H.; Yamaguchi, S.; Tanaka, H.; Maekawa, Y. *J. Polym. Sci. Part A Polym. Chem.* **2019**, *57* (4), 503–510.

(13)   Ferguson, L. N. *J. Chem. Educ.* **1970**, *47* (1), 46.

(14)   Hagesteijn, K. F. L.; Jiang, S.; Ladewig, B. P. *J. Mater. Sci.* **2018**, *53* (16), 11131–11150.

(15) Ran, J.; Wu, L.; He, Y.; Yang, Z.; Wang, Y.; Jiang, C.; Ge, L.; Bakangura, E.; Xu, T. *J. Memb. Sci.* **2017**, *522*, 267–291.

(16) Strathmann, H.; Grabowski, A.; Eigenberger, G. *Ind. Eng. Chem. Res.* **2013**, *52* (31), 10364–10379.

(17) Merle, G.; Wessling, M.; Nijmeijer, K. *J. Memb. Sci.* **2011**, *377* (1–2), 1–35.

(18) Kwon, S.; Rao, A. H. N.; Kim, T. H. *J. Power Sources* **2018**, *375*, 421–432.

(19) Lehmani, A.; Durand-Vidal, S.; Turq, P. *J. Appl. Polym. Sci.* **1998**, *68* (3), 503–508.

(20) Liu, D.; Kyriakides, S.; Case, S. W.; Lesko, J. J.; Li, Y.; McGrath, J. E. *J. Polym. Sci. Part B Polym. Phys.* **2006**, *44* (10), 1453–1465.

(21) Lee, C. H.; Park, H. B.; Lee, Y. M.; Lee, R. D. *Ind. Eng. Chem. Res.* **2005**, *44* (20), 7617–7626.

(22) Ono, H.; Miyake, J.; Miyatake, K. *J. Polym. Sci. Part A Polym. Chem.* **2017**, *55* (8), 1442–1450.

(23) Zhang, H.-W.; Chen, D.-Z.; Xianze, Y.; Yin, S.-B. *Fuel Cells* **2015**, *15* (6), 761–780.

(24) Cheng, J.; He, G.; Zhang, F. *Int. J. Hydrogen Energy* **2015**, *40* (23), 7348–7360.

(25) Gottesfeld, S.; Dekel, D. R.; Page, M.; Bae, C.; Yan, Y.; Zelenay, P.; Kim, Y. S. *J. Power Sources* **2018**, *375*, 170–184.

(26) Wu, B.; Ge, L.; Yu, D.; Hou, L.; Li, Q.; Yang, Z.; Xu, T. *J. Mater. Chem. A* **2016**, *4* (38), 14545–14549.

(27) Amel, A.; Gavish, N.; Zhu, L.; Dekel, D. R.; Hickner, M. A.; Ein-Eli, Y. *J. Memb. Sci.* **2016**, *514*, 125–134.

(28)   Couture, G.; Alaaeddine, A.; Boschet, F.; Ameduri, B. *Prog. Polym. Sci.* **2011**, *36* (11), 1521–1557.

(29)   Ran, J.; Wu, L.; Wei, B.; Chen, Y.; Xu, T. *Sci. Rep.* **2014**, *4* (1), 6486.

(30)   He, G.; Li, Z.; Zhao, J.; Wang, S.; Wu, H.; Guiver, M. D.; Jiang, Z. *Adv. Mater.* **2015**, *27* (36), 5280–5295.

(31)   Ren, X.; Price, S. C.; Jackson, A. C.; Pomerantz, N.; Beyer, F. L. *ACS Appl. Mater. Interfaces* **2014**, *6* (16), 13330–13333.

(32)   Li, N.; Yan, T.; Li, Z.; Thurn-Albrecht, T.; Binder, W. H. *Energy Environ. Sci.* **2012**, *5* (7), 7888.

(33)   Price, S. C.; Ren, X.; Jackson, A. C.; Ye, Y.; Elabd, Y. a; Beyer, F. L. *Macromolecules* **2013**, *46* (18), 7332–7340.

(34)   Holdcroft, S. *Chem. Mater.* **2014**, *26* (1), 381–393.

(35)   Zhu, L.; Pan, J.; Wang, Y.; Han, J.; Zhuang, L.; Hickner, M. A. *Macromolecules* **2016**, *49* (3), 815–824.

(36)   Dang, H.-S.; Jannasch, P. *J. Mater. Chem. A* **2016**, *4* (30), 11924–11938.

(37)   Zhang, W.; Liu, Y.; Jackson, A. C.; Savage, A. M.; Ertem, S. P.; Tsai, T.-H.; Seifert, S.; Beyer, F. L.; Liberatore, M. W.; Herring, A. M.; Coughlin, E. B. *Macromolecules* **2016**, *49* (13), 4714–4722.

(38)   Zeng, L.; Zhao, T. S.; Wei, L.; Jiang, H. R.; Wu, M. C. *Appl. Energy* **2019**, *233–234* (October 2018), 622–643.

(39)   Pan, J.; Zhu, L.; Han, J.; Hickner, M. A. *Chem. Mater.* **2015**, *27* (19), 6689–6698.

(40)   Meek, K. M.; Nykaza, J. R.; Elabd, Y. A. *Macromolecules* **2016**, *49* (9), 3382–3394.

(41)   Sun, Z.; Pan, J.; Guo, J.; Yan, F. *Adv. Sci.* **2018**, *5* (8).

(42)   Choe, Y.-K.; Fujimoto, C.; Lee, K.-S.; Dalton, L. T.; Ayers, K.; Henson, N. J.; Kim, Y. S. *Chem. Mater.* **2014**, *26* (19), 5675–5682.

(43)   Mohanty, A. D.; Tignor, S. E.; Krause, J. A.; Choe, Y.-K.; Bae, C. *Macromolecules* **2016**, *49* (9), 3361–3372.

(44)   Fujimoto, C.; Kim, D. S.; Hibbs, M.; Wrobleski, D.; Kim, Y. S. *J. Memb. Sci.* **2012**, *423–424*, 438–449.

(45)   Hibbs, M. R.; Fujimoto, C. H.; Cornelius, C. J. *Macromolecules* **2009**, *42* (21), 8316–8321.

(46)   Zhang, M.; Liu, J.; Wang, Y.; An, L.; Guiver, M. D.; Li, N. *J. Mater. Chem. A* **2015**, *3* (23), 12284–12296.

(47)   Noonan, K. J. T.; Hugar, K. M.; Kostalik, H. A.; Lobkovsky, E. B.; Abruña, H. D.; Coates, G. W. *J. Am. Chem. Soc.* **2012**, *134* (44), 18161–18164.

(48)   Olsson, J. S.; Pham, T. H.; Jannasch, P. *Adv. Funct. Mater.* **2018**, *28* (2), 1–10.

(49)   Tongwen, X.; Weihua, Y. *J. Memb. Sci.* **2001**, *190* (2), 159–166.

(50)   Zhang, X.; Chu, X.; Zhang, M.; Zhu, M.; Huang, Y.; Wang, Y.; Liu, L.; Li, N. *J. Memb. Sci.* **2019**, *574* (December 2018), 212–221.

(51)   Amel, A.; Zhu, L.; Hickner, M.; Ein-Eli, Y. *J. Electrochem. Soc.* **2014**, *161* (5), F615–F621.

(52)   Womble, C. T.; Coates, G. W.; Matyjaszewski, K.; Noonan, K. J. T. *ACS Macro Lett.* **2016**, *5* (2), 253–257.

(53)   Yoshimura, K.; Zhao, Y.; Hasegawa, S.; Hiroki, A.; Kishiyama, Y.; Shishitani, H.; Yamaguchi, S.; Tanaka, H.; Koizumi, S.; Appavou, M.-S.; Radulescu, A.; Richter,

D.; Maekawa, Y. *Soft Matter* **2017**, *13* (45), 8463–8473.

(54)   Jheng, L.-C.; Tai, C.-K.; Hsu, S. L.-C.; Lin, B.-Y.; Chen, L.; Wang, B.-C.; Chiang, L.-K.; Ko, W.-C. *Int. J. Hydrogen Energy* **2017**, *42* (8), 5315–5326.

(55)   Gong, X.; Yan, X.; Li, T.; Wu, X.; Chen, W.; Huang, S.; Wu, Y.; Zhen, D.; He, G. *J. Memb. Sci.* **2017**, *523* (May 2016), 216–224.

(56)   Zhang, B.; Gu, S.; Wang, J.; Liu, Y.; Herring, A. M.; Yan, Y. *RSC Adv.* **2012**, *2* (33), 12683–12685.

(57)   Hossain, M. A.; Jang, H.; Sutradhar, S. C.; Ha, J.; Yoo, J.; Lee, C.; Lee, S.; Kim, W. *Int. J. Hydrogen Energy* **2016**, *41* (24), 10458–10465.

(58)   Gu, S.; Wang, J.; Kaspar, R. B.; Fang, Q.; Zhang, B.; Coughlin, B. E.; Yan, Y. *Sci. Rep.* **2015**, *5* (1), 1–11.

(59)   Zha, Y.; Disabb-Miller, M. L.; Johnson, Z. D.; Hickner, M. A.; Tew, G. N. *J. Am. Chem. Soc.* **2012**, *134* (10), 4493–4496.

(60)   Kwasny, M. T.; Tew, G. N. *J. Mater. Chem. A* **2017**, *5* (4), 1400–1405.

(61)   Chen, N.; Zhu, H.; Chu, Y.; Li, R.; Liu, Y.; Wang, F. *Polym. Chem.* **2017**, *8* (8), 1381–1392.

(62)   Zhu, T.; Xu, S.; Rahman, A.; Dogdibegovic, E.; Yang, P.; Pageni, P.; Kabir, M. P.; Zhou, X.; Tang, C. *Angew. Chemie Int. Ed.* **2018**, *57* (9), 2388–2392.

(63)   Kwasny, M. T.; Zhu, L.; Hickner, M. A.; Tew, G. N. *J. Am. Chem. Soc.* **2018**, *140* (25), 7961–7969.

(64)   Liu, L.; He, S.; Zhang, S.; Zhang, M.; Guiver, M. D.; Li, N. *ACS Appl. Mater. Interfaces* **2016**, *8* (7), 4651–4660.

(65) Liu, Y.; Wang, J.; Yang, Y.; Brenner, T. M.; Seifert, S.; Yan, Y.; Liberatore, M. W.; Herring, A. M. *J. Phys. Chem. C* **2014**, *118* (28), 15136–15145.

(66) Gu, F.; Dong, H.; Li, Y.; Sun, Z.; Yan, F. *Macromolecules* **2014**, *47* (19), 6740–6747.

(67) Wang, J.; Chen, Y.; Wei, Q.; Yang, S.; Fang, H.; Wei, H.; Ding, Y. *Polymer (Guildf).* **2017**, *112*, 288–296.

(68) Hugar, K. M.; Kostalik, H. A.; Coates, G. W. *J. Am. Chem. Soc.* **2015**, *137* (27), 8730–8737.

(69) Wang, J.; Li, S.; Zhang, S. *Macromolecules* **2010**, *43* (8), 3890–3896.

(70) Marino, M. G.; Kreuer, K. D. *ChemSusChem* **2015**, *8* (3), 513–523.

(71) Li, N.; Leng, Y.; Hickner, M. A.; Wang, C.-Y. *J. Am. Chem. Soc.* **2013**, *135* (27), 10124–10133.

(72) Pan, J.; Han, J.; Zhu, L.; Hickner, M. A. *Chem. Mater.* **2017**, *29* (12), 5321–5330.

(73) Ran, J.; Wu, L.; Ru, Y.; Hu, M.; Din, L.; Xu, T. *Polym. Chem.* **2015**, *6* (32), 5809–5826.

(74) Jannasch, P.; Weiber, E. A. *Macromol. Chem. Phys.* **2016**, *217* (10), 1108–1118.

(75) Hibbs, M. R. *J. Polym. Sci. Part B Polym. Phys.* **2013**, *51* (24), 1736–1742.

(76) Tomoi, M.; Yamaguchi, K.; Ando, R.; Kantake, Y.; Aosaki, Y.; Kubota, H. *J. Appl. Polym. Sci.* **1997**, *64* (6), 1161–1167.

(77) Lin, B.; Qiu, L.; Lu, J.; Yan, F. *Chem. Mater.* **2010**, *22* (24), 6718–6725.

(78) Lu, D.; Li, D.; Wen, L.; Xue, L. *J. Memb. Sci.* **2017**, *533* (March), 210–219.

(79) Chen, D.; Hickner, M. A. *ACS Appl. Mater. Interfaces* **2012**, *4* (11), 5775–5781.

(80) Pan, Z. F.; An, L.; Zhao, T. S.; Tang, Z. K. *Prog. Energy Combust. Sci.* **2018**, *66*,

141–175.

(81)   Kwasny, M. T.; Zhu, L.; Hickner, M. A.; Tew, G. N. *J. Polym. Sci. Part A Polym. Chem.* **2018**, *56* (3), 328–339.

(82)   Wang, B.; Sun, W.; Bu, F.; Li, X.; Na, H.; Zhao, C. *Int. J. Hydrogen Energy* **2016**, *41* (4), 3102–3112.

(83)   Qiu, B.; Lin, B.; Qiu, L.; Yan, F. *J. Mater. Chem.* **2012**, *22* (3), 1040–1045.

(84)   Meek, K. M.; Elabd, Y. A. *Macromolecules* **2015**, *48* (19), 7071–7084.

(85)   Maurya, S.; Shin, S.-H.; Kim, M.-K.; Yun, S.-H.; Moon, S.-H. *J. Memb. Sci.* **2013**, *443*, 28–35.

(86)   Dang, H.-S.; Jannasch, P. *J. Mater. Chem. A* **2017**, *5* (41), 21965–21978.

(87)   Disabb-Miller, M. L.; Johnson, Z. D.; Hickner, M. A. *Macromolecules* **2013**, *46* (3), 949–956.

(88)   Shi, Z.; Holdcroft, S. *Macromolecules* **2005**, *38* (10), 4193–4201.

(89)   Mandal, M.; Huang, G.; Kohl, P. A. *J. Memb. Sci.* **2019**, *570–571* (August 2018), 394–402.

(90)   Beers, K. M.; Hallinan, D. T.; Wang, X.; Pople, J. A.; Balsara, N. P. *Macromolecules* **2011**, *44* (22), 8866–8870.

(91)   Sinn, C. G.; Dimova, R.; Antonietti, M. *Macromolecules* **2004**, *37* (9), 3444–3450.

(92)   Kamcev, J.; Paul, D. R.; Manning, G. S.; Freeman, B. D. *Macromolecules* **2018**, *51* (15), 5519–5529.

(93)   Ahluwalia, R. K.; Wang, X. *J. Power Sources* **2008**, *177* (1), 167–176.

(94)   Anantaraman, A. V.; Gardner, C. L. *J. Electroanal. Chem.* **1996**, *414* (2), 115–120.

(95)   Li, Y. S.; Zhao, T. S.; Yang, W. W. *Int. J. Hydrogen Energy* **2010**, *35* (11), 5656–

5665.

(96)   Baştuğ, T.; Kuyucak, S. *Chem. Phys. Lett.* **2005**, *408* (1–3), 84–88.

(97)   Prakash, G. K. S.; Krause, F. C.; Viva, F. A.; Narayanan, S. R.; Olah, G. A. *J. Power Sources* **2011**, *196* (19), 7967–7972.

(98)   Pan, J.; Li, Y.; Han, J.; Li, G.; Tan, L.; Chen, C.; Lu, J.; Zhuang, L. *Energy Environ. Sci.* **2013**, *6* (10), 2912–2915.

(99)   Stoica, D.; Ogier, L.; Akrour, L.; Alloin, F.; Fauvarque, J.-F. *Electrochim. Acta* **2007**, *53* (4), 1596–1603.

(100)   Pinsent, B. R. W.; Pearson, L.; Roughton, F. J. W. *Trans. Faraday Soc.* **1956**, *52* (1512), 1512.

(101)   Yan, J.; Hickner, M. A. *Macromolecules* **2010**, *43* (5), 2349–2356.

(102)   Marino, M. G.; Melchior, J. P.; Wohlfarth, A.; Kreuer, K. D. *J. Memb. Sci.* **2014**, *464*, 61–71.

(103)   Chen, C.; Tse, Y.-L. S.; Lindberg, G. E.; Knight, C.; Voth, G. A. *J. Am. Chem. Soc.* **2016**, *138* (3), 991–1000.

(104)   MacInnes, D. A.; Shedlovsky, T.; Longsworth, L. G. *J. Am. Chem. Soc.* **1932**, *54* (7), 2758–2762.

(105)   Zhu, L.; Zimudzi, T. J.; Wang, Y.; Yu, X.; Pan, J.; Han, J.; Kushner, D. I.; Zhuang, L.; Hickner, M. A. *Macromolecules* **2017**, *50* (6), 2329–2337.

(106)   Ran, J.; Wu, L.; Lin, X.; Jiang, L.; Xu, T. *RSC Adv.* **2012**, *2* (10), 4250.

(107)   Varcoe, J. R.; Slade, R. C. T.; Lam How Yee, E.; Poynton, S. D.; Driscoll, D. J.; Apperley, D. C. *Chem. Mater.* **2007**, *19* (10), 2686–2693.

(108) Ran, J.; Wu, L.; Ge, Q.; Chen, Y.; Xu, T. *J. Memb. Sci.* **2014**, *470*, 229–236.

(109) Wu, L.; Li, C.; Tao, Z.; Wang, H.; Ran, J.; Bakangura, E.; Zhang, Z.; Xu, T. *Int. J. Hydrogen Energy* **2014**, *39* (17), 9387–9396.

(110) Peckham, T. J.; Holdcroft, S. *Adv. Mater.* **2010**, *22* (42), 4667–4690.

(111) Lee, S. Y.; Shin, D. W.; Wang, C.; Lee, K. H.; Guiver, M. D.; Lee, Y. M. *Electrochem. commun.* **2013**, *31*, 120–124.

(112) Park, M. J.; Downing, K. H.; Jackson, A.; Gomez, E. D.; Minor, A. M.; Cookson, D.; Weber, A. Z.; Balsara, N. P. *Nano Lett.* **2007**, *7* (11), 3547–3552.

(113) Lee, M.; Park, J. K.; Lee, H.-S.; Lane, O.; Moore, R. B.; McGrath, J. E.; Baird, D. G. *Polymer (Guildf).* **2009**, *50* (25), 6129–6138.

(114) Zhang, J.; Li, J.; Tang, H.; Pan, M.; Jiang, S. P. *J. Mater. Chem. A* **2014**, *2* (48), 20578–20587.

(115) Li, N.; Guiver, M. D. *Macromolecules* **2014**, *47* (7), 2175–2198.

(116) Pan, J.; Zhu, L.; Han, J.; Hickner, M. A. *Chem. Mater.* **2015**, *27* (19), 6689–6698.

(117) Han, J.; Zhu, L.; Pan, J.; Zimudzi, T. J.; Wang, Y.; Peng, Y.; Hickner, M. A.; Zhuang, L. *Macromolecules* **2017**, *50* (8), 3323–3332.

(118) Kunimatsu, K.; Yagi, K.; Bae, B.; Miyatake, K.; Uchida, H.; Watanabe, M. *J. Phys. Chem. C* **2013**, *117* (8), 3762–3771.

(119) Hickner, M. A.; Fujimoto, C. H.; Cornelius, C. J. *Polymer (Guildf).* **2006**, *47* (11), 4238–4244.

(120) Jung, H.; Ohashi, H.; Tamaki, T.; Yamaguchi, T. *Chem. Lett.* **2013**, *42* (1), 14–16.

(121) Kim, Y. S.; Dong, L.; Hickner, M. A.; Glass, T. E.; Webb, V.; McGrath, J. E. *Macromolecules* **2003**, *36* (17), 6281–6285.

(122) Aamer, K. A.; Tew, G. N. *Macromolecules* **2007**, *40* (8), 2737–2744.

(123) Gohy, J.-F.; Lohmeijer, B. G. G.; Varshney, S. K.; Schubert, U. S.
       Macromolecules **2002**, *35* (19), 7427–7435.

(124) Anders, E.; Grevesse, N. *Geochim. Cosmochim.\ Acta* **1989**, *53*, 197–214.

(125) Yaroshevsky, A. A. *Geochemistry Int.* **2006**, *44* (1), 48–55.

(126) Ho Kim, S.; Worsley, M. A.; Valdez, C. A.; Shin, S. J.; Dawedeit, C.; Braun, T.;
       Baumann, T. F.; Letts, S. A.; Kucheyev, S. O.; Jen J. Wu, K.; Biener, J.; Satcher, J.
       H.; Hamza, A. V. *RSC Adv.* **2012**, *2* (23), 8672.

(127) Walker, C. N.; Versek, C.; Touminen, M.; Tew, G. N. *ACS Macro Lett.* **2012**, *1*
       (6), 737–741.

(128) Walker, C. N.; Bryson, K. C.; Hayward, R. C.; Tew, G. N. *ACS Nano* **2014**, *8* (12),
       12376–12385.

(129) Cramer, N. B.; Bowman, C. N. 2013.

(130) Cramer, N. B.; Bowman, C. N. *J. Polym. Sci. Part A Polym. Chem.* **2001**, *39* (19),
       3311–3319.

(131) Cramer, N. B.; Reddy, S. K.; O'Brien, A. K.; Bowman, C. N. *Macromolecules*
       2003, *36* (21), 7964–7969.

(132) Hoyle, C. E.; Lee, T. Y.; Roper, T. *J. Polym. Sci. Part A Polym. Chem.* **2004**, *42*
       (21), 5301–5338.

(133) Deubel, F.; Bretzler, V.; Holzner, R.; Helbich, T.; Nuyken, O.; Rieger, B.; Jordan,
       R. *Macromol. Rapid Commun.* **2013**, *34* (12), 1020–1025.

(134) Sarapas, J. M.; Tew, G. N. *Angew. Chemie Int. Ed.* **2016**, *55* (51), 15860–15863.

(135) Sarapas, J. M.; Tew, G. N. *Macromolecules* **2016**, *49* (4), 1154–1162.

(136) Northrop, B. H.; Coffey, R. N. *J. Am. Chem. Soc.* **2012**, *134* (33), 13804–13817.

(137) Hogg, R.; Wilkins, R. G. *J. Chem. Soc.* **1962**, *0*, 341–350.

(138) Potts, K. T.; Usifer, D. A.; Guadalupe, A.; Abruna, H. D. *J. Am. Chem. Soc.* **1987**, *109* (13), 3961–3967.

(139) Potts, K. T.; Usifer, D. A. *Macromolecules* **1988**, *21* (7), 1985–1991.

(140) Varcoe, J. R.; Slade, R. C. T. *Fuel Cells* **2005**, *5* (2), 187–200.

(141) Ciszewski, J. T.; Mikhaylov, D. Y.; Holin, K. V.; Kadirov, M. K.; Budnikova, Y. H.; Sinyashin, O.; Vicic, D. A. *Inorg. Chem.* **2011**, *50* (17), 8630–8635.

(142) Hutchison, K.; Morris, J. C.; Nile, T. A.; Walsh, J. L.; Thompson, D. W.; Petersen, J. D.; Schoonover, J. R. *Inorg. Chem.* **1999**, *38* (10), 2516–2523.

(143) Maestri, M.; Armaroli, N.; Balzani, V.; Constable, E. C.; Thompson, A. M. W. C. *Inorg. Chem.* **1995**, *34* (10), 2759–2767.

(144) Collin, J. P.; Guillerez, S.; Sauvage, J. P.; Barigelletti, F.; De Cola, L.; Flamigni, L.; Balzani, V. *Inorg. Chem.* **1991**, *30* (22), 4230–4238.

(145) Guadalupe, A. R.; Usifer, D. A.; Potts, K. T.; Hurrell, H. C.; Mogstad, A. E.; Abruna, H. D. *J. Am. Chem. Soc.* **1988**, *110* (11), 3462–3466.

(146) Kelly, J. M.; Long, C.; O'Connell, C. M.; Vos, J. G.; Tinnemans, A. H. A. *Inorg. Chem.* **1983**, *22* (20), 2818–2824.

(147) Hess, M.; Roeben, E.; Habicht, A.; Seiffert, S.; Schmidt, A. M. *Soft Matter* **2019**, *15* (5), 842–850.

(148) Rossow, T.; Seiffert, S. *Polym. Chem.* **2014**, *5* (8), 3018.

(149) Edson, J. B.; Macomber, C. S.; Pivovar, B. S.; Boncella, J. M. *J. Memb. Sci.* **2012**, *399–400*, 49–59.

(150) Ge, Q.; Ran, J.; Miao, J.; Yang, Z.; Xu, T. *ACS Appl. Mater. Interfaces* **2015**, *7* (51), 28545–28553.

(151) Sharma, M.; Yashonath, S. *J. Chem. Phys.* **2008**, *129* (14), 144103.

(152) Shen, L.; Chen, Z. *Chem. Eng. Sci.* **2007**, *62* (14), 3748–3755.

(153) Chen, D.; Hickner, M. A. *Macromolecules* **2013**, *46* (23), 9270–9278.

(154) Zhu, L.; Zimudzi, T. J.; Li, N.; Pan, J.; Lin, B.; Hickner, M. A. *Polym. Chem.* **2016**, *7* (14), 2464–2475.

(155) Morgan, G.; Burstall, F. H. *J. Chem. Soc.* **1937**, 1649–1655.

(156) Mugemana, C.; Guillet, P.; Hoeppener, S.; Schubert, U. S.; Fustin, C.-A.; Gohy, J.-F. *Chem. Commun.* **2010**, *46* (8), 1296.

(157) Mansfeld, U.; Winter, A.; Hager, M. D.; Festag, G.; Hoeppener, S.; Schubert, U. S. *Polym. Chem.* **2013**, *4* (11), 3177.

(158) Kornyshev, A. A.; Kuznetsov, A. M.; Spohr, E.; Ulstrup, J. *J. Phys. Chem. B* **2003**, *107* (15), 3351–3366.

(159) Van Der Sluys, W. G. *J. Chem. Educ.* **2001**, *78* (1), 111–115.

(160) Le Roy, D. J.; Gordon, A. R. *J. Chem. Phys.* **1938**, *6* (7), 398–402.

(161) Zhu, L.; Yu, X.; Hickner, M. A. *J. Power Sources* **2018**, *375*, 433–441.

(162) Francisco, V.; Basilio, N.; García-Río, L. *J. Phys. Chem. B* **2012**, *116* (17), 5308–5315.

(163) Maity, P.; Saha, B.; Kumar, G. S.; Karmakar, S. *RSC Adv.* **2016**, *6* (87), 83916–83925.

(164) Lounis, F. M.; Chamieh, J.; Leclercq, L.; Gonzalez, P.; Geneste, A.; Prelot, B.; Cottet, H. *J. Phys. Chem. B* **2017**, *121* (12), 2684–2694.

(165) Olesen, N. E.; Westh, P.; Holm, R. *J. Colloid Interface Sci.* **2015**, *453*, 79–89.

(166) Tonga, G. Y.; Mizuhara, T.; Saha, K.; Jiang, Z.; Hou, S.; Das, R.; Rotello, V. M. *Tetrahedron Lett.* **2015**, *56* (23), 3653–3657.

(167) Fu, J.; Schlenoff, J. B. *J. Am. Chem. Soc.* **2016**, *138* (3), 980–990.

(168) Grew, K. N.; Chiu, W. K. S. *J. Electrochem. Soc.* **2010**, *157* (3), B327–B337.

(169) Wang, H.; Wang, J.; Zhang, S.; Xuan, X. *J. Phys. Chem. B* **2008**, *112* (51), 16682–16689.

(170) Hribar, B.; Southall, N. T.; Vlachy, V.; Dill, K. A. *J. Am. Chem. Soc.* **2002**, *124* (41), 12302–12311.

(171) Pigga, J. M.; Teprovich, J. A.; Flowers, R. A.; Antonio, M. R.; Liu, T. *Langmuir* **2010**, *26* (12), 9449–9456.

(172) Marcus, Y. *J. Solution Chem.* **2008**, *37* (8), 1071–1098.

(173) Bernal, J. D.; Fowler, R. H. *J. Chem. Phys.* **1933**, *1* (8), 515–548.

(174) Samoilov, O. Y. *Discuss. Faraday Soc.* **1957**, *24* (0), 141–146.

(175) Bhowmik, D.; Malikova, N.; Mériguet, G.; Bernard, O.; Teixeira, J.; Turq, P. *Phys. Chem. Chem. Phys.* **2014**, *16* (26), 13447–13457.

(176) Dougherty, D. A. *Science (80-.).* **1996**, *271* (5246), 163–168.

(177) Ma, J. C.; Dougherty, D. A. *Chem. Rev.* **1997**, *97* (5), 1303–1324.

(178) Dougherty, D. A. *Acc. Chem. Res.* **2013**, *46* (4), 885–893.

(179) Bingham, R. C. *J. Am. Chem. Soc.* **1976**, *98* (2), 535–540.

(180) Gallivan, J. P.; Dougherty, D. A. *J. Am. Chem. Soc.* **2000**, *122* (5), 870–874.

(181) Lewis, G. N.; Randall, M. *J. Am. Chem. Soc.* **1921**, *43* (5), 1112–1154.

(182) da Silva, D. J. R.; Longo, R. L. *J. Mol. Liq.* **2019**, *282*, 577–586.

(183) Yahyaee, A.; Nazifi, M.; Kianpour, M.; Heidar, K. T. *Am. J. Anal. Chem.* **2018**, *09* (04), 257–271.

(184) Fabry, T. L.; Fuoss, R. M. *J. Phys. Chem.* **1964**, *68* (4), 971–974.

(185) Kunze, R. W.; Fuoss, R. M. *J. Phys. Chem.* **1963**, *67* (4), 911–913.

(186) Gujt, J.; Bešter-Rogač, M.; Hribar-Lee, B. *J. Mol. Liq.* **2014**, *190* (11), 34–41.

(187) Lind, J. E.; Fuoss, R. M. *J. Phys. Chem.* **1961**, *65* (6), 999–1004.

(188) Kunze, R. W.; Fuoss, R. M. *J. Phys. Chem.* **1963**, *67* (4), 914–916.

(189) Sauerheber, R.; Heinz, B. *Chem. Sci. J.* **2016**, *6* (4), 4–8.

(190) Amicangelo, J. C.; Armentrout, P. B. *J. Phys. Chem. A* **2000**, *104* (48), 11420–11432.

(191) Hu, M.; Tang, J.; Li, S.; Xia, S.; Jiang, Y. *J. Chem. Eng. Data* **2008**, *53* (2), 508–512.

(192) Lopes, A.; Farelo, F.; Ferra, M. I. A. *J. Solution Chem.* **1999**, *28* (2), 117–131.

(193) Ghalami-Choobar, B.; Shafaghat-Lonbar, M.; Mossayyebzadeh-Shalkoohi, P. *J. Mol. Liq.* **2015**, *212*, 922–929.

(194) Akiyama, R.; Yokota, N.; Otsuji, K.; Miyatake, K. *Macromolecules* **2018**, *51* (9), 3394–3404.

(195) Kamcev, J.; Paul, D. R.; Freeman, B. D. *Macromolecules* **2015**, *48* (21), 8011–8024.

(196) Sondheimer, S. J.; Bunce, N. J.; Lemke, M. E.; Fyfe, C. A. *Macromolecules* **1986**, *19* (2), 339–343.

(197) Rollet, A. L.; Diat, O.; Gebel, G. *J. Phys. Chem. B* **2002**, *106* (12), 3033–3036.